2019

The Pre-Roche Lobe Overflow Evolution of Massive Close Binary Stars: A Study of Rotation, Wind Enhanced Mass-Loss, and the Bi-Stability Jump

Thomas C. Gehrman Jr.
Minnesota State University, Mankato

The Pre-Roche Lobe Overflow Evolution of Massive Close Binary Stars: A Study of Rotation, Wind Enhanced Mass-Loss, and the Bi-Stability Jump

by

Thomas C. Gehrman Jr.

A Thesis Submitted in Partial Fulfillment of the

Requirements for the Degree of

Master of Science

in

Physics

Minnesota State University, Mankato

Mankato, Minnesota

November 2019

November 11, 2019

The Pre-Roche Lobe Overflow Evolution of Massive Close Binary Stars: A Study of Rotation, Wind Enhanced Mass-Loss, and the Bi-Stability Jump

Thomas C. Gehrman Jr.

This thesis has been examined and approved by the following members of the student's committee.

_____

Dr. Paul Eskridge, Advisor

_____

Dr. Rebecca Bates

_____

Dr. Analía Dall'Asén

_____

Dr. Jorge Méndez, Graduate Coordinator

The Pre-Roche Lobe Overflow Evolution of Massive Close Binary Stars: A Study of Rotation, Wind Enhanced Mass-Loss, and the Bi-Stability Jump

Thomas C. Gehrman Jr.
Master of Science in Physics
Minnesota State University, Mankato
2019

Abstract

Massive stars have the ability to enrich their environment with heavy elements and influence star formation in galaxies. Some massive stars exist in binary systems with short orbital periods. These are called massive close binaries. It is important to understand the evolution of massive close binary systems to gain insight about galaxy evolution. Massive stars above 20 solar masses experience a bi-stability jump where there is a sudden increase in mass-loss rate in their winds. There is ongoing research in this field, but the study of the bi-stability jump and its effects on massive close binary star properties has not been done before. A related question is whether binarity can produce a slow rotating, nitrogen-rich massive star such as those found in the Large Magellanic Cloud (Hunter et al. 2008). To accomplish this, two single-star models from Higgins & Vink (2019) and Brott et al. (2011) were used to model a close binary system with the 1-dimensional hydrodynamic stellar evolution code MESA. A grid of models using Higgins & Vink (2019) stellar parameters was created by varying 5 parameters: the convective step overshoot, the tidally enhanced wind coefficient, the wind enhancement factor, the initial rotation, and the initial masses of both stars. Two models were created to compare the approaches of Higgins & Vink

(2019) and Brott et al. (2011). Results show that early on in the evolution of the rotating models, the primary star has a more nitrogen-rich photosphere and rotates slower than the secondary star. Tidally enhanced winds are strong enough to strip off the surface layers of the primary. This exposed the nitrogen-rich envelope that is enhanced due to mixing. Tidal forces and tidally enhanced winds slow the rotation rate of the primary star. The existence of the bi-stability jump in massive close binary stars does have an effect on binary properties and could prevent a Roche lobe overflow event. From the numerical data from the models, predictions for characteristics of a wind-blown bubble provide possible future observational properties that are testable with current X-ray observatories.

Table of Contents

Chapter 1

Introduction

Understanding the evolution of massive stars is a key to understand how they ionize their environment (the interstellar medium or ISM here after), how star formation occurs in the Milky Way Galaxy, and how the ISM is enriched with heavy elements. Advances in computational astrophysics have provided progress towards connections between the theory and observations of massive stars. Advanced stellar modeling codes, such as MESA (Modular Experiments for Stellar Astrophysics), are able to implement the complex physics of massive stellar winds, rotationally induced instabilities, and internal mixing caused by the thermodynamic properties of a massive star. This provides the ability to address current questions as: Why are some slow rotating massive stars more nitrogen-rich than fast rotating stars? Should rotation enhanced wind mass loss be included in modeling? What is the jump temperature and magnitude of the bi-stability jump, which magnifies mass loss by stellar winds? Answering these questions could constrain coefficients and parameters used to model massive stars to match observations. These include the initial surface rotation and mass of the star, the wind factor that alters the amount of mass lost through winds, the convective overshoot coefficient that effects mixing, and what mixing agents should be included inside the star to drive the diffusion of angular momentum and elements. To understand more about the evolution of massive stars these parameters and conditions need to be constrained by modeling and observations.

The majority of massive stars are in binary star systems and some are in close binary orbits with periods (P_{orb}) less than 10 days, with $\bar{P}_{orb} \approx 5$ days (Duchêne & Kraus 2013). Close binary systems add additional complexities to stellar modeling. For instance, they will induce a differential gravitational force on each other that effects the rotation and internal mixing of the stars. Their gravitational force on each other will significantly enhance their winds (known as tidally enhanced winds). Mass lost due to winds from a star can be accreted onto its companion star. Addressing these issues increases in difficulty, since the majority of massive stars exist in binaries.

Young massive stars are classified as O and B[1] stars, have masses above $\sim 8\mathrm{M}_{\odot}$[2], and surface temperatures above ~ 25 kK (kK stands for 10^3 Kelvin). They possess winds that have mass loss rates between $10^{-4} - 10^{-6}$ $\mathrm{M}_{\odot}$ yr^{-1} and have a large range of rotation rates. They are the most luminous stars in the sky with $\log L/\mathrm{L}_{\odot} \sim 4 - 6$ and therefore are the easiest to observe [3]. However, they are few in number, because they have short lifetimes in comparison to lower mass stars like the Sun and because the initial mass function[4] disfavors them. Massive stars have the ability to create shock fronts or "wind-blown bubbles" by their winds. The mass loss from their winds rams into the atoms in the ISM and effectively ionizing them. These wind-blown bubbles can be observed with both optical and X-ray observatories.

[1]Spectral classification is used to classify the surface temperature and luminosity of a star. The classification scheme from hottest O stars to coolest M stars goes as: OBAFGKM.

[2]Here $\mathrm{M}_{\odot} = 1.9892 \times 10^{33}$ g is the mass of the Sun (Bahcall et al. 2005)

[3]$\mathrm{L}_{\odot} = 3.8418 \times 10^{33}$ ergs s^{-1} is the luminosity of the Sun (Bahcall et al. 2005)

[4]The initial mass function (IMF) provides a description of the relative number of star formed as a function of stellar mass. From observations, the IMF indicates that there are more lower mass stars than massive ones

There are two foci of this study. One is to understand how the bi-stability jump, which causes a significant increase in mass loss from massive stellar winds, effects binary physical properties. The bi-stability jump happens for massive stars above $20M_{\odot}$. At temperatures between 27 kK and 25 kK a runaway recombination of FeIV to FeIII will happen throughout the winds. This sudden of FeIV to FeIII dramatically increases the wind mass loss rate. Mass lost from a binary system will have an effect on the orbital angular momentum (J_{orb}) of the binary system. The change of J_{orb} over time will increase due to the sudden increase in the wind mass-loss rate from the bi-stability jump of both stars. This could mean the bi-stability could have an observable effect on a massive close binary system. Second, to possibly answer the question why do some slow rotating, nitrogen-rich massive stars exist in the Large Magellanic Cloud (Hunter et al. 2008). In this thesis a grid of models by varying several parameters (discussed below) were created to attempt to address these questions. In addition, the evolution of rotation, mass loss through winds, ^{14}N surface abundance, binary separation, orbital period, and orbital angular momentum. The mass-luminosity plane was used to provide insight on how the bi-stability jump and mass loss effects the models.

Single-star models were created based on the works of Higgins & Vink (2019) and Brott et al. (2011), who constrained their models to match observations. Models of massive close binary systems were created by using the stellar evolution code MESA (Paxton et al. 2010). Binary parameters and coefficients were chosen based off of the

works of Eggleton (1983), Paxton et al. (2015), Hurley et al. (2002), Bondi & Hoyle (1944), and Tout & Eggleton (1988). Numerical outputs from the binary models were used to calculate characteristics of a predicted wind-blown bubble by using the equations from Weaver et al. (1977) and Weaver et al. (1978). Using the predicted wind-blown bubble characteristics, the online program PIMMS (Portable, Interactive Multi-Mission Simulator), provided by NASA, was used to predict count rates for two X-ray observatories, the Chandra X-ray Observatory and X-ray Multi-Mirror Mission-Newton (XMM). The counts rates provided from PIMMS could provide a connection between models presented in this study and observations.

A grid of models was created by varying four parameters: the convective step overshoot α_{ov}, the wind factor f_v, the initial rotation rate v_{init}, and the tidal wind enhancement factor B_W. The grid of models used a primary star mass of $\mathrm{M}_\star = 35\mathrm{M}_\odot$ and secondary[5] star mass of $\mathrm{M}_\star = 25M_\odot$ with an orbital period of 4 days. This was done using the stellar parameters provided by Higgins (private communication). Two models were created for comparing the works of Higgins & Vink (2019) and Brott et al. (2011) in a binary system. Brott et al. (2011) models were reproduced using the stellar parameters provided by Keszthelyi (private communication). An additional grid of models was created by varying the initial primary and secondary masses using the stellar parameters for both Higgins & Vink (2019) and Brott et al. (2011).

[5]The primary is always referred to the initially more massive star in the binary system and the secondary the less massive.

The theoretical evolution and physical parameters of stellar models are discussed in Chapter 2. In Chapter 3 MESA, the program used in this work, is explained. Chapter 4 introduces the theoretical background of stellar rotation. A more in depth explanation of differential rotation is presented because of its ability to induce strong chemical and angular momentum mixing. Chapter 5 includes the theoretical evolution and physical parameters of binary models. Chapter 6 discusses the theory and observations of line driven winds of massive stars. In Chapter 7 binary modeled results are analyzed, discussed, and model comparisons are made between the two papers Higgins & Vink (2019) and Brott et al. (2011). Chapter 8 uses specific binary and single star model results, for example orbital velocity, to make detailed predictions for future observations. Finally, chapter 9 is the summary and conclusion of the work and discussion of potential future work.[6]

[6]Note it is not necessary to read all of Chapters 2-4 to understand the analysis and results of Chapters 7 and 8. The following covers the theory that is necessary to understand the results: Sections 2.5-2.6, 4.2.1-4.3, Chapter 5, and Chapter 6.

Chapter 2

Stellar Model

To accurately model any type of star, there are "main ingredients" that need to be defined. These are conservation of momentum and energy, energy transport by combination of convection, conduction, and/or radiation, and luminosity (energy per unit time) generation. There can be a large range of elemental abundance for different stars, therefore two stars with the same mass may not experience the same evolution. The equations of stellar structure are the foundation of a stellar model. In addition to the stellar structure equations, there are the equations used to model stellar atmospheres. Accurately modeling a stellar atmosphere is paramount, because it is the only part of the star an observer sees. There are four basic equations of stellar structure. They include: the equations of hydrostatic equilibrium, mass conservation, energy conservation, and radiative transfer. If we ignore convection, they are as follows:

$$\frac{dP(r)}{dr} = -\frac{\rho(r)GM(r)}{r^2} \tag{2.1}$$

$$\frac{dM(r)}{dr} = 4\pi r^2 \rho(r) \tag{2.2}$$

$$\frac{dT(r)}{dr} = \frac{3k_r \rho(r)}{64\pi r^2 \sigma_{ST} T^3(r)} L(r) \tag{2.3}$$

$$\frac{dL(r)}{dr} = 4\pi r^2 \rho(r) \epsilon(r) \tag{2.4}$$

where M, G, r, T, P, ρ, k_r, L, ϵ, σ_{ST} are the mass of the star, the gravitational constant, the distance from the center to any location in the star, local temperature, pressure, mass density, thermal conductivity, luminosity, nuclear energy generation rate and the Stefan-Boltzmann constant, respectively. In modeling it is more common and advantageous to have the above equations written as functions of mass m rather than r, e.g. when rotation is involved. Note that the four equations above are ideal, meaning the equations assume no changes over time and rotation. In addition, radiative transfer is not the only energy transport mechanism happening within a star. Therefore, the equations used in the models are extremely complex and are fully explained in Paxton et al. (2010) & Paxton et al. (2015). In addition to the stellar structure equations, there are four more components to model a star: an equation of state, a nuclear reaction network, elemental abundances and opacities (κ). The remainder of this chapter presents a detailed discussion of the initial physical characteristics of a single star, with the initial physical variables based on those adopted by Higgins & Vink (2019) and Brott et al. (2011).

2.1 Nuclear Reaction Network

Various types of nuclear reactions take place in the cores of stars, where all of the luminosity is created by the continuous fusing and decaying of elements and isotopes.

The CNO cycle, shown in Figure 2.1, and named for its catalysts ^{12}C, ^{16}O, and ^{14}N, contributes the majority of hydrogen burning for stars with $M_\star > 1.5 M_\odot$(see

Table 2.1: Luminosity output of the pp-chain and the CNO-cycle for various masses

Mass $M_\odot$	$\log L_{pp}$ $L_\odot$	$\log L_{CNO}$ $L_\odot$
20	1.81	4.86
25	1.94	4.88
30	2.14	5.07
35	2.01	5.23

Note Models were created using the inlists provided by Higgins (private communication)

Table 2.1). This criterion is well met for stars in this study, with all modeled stars having $M_\star \geq 20 M_\odot$.

The triple underlining of ^4He in Figure 2.1 is to indicate the production of ^4He in the CNO cycle. Parts of the CNO cycle have long timescales, specifically the weak nuclear decays for isotopes, ^{13}N, ^{15}O, and ^{18}F have half lives of 9.97 min, 122.24 sec, and 109 min (Chu et al. 1999). This can have significant impact on stellar composition evolution. If a star experiences mixing from its core to the envelope, then processed material, such as ^{14}N, will be drawn out of the core and into the envelope and surface of the star.

Figure 2.2 shows the result of rotational mixing of CNO burning products, particularly nitrogen, for high mass stars. In Figure 2.2, log(N/H) is the surface mass fraction of ^{14}N over hydrogen and is calculated as $\log \frac{N/14}{H/1}$. This gives a negative number since it is less then 1. Therefore, it is convention to add 12 to the equation to make the value positive. This mixing can lead to surface nitrogen enrichment which is currently being studied in both single and binary observations and modeling (see,

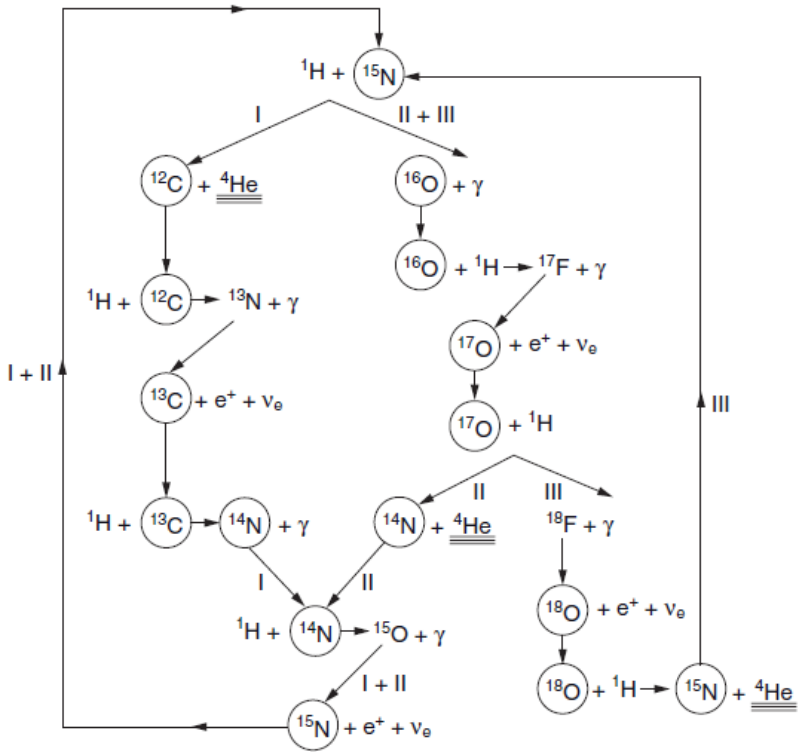

Figure 2.1: CNO cycle diagram showing the three possible reaction chains. The catalyst of the cycle are circled (Figure 6.6 from LeBlanc 2010)

for instance, Song et al. 2018).

A simple nuclear reaction network (NRN) model is adequate for this study such as provided by MESA's basic.net (Timmes 1999). Therefore the basic.net from MESA is used. This nuclear reaction network consists of isotopes of: ^{1}H, ^{3}He, ^{4}He, ^{12}C, ^{14}N, ^{16}O, ^{20}Ne, and ^{24}Mg. Inlists provided by Keszthelyi (private communications) do not define a specific a NRN, therefore MESA defaults to the basic.net. MESA uses NACRE (Nuclear Astrophysics Compilation of REaction Rates, Angulo et al. 1999) for the rates at which nuclear reactions take place for different isotopes.

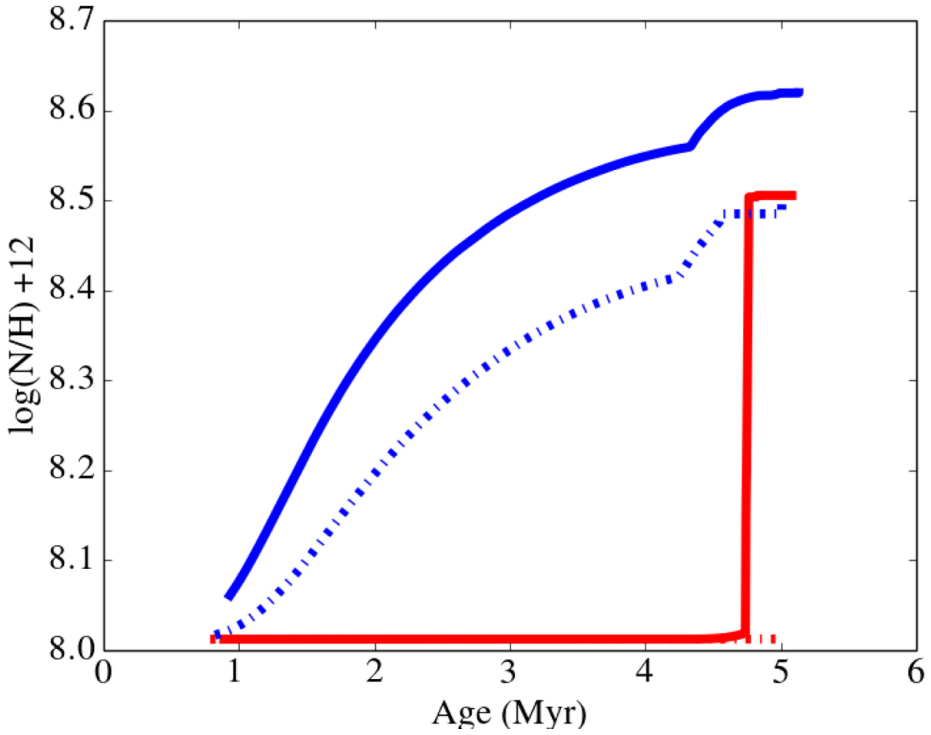

Figure 2.2: Figure 1 from Higgins & Vink (2019). The thick lines represent $\alpha_{ov} = 0.5$ and dotted $\alpha_{ov} = 0.1$. Blue lines are models with $v_{rot} = 200$ km s^{-1} and red for non-rotating models.

2.2 Equation of State

An example of a simple equation of state is the ideal gas law, $PV = nRT$, this law provides reasonable results for modeling the interior of stars, however there are additional physical processes that need to be considered. For example, different physics that contribute to the pressure, e.g. radiation pressure, degeneracy pressure, and Coulomb interactions. Radiation pressure is the result of photons interacting with free electrons or electrons in an atom. Degeneracy pressure is due to the Pauli exclusion principle which states that two fermions, such as electrons, can not share the same eigenstate and energy state. When electrons are forced to fill all lower energy

levels and the density of electrons keeps increasing a degeneracy pressure is created, contributing to the pressure in the equation of state. Coulomb interactions happen due to the electromagnetic force between ions and electrons. The equation of state is also dependent on the abundance of elements in the star.

See Section 4.2 of Paxton et al. (2010) for the full explanation of the equation of state used in the modeling program MESA (discussed in Chapter 3). MESA uses the Helmholtz free energy variables ρ and T rather then P and T. Higgins & Vink (2019) use the equation of state (EOS) from MESA. MESA uses the OPAL tables (Rogers 2002) and, for lower temperatures and densities the EOS tables of Saumon, Chabrier, & Van Horn (1995), also known as the SCVH tables. Paxton et al. (2010) used the combination of both the above tables to generate a broader range for their EOS tables (see Figure 1 in Paxton et al. 2010). The EOS tables include the range of values of $2.1 < \log T < 8.2$ and $-10 < \log Q < 5.69$, which cover the range of T and Q values in this work. Here $\log Q$ is determined in MESA by the following equation from Paxton et al. (2010):

$$\log Q = \log \rho - 2 \log T + 12 \tag{2.5}$$

Temperature T , density ρ and the internal energy Q are in units of K, g cm^{-3}, and ergs, respectively. The tables are generated for a range of $0.0 < X < 1.0$ and $0 < Z < 0.04$ values, here X, Y, and Z, stand for the fraction of ^1H, ^4He and metals (all elements and isotopes heavier than ^4He), respectively. Inlists provided

by Keszthelyi (private communications) do not provide an EOS therefore the MESA equation of state is used. For models presented in chapter 7, at the terminal age main sequence TAMS, the $\log \rho$ and $\log T$ are high enough that MESA will switch to HELM EOS (Timmes & Swesty 2000).

2.3 Opacities

Opacities have a large effect on a star's evolution in the core and especially in the envelope. The envelope is the space between the core and the surface of the star. Photons generated in the core do not leave in a straight path out into space after they are produced. They experience radiative diffusion, where a photon can be constantly absorbed and scattered by electrons and ions. It takes 1.7×10^5 years for a photon in the Sun to escape into space (Mitalas & Sills, 1992). The mean free path l is defined as the average distance traveled between emission and absorption of a photon and can be defined as (Carroll & Ostlie, 2007):

$$l = \frac{1}{\kappa_\lambda \rho} \tag{2.6}$$

Here κ_λ (units of $\mathrm{cm}^2\ \mathrm{g}^{-1}$) is the opacity for a photon of a particular wavelength and ρ is the local density of matter. The shorter l is the longer the diffusion timescale. The magnitude of the opacity depends on the interaction of photons with matter. Defining the different physical mechanisms that contribute to the opacity gives insight about the structure of a star.

A large opacity can have a significant impact on a star, for example increasing a star's radius. This increase in radius is caused by photons strongly interacting with matter, implying a longer diffusion time scale and "puffing" up the envelope. Opacity is dependent on the local temperature, density, and metallicity. A higher density creates more possibility for interactions with photons. There is a temperature dependence, because higher temperatures cause an increase in ionization states and therefore more absorption and scattering events. At higher metallicity the frequency of bound-bound transitions is amplified due to the increase of heavier elements that have more electrons. In addition, the free electron density is higher because metals have lower ionization potentials then helium and hydrogen.

MESA uses the combined radiative and electron conductive opacities of Cassisi (2007) for a range of -6 $\leq \log \rho \leq$ 9.75 and 3 $\leq \log T \leq$ 9 (See Paxton et al. 2010). Values above or below $\log T$ or $\log \rho$ of Cassisi (2007) are not reached in this work, therefore no other opacity tables are used.

2.4 Abundances

Abundances are the fraction of all elements that reside in the star. They play a key role in the evolution of massive stars. As discussed previously they affect the EOS, the stellar evolution equations, and opacities. In addition to affecting the underlying equations they play a key role in my research. Changing the abundance can alter the amount of mass lost due to stellar winds. Higgins & Vink (2019) and Brott et al.

(2011) use the derived wind mass loss equations of Vink et al. (2001), where the expressions are metal-dependent, implying an increase in metal abundance can have a significant impact on $\dot{M}_W$. $\dot{M}_W$ is the amount of mass loss per unit time by the wind expressed in units of $M_\odot$ yr^{-1}. A massive star's wind can be changed by a factor ~ 5 by altering the iron abundance in the photosphere (Vink et al. 2001). Altering the mixing coefficients, which affects angular momentum and elemental diffusion in the interior of a star, changes the evolutionary history of a stellar and binary model. Both mixing coefficients and metal dependent winds affect a star's surface abundance evolution, which is dependent on the initial abundances.

The abundances are set following the works of Higgins & Vink (2019) and Brott et al. (2011) for single stars. In Brott et al. (2011) initial abundances were set to X = 0.7274, Y = 0.2638 and Z = 0.0088, with specific heavy elements set to the Asplund et al. (2004) values (see Brott et al. 2011 for a detailed description of the abundances). However using these abundances does not reproduce the results of Brott et al. (2011) when using MESA. Therefore Keszthelyi et al. (2017) set Z =0.014 and for heavy elements used a combination of Asplund et al. (2004) and Lodders (2003) tables to reproduce Brott et al. (2011) results. However when the Iglesias & Rogers (1996) opacity tables are used then Grevesse & Sauval (1998) abundances were used for reproducing the Brott et al. (2011) models. To follow the work of Higgins & Vink (2019) the Grevesse & Sauval (1998) tables are used.

2.5 Mixing

Mixing plays a vital role in a star as it determines how matter and energy are transported. Of all the requirements to model a star, mixing length theory and the types of mixing, e.g. convection, convection overshoot, semiconvection, and rotational mixing have been the hardest to properly model and compare to observations. A goal of stellar modeling is to restrict the mixing coefficient values through observations and therefore no longer vary them in models.

The core may receive extra fuel (Hydrogen) by mixing, thereby extending a star's lifetime. Mixing plays a vital role in angular momentum transport in a stellar interior, and effects what type of matter reaches the photosphere and therefore what we observe. Mixing is not the same for all stars because it is dependent on the thermodynamic and rotational properties of the star. For instance, a low mass star ($M_\star < \mathrm{M}_\odot$) has a deep convection zone "digging" far down in its stellar interior. While massive stars can have two convection zones in the core and envelope (see figure 2.3).

The following subsections list and explain the types of mixing addressed in this study. The mixing equations define the location in the model interior, where the boundaries lie, and the conditions for the formation of the type of mixing. A physical parameter varied for each star in the binary models is the mixing coefficient α_{ov} (explained in Section 2.5.3).

The mixing length theory (MLT) adopted by Brott et al. (2011) is based on Böhm-Vitense (1958). Higgins & Vink (2019) use that of Henyey et al. (1965). Each MLT

has the same adjustable parameter, α_{conv}, and is defined as (Carroll & Ostlie 2007):

$$\alpha_{conv} = l_{ml}/H_P \tag{2.7}$$

Here l_{ml} is the mixing length in the star, e.g. how far a parcel of matter will travel before it dissipates into its surroundings. $H_P = P/\rho g$, the pressure scale height, is the distance over which P will change by a factor of e. For the Sun, $H_P \approx \mathrm{R}_\odot/10$ (Carroll & Ostlie 2007) where $\mathrm{R}_\odot = 6.9598 \times 10^{10}$ cm (Bahcall et al. 2005). Higgins & Vink (2019) and Brott et al. (2011) both set $\alpha_{conv} = 1.5$ in their models.

2.5.1 Convection

Both Higgins & Vink (2019) and Brott et al. (2011) use the Ledoux (1947) criterion to define the convective core boundaries:

$$\nabla_{rad} < \nabla_{ad} + \frac{\phi}{\delta}\nabla_\mu \tag{2.8}$$

$$\text{Where } \nabla_{rad} = \left(\frac{\partial \ln T}{\partial \ln P}\right)_{rad}, \quad \nabla_{ad} = \left(\frac{\partial \ln T}{\partial \ln P}\right)_{ad}, \quad \nabla_\mu = \left(\frac{\partial \ln \mu}{\partial \ln P}\right)_{rad} \tag{2.9}$$

ϕ and δ are from the equation of state and are defined as:

$$\delta = -\left(\frac{\partial \ln \rho}{\partial \ln T}\right)_P \qquad \text{and} \qquad \phi = \left(\frac{\partial \ln \rho}{\partial \ln \mu}\right)_{P,T} \tag{2.10}$$

Where μ is the mean molecular weight. In chemically homogeneous environments

where $\nabla_\mu = 0$ the Ledoux criterion is equal to the Schwarzschild (1906) criterion $\nabla_{rad} < \nabla_{ad}$. Convection takes place when the magnitude of energy-transport by radiation becomes less than for transport by an adiabatic process and/or μ gradients (causing a buoyant force on the parcel of matter). In an actual star convection and radiation energy-transport happen at the same time. In Figure 2.3 convection only happens in the core and near the surface for the stellar model both early on and at the TAMS. Convection, as shown in Figure 2.3, is the strongest mixing agent in the stellar model. Also the Figure provides a good example showing that radiation energy-transport is dominant in the envelopes of massive stars.

2.5.2 Semiconvection

Semiconvection is a special case of convection and exists in the regions where mixing is unstable for the Schwarzchild criterion, but stable for the Ledoux criterion (Equation 2.8). When the condition in Equation 2.8 is satisfied semiconvection takes place with a diffusion coefficient from Langer (1983):

$$D_{sc} = \alpha_{sc} \left(\frac{K}{6 C_P \rho} \right) \frac{\nabla_T - \nabla_{ad}}{\nabla_{ad} + \frac{\phi}{\delta} \nabla_\mu - \nabla_T} \tag{2.11}$$

where K is the radiative conductivity:

$$K = \frac{4acT^3}{3\kappa\rho} \tag{2.12}$$

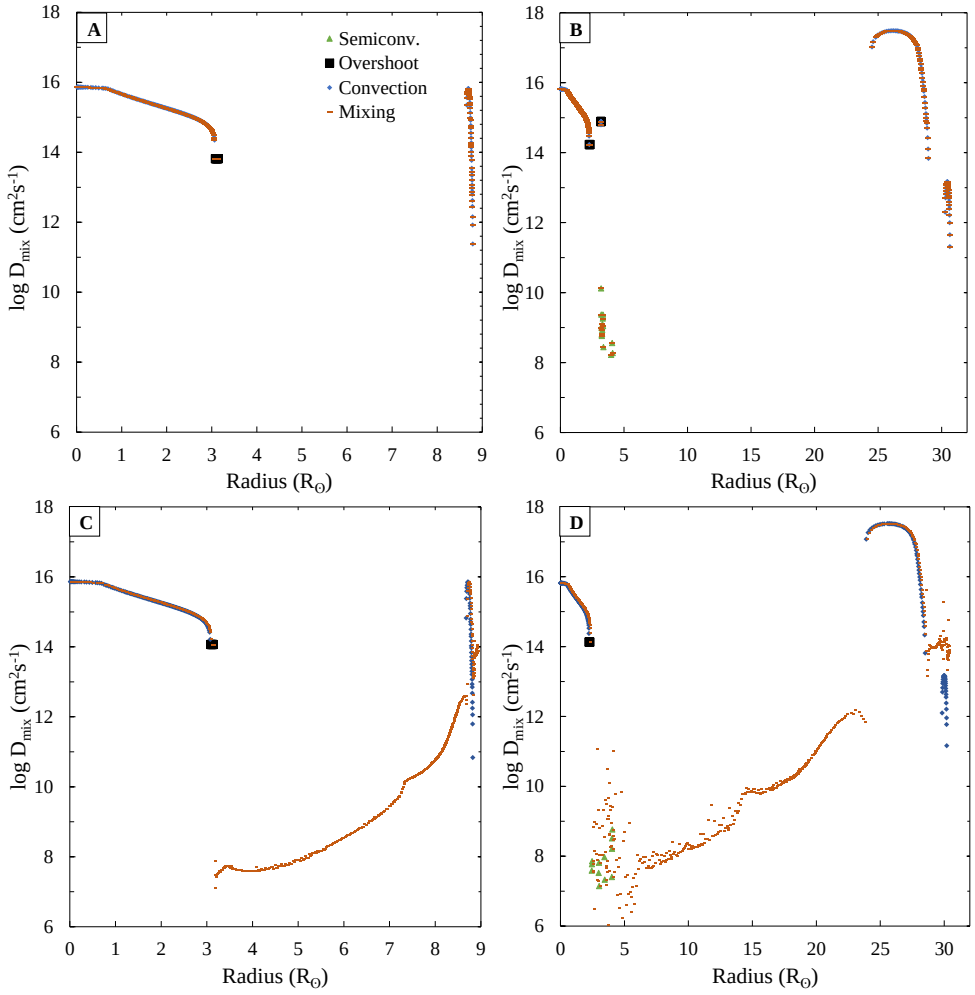

Figure 2.3: Plot of Mixing Coefficients vs radius for a 40$M_\odot$ star with v_{init} = 200 km s^{-1} using Higgins & Vink (2019) inlists. A & C are the star at ~10^5 years and B & D are at TAMS. A & B are with rotational mixing coefficients turned off and C & D turned on. The convective overshoot black box is enlarged to emphasize its location in the star.

and C_p is the specific heat at constant pressure. Finally α_{sc} is the semiconvection efficiency coefficient and is set to one for this work. See Table 2.3 for the parameter values of both Higgins & Vink (2019) and Brott et al. (2011).

By comparing panels a) and c) to b) and d) in Figure 2.3 it appears that semi-

convection happens later in a star's life, with rotational mixing either on or off. Semiconvection in the models shown is not the strongest contributor to mixing when compared to convection or convective overshoot near the boundary of the core.

The radius of the core can be determined in the panels by the location of the discontinuity of convection and convective overshoot in panels c), b) , and d), or the drop after convective overshoot in panel a). For graphs a) and c) the core boundary is $\approx 3R_{\odot}$ and for b) and d) $\approx 4.5R_{\odot}$. The radii change between panels a) and b) because both the radii of the core and the star evolve throughout a star's life.

2.5.3 Convective Overshoot

One of the main foci of this research is convective overshoot, particularly of the core. Convective overshoot has a significant impact on a star's evolution as shown in Figures 2.4 and 2.5. Convective overshoot takes place at the boundaries of the convection zones, where instead of the parcel of matter stopping it is allowed to diffuse past the boundary. Overshoot can be modeled as a step or an exponential decay as a function of H_P. This can be done in two different ways or a combination of both. One way is using exponential diffusion overshoot (Herwig 2000):

$$D_{ov} = D_0 \exp\left(\frac{-2z}{H_v}\right) \tag{2.13}$$

H_v is the velocity scale height and is defined as $H_v = f_{ov} H_P$ and f_{ov} is the exponential overshoot coefficient. See Appendix A and B for the values, locations, and evolution-

ary stages affected by this coefficient for the Higgins & Vink (2019) and Brott et al. (2011) models. D_0 is another adjustable parameter and is set to 1 in Higgins & Vink (2019). MESA has f_{ov} coefficient setting, but it requires an initial $(f_{ov})_0$. This is explained in Paxton et al. (2010), Paxton et al. (2013), and Paxton et al. (2015). The change from convective mixing to convective overshoot happens at a distance of $f_0 H_P$ near the convective boundary where $\nabla_{ad} \equiv \nabla_{rad}$. The problem is at the edge of the convection zone the mixing coefficients goes to zero. Introducing a new overshoot coefficient, $(f_{ov})_0$, allows setting the convective overshoot boundary into the convection zone, therefore making the mixing coefficients nonzero. Setting the value of $(f_{ov})_0$ creates an offset, implying f_{ov} has to be adjusted to the correct physical value. For example, if $(f_{ov})_0 = 0.05$ and if it is physically required that $f_{ov} = 0.5$ for a model, f_{ov} has to be set to 0.45 due to the offset. In Higgins & Vink (2019) $(f_{ov})_0$ is set to 0.005. In Brott et al. (2011) it is set to 0.001 (Keszthelyi private communication).

Another prescription for convective overshoot is step overshoot. Here overshoot is a defined as step function to go past the convective boundary:

$$l_{ov} = \alpha_{ov} H_P \tag{2.14}$$

Varying the α_{ov} coefficient between 0.1-0.5 has a large effect in modeling a star. Both Higgins & Vink (2019) and Brott et al. (2011) use a combination of step and exponential diffusion overshoot. Brott et al. (2011) used a step overshoot $\alpha_{ov} = 0.335$.

The overshoot coefficient can be set to individually mix during the MS (hydrogen

burning), helium burning, and after helium burning (metals). In addition, it can mix burning shells during later evolutionary stages. In all stars, past hydrogen burning, there exists burning shells outside the core. For example, during helium burning, the core will be surrounded by a hydrogen burning shell. To give a few examples, if convective overshoot happens only for hydrogen burning shells, then the overshoot coefficient is set for mixing of hydrogen during the onset of a hydrogen burning shell. If metals and helium have convective overshoot in the core and hydrogen does not, then the coefficient is specifically set to mix in the core during helium and heavier elemental burning stages.

Both Higgins & Vink (2019) and Brott et al. (2011) have convective overshoot set for hydrogen in the core, above, and below a hydrogen burning shell (see Appendix A & B). Therefore the star experiences most of the mixing due to step overshooting during the MS where hydrogen is the dominate element in the core. Referring to Figure 2.3 again, in panels b) & d) there is a small amount of convective overshoot taking place near the boundary of the core. This validates the claim that overshoot only takes place in the core during hydrogen burning.

The focus of Higgins & Vink (2019) was modeling the observations of the detached binary star system HD 166734 by adjusting different values of α_{ov}, f_v and v_{rot} (v_{rot} and f_v will be discussed later). HD 166734 consists of a primary and secondary star with dynamical masses of $39.5 M_{\odot}$ and $33.5 M_{\odot}$. Higgins & Vink (2019) use a combination of massive stellar winds, rotational mixing, and extreme values of α_{ov}

$= 0.1$ to $\alpha_{ov} = 0.5$ to reproduce the ^{14}N surface abundances, masses, luminosities, and temperatures of both the primary and secondary stars in HD 166734. They conclude that the values of $\alpha_{ov} = 0.3 \pm 0.1$ and $\alpha_{ov} = 0.5 \pm 0.1$ reproduced the physical characteristics of the primary and secondary, respectively. They increased their sample size for model comparison based on the work of Markova et al. (2018), which includes a list of roughly 30 O type stars.

Table 2.2: Stellar Evolution Model Settings for this Thesis

Models	EOS	NRN	Opacity	MLT	Core Boundary
MESA module	eos	net	kap	mlt	mlt
Brott	MESA	basic.net	OPAL	Böhm-Vitense	Leduox
Higgns	MESA	basic.net	gs98	Henyey	Leduox

Brott and Higgins labels represent the parameters of the work of Higgins & Vink (2019) and Brott et al. (2011).

Table 2.3: Numerical Stellar Parameters

Models	X	Y	Z	α_{ov}	f_{ov}	α_{sc}	α_{conv}
Brott	0.7274	0.2638	0.0088	0.335	-	1	1.5
Keszthelyi	0.7274	0.2638	(0.02-0.014)	0.335	0.001	1	1.5
Higgins	0.7000	0.2800	0.0200	$(0.1 - 0.5)$	0.005	1	1.5

Brott and Higgins definitions are described in Table 2.2. Keszthelyi (label representing Keszthelyi et al. 2017) relaxes the X, and Y from the initial MESA values to the values used by Brott et al. (2011). Z is relaxed from 0.02 to 0.014 as shown in Appendix B.

2.6 Mass-Luminosity Plane

I conclude this chapter by discussing a useful tool that will be used throughout this work. Figure 2.4 shows a vector relationship of α_{ov}, $\dot{M}_W$ and v_{init} plotted on an inverted mass axis vs. luminosity (normally given in $\log L$) (analog of the Hertzsprung-Russell Diagram). v_{init} is the initial rotation velocity of the star given in units of km s^{-1}. The plot is a theoretical graph of the Mass-Luminosity plane from Higgins & Vink (2019). The theoretical vector, representing a stellar evolutionary track, can be altered by modifying α_{ov}, $\dot{M}_W$, and v_{init} as shown in Figure 2.5. In the binary models presented in Chapter 7, $\dot{M}_W$ has the greatest influence in changing the theoretical vector.

A mass-luminosity relationship exists for both binaries and single stars. This is an extremely useful observational tool (For binaries See Figure 7.7 from Carroll & Ostlie 2007). One form of the relationship for single stars can be written in the following way (Higgins & Vink 2019):

$$L = \mu^4 M^\beta \tag{2.15}$$

Here β is a parameter that varies as a function of mass. Stellar evolution can be altered by changing μ by altering the abundances. A star with a higher μ will exhibit a larger luminosity according to Equation 2.15.

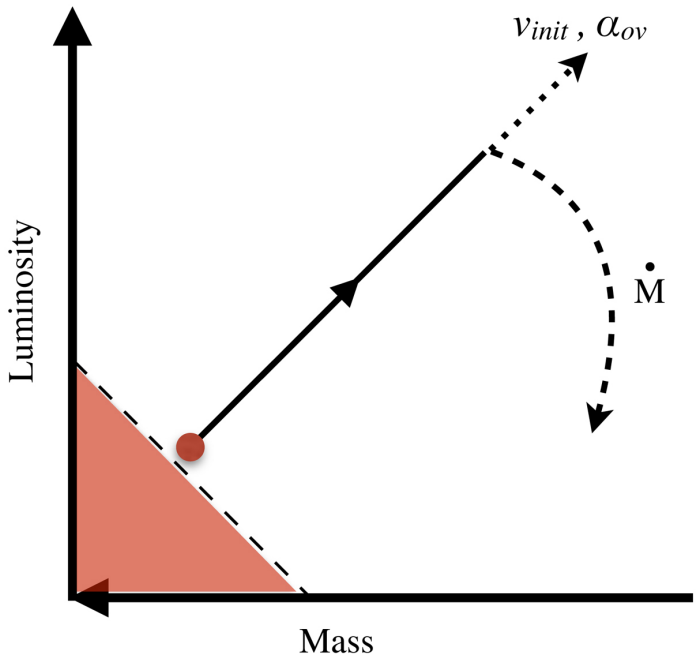

Figure 2.4: The theoretical Mass-Luminosity plane where a star's evolution is described as a vector quantity that depends on v_{init}, α_{ov}, and $\dot{M}$. The highlighted area is the "forbidden zone" meaning that a stellar model can not evolve into this region

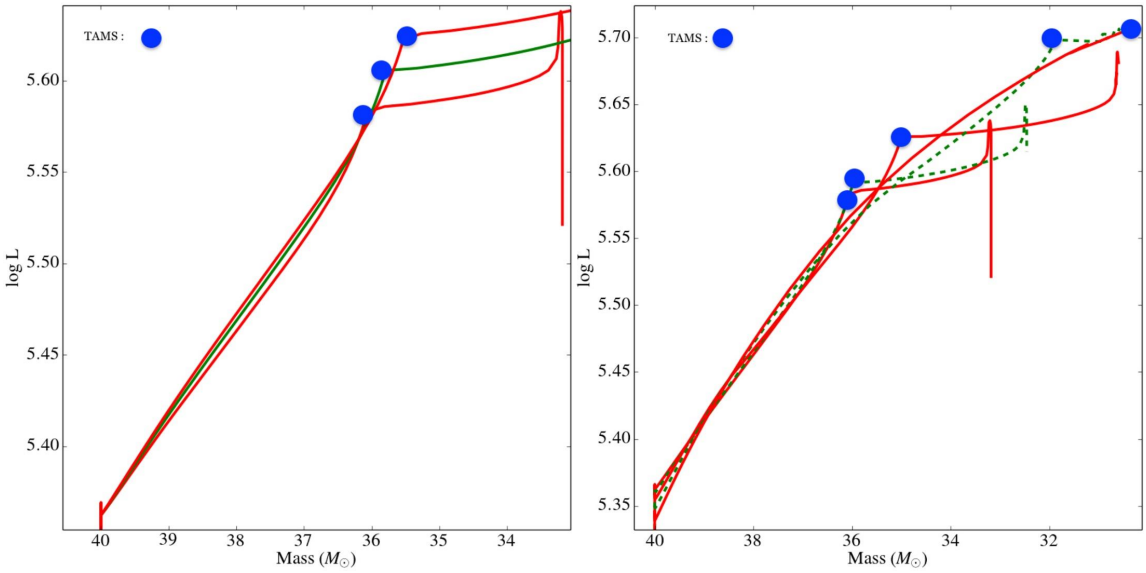

Figure 2.5: A plot of a $40M_\odot$ model on the Mass-Luminosity plane from Higgins & Vink (2019). The left graph is for $\alpha_{ov} = 0.1$, 0.3, and 0.5 corresponding to red, green, and red, respectively. The blue dots give the location TAMS. The right graph from Higgins & Vink (2019) for velocities from $100 - 500$ km s^{-1}. The point at TAMS is extended by an increasing v_{init}.

Chapter 3

Stellar Evolution Code - MESA

MESA is one-dimensional stellar evolution code written in FORTRAN 90/95. It has the ability to start a ZAMS model with masses in the range of $0.08\mathrm{M}_{\odot} < M_{\star} < 100\mathrm{M}_{\odot}$ and can be applied to model binary systems, white dwarfs, and massive stars until core collapse. It is easy for a user to call different independent types of FORTRAN modules in one model e.g. the EOS, opacities, nuclear reaction networks, and convection allow changes in structure as well as more efficient use of computation resources. The open source MESA community is constantly testing, adding, and updating algorithms. There have been five papers published, each adding new modules and updated physics created by users and creators of MESA. For example, Paxton et al. (2010) included the ability to model mass loss and single star evolution, while Paxton et al. (2015) added a new binary module and improved all previous physics.

The default FORTRAN modules are called by the MESAstar library to generate a basic star, but the user can alter the defaults and call extra MESA FORTRAN modules in the inlists. Binary and star inlists are where the user can define different FORTRAN modules used to model their systems. For example, in the inlist of Higgins & Vink (2019) the syntax of `MLT_option = 'Henyey'` calls the MLT FORTRAN module in MESA for the algorithm written for the mixing length theory of Henyey et al. (1965). The FORTRAN module mlt called in the inlist consists of multiple model routines for different mixing length theories, e.g. `'Cox'` (Cox & Giuli

1968 chapter 14), `'ML1'` (Böhm-Vitense 1958), `'ML2'`, `'Mihalas'` (Mihalas & Kunasz 1978), and `'Henyey'` (Henyey et al. 1965), and none, with a mixing length parameter α_{conv} that the user can call and adjust within their inlists.

The modularity of MESA implies calling individual FORTRAN modules e.g., eos and mlt module, to MESAstar separately to generate a model. This allows for parallel processing, thus shorter run-times, and allows to easily change schemes within a module. For example, a user can easily change the MESAstar module from calling the Vink wind algorithm (Vink et al. 2001), via `hot_wind_scheme = 'Vink'`, in their inlists to have MESAstar call the `hot_wind_scheme = 'Kudritzki'` (Kudritzki et al. 1989). Another example, if a user changes the inlists for the mlt module initiating the 'Henyey' MLT defined above and instead they have mlt module initiate the 'Cox' MLT (syntax `MLT_option = 'Cox'` algorithm).

MESA has many FORTRAN modules and routine options used in other code, e.g. the STERN code (Heger et al. 2000; Yoon & Langer 2005; Petrovic et al. 2005), GENEVA (Eggenberger et al. 2008), and KEPLER (Weaver et al. 1978). In addition, the creators tests the modules, e.g. mlt, net, and kap modules in other codes for validity. Therefore using these tested modules is extremely helpful for creating inlists for model to model comparisons. See Paxton et al. (2010), Paxton et al. (2013), Paxton et al. (2015), Paxton et al. (2018) for examples of stellar model output comparisons. In this thesis, two papers are compared: Higgins & Vink (2019) uses MESA and Brott et al. (2011) uses the STERN code. Figure 3.1 shows a comparison of the evolution

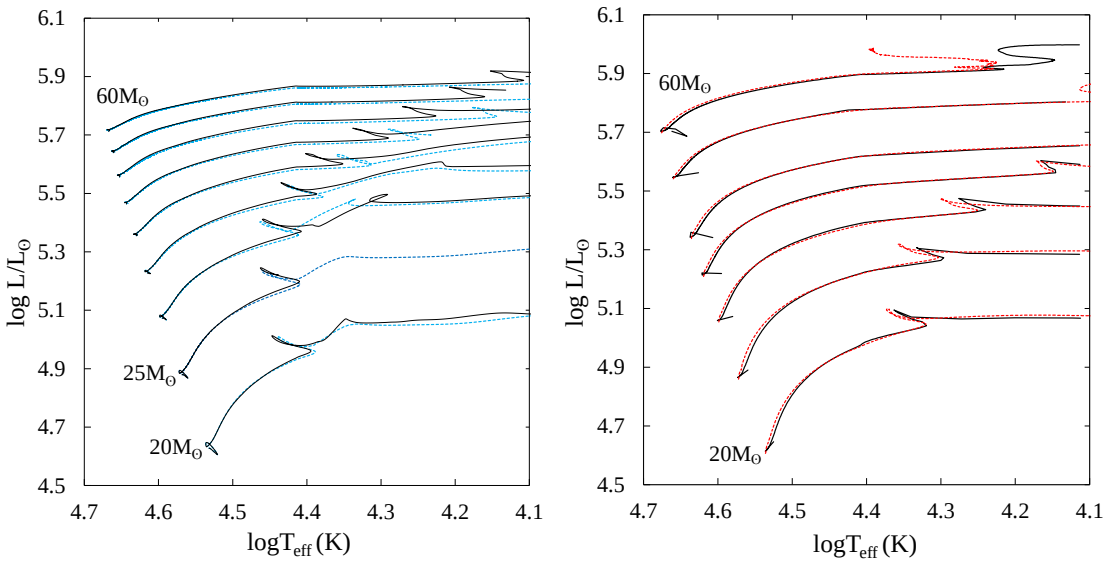

Figure 3.1: Evolutionary tracks for mass from 20-60$M_{\odot}$ at increments of 5$M_{\odot}$. Comparison between MESA inlists provided by Keszthelyi (private communication) (right) and Higgins (private communication) left panel. Blue lines are the evolutionary tracks from Higgins & Vink (2019) (left) and red lines are Brott et al. (2011)(right) models and black are the ones using provided inlists using MESA version 11554.

tracks between an older version of MESA and a newer one (Higgins & Vink 2019) and the inlists provided by Keszthelyi (private communication) to model Brott et al. (2011). The stellar parameters used to compare Higgins & Vink (2019) and the newer MESA version was for an initial rotation rate of 200 km s^{-1} and $\alpha_{ov} = 0.1$. There is good agreement for both papers using MESAstar for the mass range 20-45$M_{\odot}$. Later in the stellar evolution there is a pronounced difference for high mass models. Note that the 25$M_{\odot}$ terminated slightly after helium core burning for Higgins model unlike the rest of the models in Figure 3.1. It is still reasonable to use the 25$M_{\odot}$ model for the binary star model because all binary star models terminate roughly before helium core burning.

Another benefit of using MESA is the ease of expanding upon the original code using MESA's `run_star_extras.f90` and implementing a user defined algorithm to run within the inlists for the user's stellar model. MESA has extra FORTRAN routines so models can be easily extended to add new stellar modeling theory. For example, `use_other_wind.f90` is written to extend or change the wind scheme used by MESAstar. MESA is thread safe which allows modules to do parallel computations and reduce computation time for eos and net models for example. (See Table 9 in Paxton et al. 2010 for computation times for different amounts of threads.) MESAstar has real-time plots (PGSTAR), which allows the user to see the evolution of their system through various programmed plots, e.g. HR-diagram and mass loss plots. The user can also create their own real-time generated plots in their inlists. Finally, a very useful tool is the ability to either save a model for the future use or save a photo. Photos are "snap shots" of the model and are generated periodically through out the model evolution. A user can stop a run, adjust or change an argument in their inlists, and restart from the photo. The argument for using MESA for this thesis is its ease of comparison with other codes, ease of modifying, useful tools, and modularity.

The inlists used in this work were provided by Higgins (private communication) for modeling Higgins & Vink (2019) (in Appendix A), Keszthelyi (private communication) for modeling Brott et al. (2011) (in Appendix B), and the binary inlists I created to model massive close binary stars (in Appendix C). Appendices A-C provide the syntax for all options defined in the inlist shown in Tables 2.2 and 2.3. The

MESA version used in this thesis is 11554.

3.1 MESA Design

MESAstar, a FORTRAN library where models are generated, creates hundreds to thousands of models over an evolution run in real time through arrays and pointers in FORTRAN. The evolution of a star happens over a timestep δt ranging from seconds to $\sim 10^5$ yrs between each model for a star. MESA has two base pointers written for all FORTRAN modules. They are the "s" pointer which points to the information in the MESAstar FORTRAN library and the "b" pointer that is meant for the binary FORTRAN library. For example, in Appendix D.2, the binary pointer has an index that is called for either the calculated information of the primary star $i = 1$ or the secondary star $i = 2$.

A position in a star can be represented by a mass coordinate or at a specific radius in terms of cells defined as k in MESA, where $k = 1$ is the surface of the modeled star and k increases towards the center. Over the evolution of the model, the cells will split or merge depending upon the physics and tolerances set by MESA or the user. The user can vary the spatial resolution of the program by varying parameters such as the `varcontrol_target` option. This allows the program to have a larger mesh (number of cells) for problems, e.g. extremely small δt during core collapse, however this introduces more computational error. Another example is `use_gold_tolerances` option which creates a stronger restriction on energy conservation error during a run.

When a convergent solution is not met for a model in a run then MESAstar goes through a retry and a backup which executes with a smaller δt to get a solution.

Each individual cell represents all the physics and physical quantities of the star. As an example, cell $k = 1$ represents the surface physics and quantities of: the radius, rotation, luminosity, mass, hydrogen abundance, moment of inertia, density, and so forth. The syntax for a few of the examples above are m(k), i(k), r(k), L(k), and rho(k) (See Figure 9 of Paxton et al. (2010)). When the tolerance is reached for the physical quantities of a cell, the cell will split. Therefore the number of cells in a modeled star evolves over time. This is called remeshing. More complex physics for each cell is calculated upon basic physical variables, e.g., rotational instabilities (Chapter 4) and convection is calculated from the mass, pressure, and temperature of the cells.

3.2 MESAstar RUN

MESA does mesh refinement, analytic Jacobians, and coupled solution of the structure and composition equations. MESAstar first reads the inlists and run_star_extras.f90 and initializes the physics modules to create a nuclear reaction network and access the EOS and opacity data. The specified starting model is then loaded into memory, and the evolution loop is entered. The procedure for one timestep has four basic elements. First, the code prepares to take a new timestep by remeshing the model if necessary. Second, the code adjusts the model to reflect mass loss by winds or mass

gain from accretion, adjusts abundances for element diffusion, determines the convective diffusion coefficients, and solves for the new structure and composition using the Newton-Raphson solver. Third, the next timestep is estimated. Fourth, output files are generated.

3.3 MESA Binary Run

MESA binary performs each evolution step by independently solving the structure of each component and the orbital parameters, using the same timestep δt for each. This approach differs from MESAstar, which simultaneously solves for the structure of both stars and the orbit in a single Newton-Raphson solver. The choice to solve for each star separately gives a significant amount of flexibility and simplicity. Additional timestep limits are imposed in MESA binary that consider relative changes between the radius and Roche lobe radius of both components, the total orbital angular momentum.

Chapter 4

Rotation

A star's initial rotation stems from the conservation of angular momentum of the infalling matter during the pre-main sequence (PMS) stage. After PMS the evolution of surface rotation can change in many different ways depending on the evolutionary state of the star and the physical mechanisms taking place. For example, if no angular momentum is lost from the star, then during the main sequence it will generally rotate slower over a long period of time as the radius of the star becomes slightly larger. At the next stage a massive star will evolve and become a red supergiant, where the radius is larger. Therefore the rotation speed will slow down to conserve angular momentum.

Rotation has a large impact on the evolution of massive stars, due to the inclusion of a centrifugal term in the stellar structure and rotational mixing equations (Heger et al. 2000; Meynet & Maeder 2000). There are two types of modeled rotation within a star: differential and solid body. When differential rotation takes place in a star various types of fluid instabilities occur, which effect angular momentum and elemental transport within a star during its evolution.

The initial rotation rate of both stars are variables in this work. The user can define the strength of chemical and angular momentum diffusion due to rotation by setting their coefficient values in the inlists. These values have a large impact on the evolution of a star and can lengthen its lifetime and increase surface abundances

dramatically. Rotation modeled in 3-dimensions provides better precision, however the models for a 1-dimension (1D) approximation gives good results when comparing to observations.

As explained in Chapter 2, the stellar evolution equations have to be re-derived to include the centrifugal term and the departure from spherical symmetry caused by rotation (see Paxton et al. 2013 for the new derived formula in MESA). Angular momentum and elemental diffusion coefficients, for different types of circulation and instabilities caused by rotation, need to be set to accurately model the interior of a star. See Table 4.1 for the velocity and diffusion coefficient variables and the types of circulation used in this work.

Below I give a brief introduction to the origin and evolution of a star's rotation followed by the observational evidence of rotation of the Sun. Two sections explain the theory and background of solid body and differential rotation and how it is treated in MESA. The majority of this section focuses on the theory behind the different types of circulations and instabilities that develop because of differential rotation.

Stars have a maximum rotational velocity limit, defined as the critical velocity (v_{crit}). When $\vec{g}_{grav} + \vec{g}_{cent} + \vec{g}_{rad} = 0$ the star has reached its critical rotation rate, where $\vec{g}_{grav}$, $\vec{g}_{cent}$, $\vec{g}_{rad}$ are the gravitational, centripetal and radiative acceleration, respectively. At this point the star starts losing matter. Critical velocity will be discussed in the last section of this chapter. In a binary system rotation can be affected by strong tidal interaction between the primary and the secondary (Hurley

et al. 2002). This will be discuss further in Chapter 7.

MESA models start out with solid body rotation and then the rotation profile changes according to the different circulations and mixing agents e.g., convection, implemented (See Figure 4.4). The instabilities are strong enough to change the rotation profile from differential rotation to solid body or even a combination of both types. A good example is the Sun's rotation profile. It has both solid body rotation in its interior and differential rotation at and below its surface. The location of change from differential to solid body rotation in the interior of the Sun is called the tachocline. Its existence can be inferred from heliosiemology observations by the suppression of certain oscillatory modes in the Sun (Spiegel & Zahn 1992). Many ongoing investigation are being made as to why the tachocline exists. One possibility is a type of dynamo is created, for instance the Spruit-Taylor dynamo (discussed later). This can connect the core and envelope's rotation through magnetic fields and thus enforcing solid body rotation.

4.1 Solid Body Rotation

The equation of motion for a parcel of mass in a rotating fluid is based upon the Navier-Stokes equation. The theory of uniform rotation is derived from the Roche model and is shown in Maeder & Meynet (2012). The Roche approximation assumes the gravitation potential and rotation to be of a centrally condensed core with a mass-less photosphere (Lebovitz 1967). The effective gravity, $\vec{g}_{eff}$, is dependent on both

the gravitational force and centrifugal force at a specific radius in a star. Equation 2.1 now includes the centrifugal term in the rotating star and the equation becomes (Maeder & Meynet 2012):

$$\frac{1}{\rho}\vec{\nabla}P = -\vec{\nabla}\Phi + \frac{1}{2}\Omega^2\vec{\nabla}\left(r\sin\phi\right)^2 \tag{4.1}$$

$\Phi = -\frac{GM_r}{r}$ is gravitational potential. ϕ and r are the polar angle and radius, respectively. Following the derivation in Maeder & Meynet (2012), if the angular speed (Ω) is a constant then the centrifugal acceleration can be derived from a potential V_c.

$$-\vec{\nabla}V_c = \Omega^2 r\sin\phi \tag{4.2}$$

Therefore the sum of the potentials can be expressed in the following way (Maeder & Stahler 2009):

$$\Psi = V_c + \Phi \tag{4.3}$$

Thus all thermodynamic variables, e.g. ρ, P, T , are constant on all equipotential surfaces at a given radius. This implies the star is barotropic (Maeder & Meynet 2000) so the pressure is constant on the equipotential surfaces. Equation 4.1 can now be written as:

$$\frac{1}{\rho}\vec{\nabla}P = \vec{\nabla}\Psi \tag{4.4}$$

Ω is defined in MESA as $\Omega(k) = \frac{j(k)}{i(k)}$, where $j(k)$ and $i(k)$ are the angular mo-

mentum and momentum of inertia at cell k; this is altered at each timestep through the mass and radius cell adjustment. See Appendix B.6 of Paxton et al. (2013) for the full computational explanation of the change of Ω. Throughout the chapter the theory is based on Ω in units of s^{-1}, however, as shown in Table 4.1 and Appendices A and B, this thesis uses v_{rot} in units of km s^{-1} as the variable.

4.2 Differential Rotation

The shellular rotation law, which is the most widely used differential rotation law, was extensively studied by Zahn (1992). He assumed strong horizontal ($\hat{\theta}$) and a weak vertical ($\hat{r}$) turbulence in a star which enforces a constant Ω on isobaric surfaces. Therefore Equation 4.1 can not be applied when shellular rotation takes place. In spherical coordinates $\Omega(r, \phi)$ now becomes (Zahn 1992):

$$\Omega(r, \theta) = \bar{\Omega}(r) + \hat{\Omega}(r, \theta) \tag{4.5}$$

Here $\bar{\Omega}$ is the mean rotation velocity over a spherical surface and $\hat{\Omega}(r, \theta)$ represents Ω at a specific latitudinal zone. For example, zonal air flow in the Earth's atmosphere flows parallel between two different latitudes. However in the case of $\hat{\Omega}(r, \theta)$ rotation may not be parallel to two different latitudes in the star (See section 2 from Zahn 1992 for the full explanation). The assumption for weak vertical turbulence is justified because of density stratification in a star, thus circulation in this direction is diminished.

According to Maeder & Meynet (2012) the star becomes baroclinic and the gravitational potential and Ω are constant on isobaric surfaces. However they are not constant on equipotential surfaces. Therefore the star can no longer be assumed to be spherically symmetric. This implies that instead of constant g_{eff}, T, P, and ρ on an isobaric surfaces, one has to take an average of these quantities over an isobaric surface to get the complete stellar structure equations (Equations 2.1-2.4). For example, the new hydrostatic equilibrium equation becomes (Maeder & Stahler 2009):

$$\frac{dP(r)}{dM_P} = -\frac{GM_P}{4\pi r_P^4} f_P \tag{4.6}$$

$$f_p = \frac{4\pi r_P^4}{GM_P S_P} \frac{1}{< g_{eff}^{-1} >} \tag{4.7}$$

M_P, r_P, and S_P are mass, radius, and spherical surface area on an isobar. M_P is used in the derivative since the radius is no longer constant on an isobaric surface. When f_P equals 1, equation 4.6 becomes equation 2.1.

MESA adopts the shellular approximation of Meynet & Maeder (1997). Paxton et al. (2010) uses the 1-dimensional approximation as an argument to treat the isobars as equipotentials. They give a brief explanation and derivation of the new stellar structure equations based on the new inertial term discussed above and the averages taken over the isobars. However, they still treat the isobars as equipotentials even though they deviate from spherical symmetry and the star is baroclinic (Maeder & Meynet 2012).

The strength of differential rotation can be expressed by the magnitude of the gradient of Ω ($|\vec{\nabla}\Omega|$), which is known as the shear. When modeling a stellar interior in one dimension, this is simply $\frac{d\Omega}{dr}$. If the magnitude of the shear is 0 throughout the star, than the star has uniform rotation.

4.2.1 Chemical and Angular Momentum Diffusion

As noted above, certain conditions caused by rotation and a star's physical characteristics can lead to instabilities that can trigger different types of circulations. These circulations have a large impact on the angular momentum and chemical transport within the star. MESA treats the transport of chemical and angular momentum as fully diffusive. See Zahn (1992) for the full advection-diffusion equation.

Below, I describe each circulation used in the binary model, what instability condition needs to be satisfied for them to occur, and use profiles to show their location and mixing strength. I will also discuss the coefficients defined in this work for chemical and angular momentum diffusion. Listed below are the circulations and instabilities used in Higgins & Vink (2019) and Brott et al. (2011). The instabilities depend on both vertical and horizontal turbulence, thus implying that in the cases discussed below density stratification is weak enough to have rotation in the vertical direction.

Eddington-Sweet (ES) Circulation- First derived by Von Zeipel (1924) for rigid rotation and updated by Baker (1959) for more general rotation. The more modern version of the theory can be found in Maeder (1998) and explained in Heger

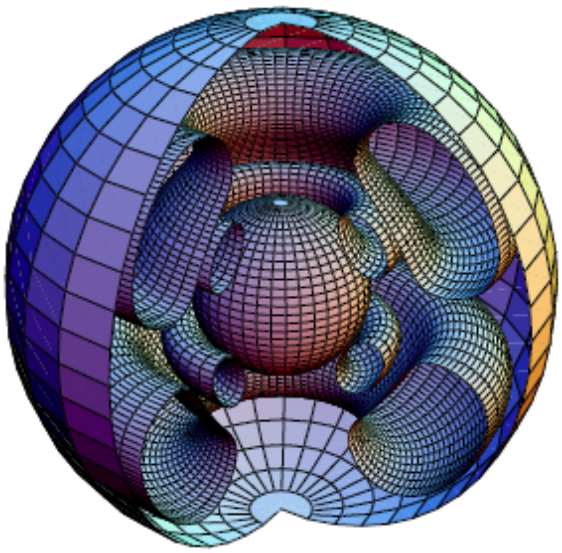

Figure 4.1: A rotating $20M_{\odot}$ model with solar metallicity and v_{init} = 300 km s^{-1}. The outer sphere is the star surface. The inner sphere is the outer boundary of the convective core. Figure is from Meynet & Maeder (2002).

et al. (2000). It is also known as meridional circulation, and is created by the breakdown of thermal stability due to differential rotation in a star. Isobaric and isothermal surfaces do not coincide, which leads to motion in the radial direction. In the differential rotation section I explained that radial turbulence (perpendicular to the isobars) is neglected since it is suppressed by high density gradients. In cases where these gradients hit a specific criterion (see Heger et al. 2000) they will drive the circulation generally in the radial direction. I say "generally" because the equations of motion are extremely complex (see Maeder 1998 and Heger et al. 2000 for the details). Figure 4.1 from Meynet & Maeder (2002) shows the ES circulation inside a star. The central sphere in the figure would be the core of the star. Note the circulation, represented by the elliptical toroids in Figure 4.1, is on the surface of the toroid rotating in the

radial direction, not along the axis of the toroids. If large mean molecular weight gradients, ∇_μ, do not exist to suppress the circulation, then it will have a largest impact on the transport of angular momentum and elements within the star (see Figure 4.5). In addition, the ES circulation has the largest impact on Ω diffusion, S (spin angular momentum), and elemental diffusion in comparison to the other circulations mentioned below.

Dynamical Shear Insability (DSI) - This instability exists when the energy that can be gained from the shear flows due to differential rotation is comparable to the required work for a mass cell to move against the gravitational potential (adiabatic turn over) and occurs on isobars at the dynamical timescale (Zahn 1992).

For example, assuming constant mean molecular weight μ, a cell of matter of higher ρ, T, and P is perturbed into a surrounding place of lower T, ρ, and P than its previous surroundings (in radial direction). During this processes the cell is unable to stay buoyant in the new medium and therefore is dynamically unstable and begins to fall. The cell begins to fall due to gravity and its difference in density with the surroundings. The time required for this convective processes to take place is the dynamical timescale, t_{dyn}. This is the amount of time for a star to respond to deviations from hydrostatic equilibrium. For example the model used to produce panels c) and d) in Figure 4.5 $t_{dyn} \approx 4 \times 10^4$ seconds. This time scale is infinitesimal in comparison to the lifetime of any star. The criterion for the Dynamical shear instability is written as (Maeder & Meynet 2012):

$$R_i \equiv \frac{g}{\rho} \frac{\frac{d\rho}{dz}}{(\frac{dv}{dz})^2} < Ri_{crit} \tag{4.8}$$

Another way to express this is as follows:

$$\rho(\delta v)^2 > g\ \delta\rho\ \delta z \tag{4.9}$$

Where δv, $\delta\rho$ and δz are small changes in velocity, density, and height. The left hand side of Equation 4.9 is the differential shear energy and the right side is the differential gravitational potential for a moving mass element. Ri_{crit} is the Critical Richardson number and is equal to 1/4. When this number is reached the instability develops and the circulation begins. This instability enforces differential rotation, and since no work is required to mix elements on an isobar, this instability is effective at mixing angular momentum and elements. However, as shown in Figure 4.5, the strict conditions for the instability prevents it to exist in any location in the star at $t \sim 10^5$ yrs or the TAMS.

Secular Shear Instability (SSI)- The condition for this instability is just the relaxed condition for the the dynamical shear instability. Thermal adjustments are allowed to take place in radial perturbations (Heger et al. 2000).

In this condition, the perturbed higher ρ cell, discussed above, is dynamically stable and can stay "afloat" in the medium. However over time the cell's temperature decreases as its thermal energy is transferred into the medium. Therefore its buoyancy diminishes which causes it to fall. The secular shear instability happens on the

thermal timescale also known as the Kelvin-Helmholtz time scale t_{kh}. This is the time for photons to diffuse from the core out to space (see section 2.2). Using the data from the model to produce panels c) and d) the t_{kh} is $\approx 2 \times 10^4$ years. Having a less strict criterion then the DSI, the SSI does exist in the model as shown in Figure 4.5.

Goldreich-Schubert-Fricke - The Goldreigh-Schubert-Fricke (GSF) instability (Goldreich & Schubert 1967 and Fricke 1968) arises if the temperature gradient ∇_T can't compensate for the centrifugal force caused by rotation. This instability takes place in the inviscid limit. This circulation enforces uniform rotation in chemically homogeneous stars.

All previous instabilities are suppressed by high density gradients or rather high mean molecular weight gradients ∇_μ. The cell example for both the dynamical shear and secular shear can be applied to GSF instability and ES-circulation in the radial direction. The high ρ cell is prevented from falling into a more dense environment, thus enforcing stability.

Spruit-Taylor dynamo (ST) - The Spruit-Taylor dynamo (Spruit 1999, Spruit 2002, Taylor 1973) is an instability where a toroidal field B_ϕ grows and changes to B_r. The characteristic growth rate of the instability is:

$$\sigma_g = \frac{\omega_A^2}{\Omega} \tag{4.10}$$

Here ω_A is the Alfén frequency (Alfvén 1942) defined as:

$$\omega_A = \frac{B}{(4\pi\rho)^{1/2}\, r} \tag{4.11}$$

B is the magnetic field of the star and Equation 4.11 is cgs explicit. The toroidal fields form concentric rings perpendicular to the rotation axis. The magnetic pressure provided by the rings coupled with the fact that the fields are unstable forces motions of elements and angular momentum side to side (see Figure 1 from Spruit 2002). If a magnetic field is present then there is a severe reduction in differential rotation because the ST-dynamo is strongly dependent on differential rotation $\frac{|\nabla\Omega|}{\Omega}$. Therefore it enforces an almost constant Ω. This dynamo theory gives a possible explanation for the appearance of Sun Spots and for the solid body rotation profile in the Solar interior.

The evolution of surface ^{14}N is dependent upon these instabilities and the other mixing processes (discussed in section 2.4) for massive stars. There is a slight difference shown between panels B) and D) in Figure 4.3 for ^{14}N. However, even when all instabilities are present, there is little difference between ^{1}H and ^{4}He mass fraction when comparing panels B) and D) in Figure 4.2.

4.3 Diffusion Equations

Below is the discussion of the diffusion equations from Heger et al. (2000) and how angular momentum and chemical diffusion take place as shown in Paxton et al. (2010). The equations include the diffusion coefficients for the above circulations and insta-

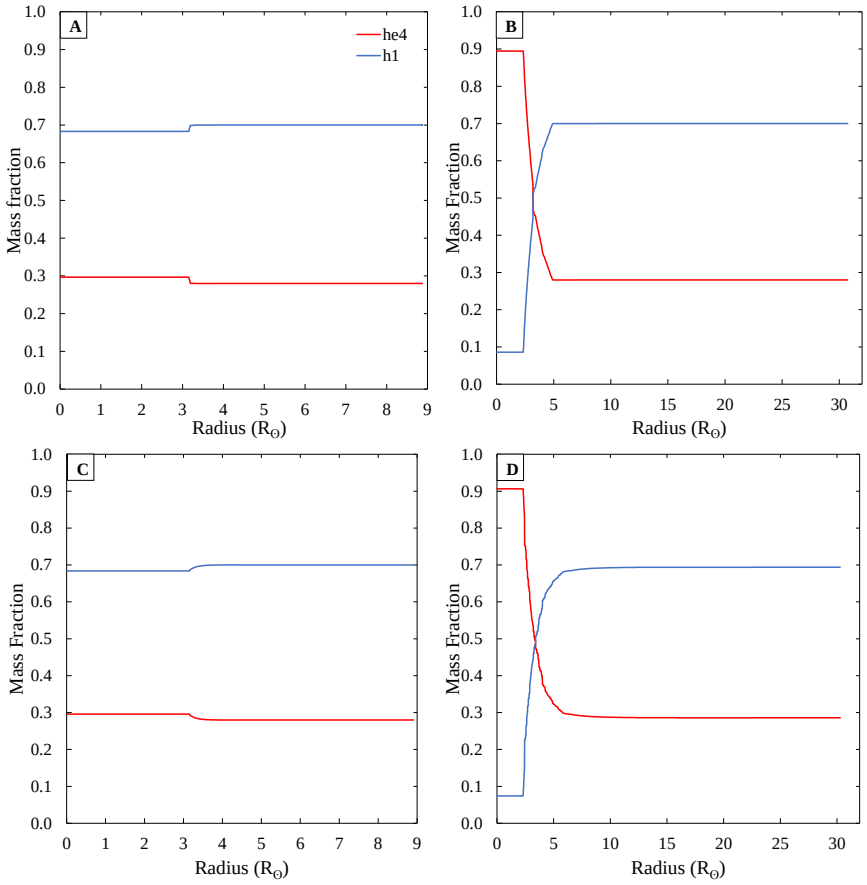

Figure 4.2: ^1H and ^4He mass fraction vs radius for 40M$_\odot$ star with v_{in} = 200 km s^{-1}. Panels A and B are all mixing coefficients turned off and C and D all are turned on. The age of the star in with A and C is $\approx 10^5$ years, where as B and D are at the TAMS.

bilities discussed in Section 6.4.2, above. The purpose of expressing the equations is to show how convection, semiconvection, and convective overshoot coefficients come into play when there is differential rotation in a star. The diffusion equation is given by Heger et al. (2000) as follows:

$$\left(\frac{\partial \chi_n}{\partial t}\right)_m = \left(\frac{\partial}{\partial m}\right)_t \left[(4\pi r^2 \rho)^2 D \left(\frac{\partial \chi_n}{\partial m}\right)_t\right] + \left(\frac{d\chi_n}{dt}\right)_{nuc} \tag{4.12}$$

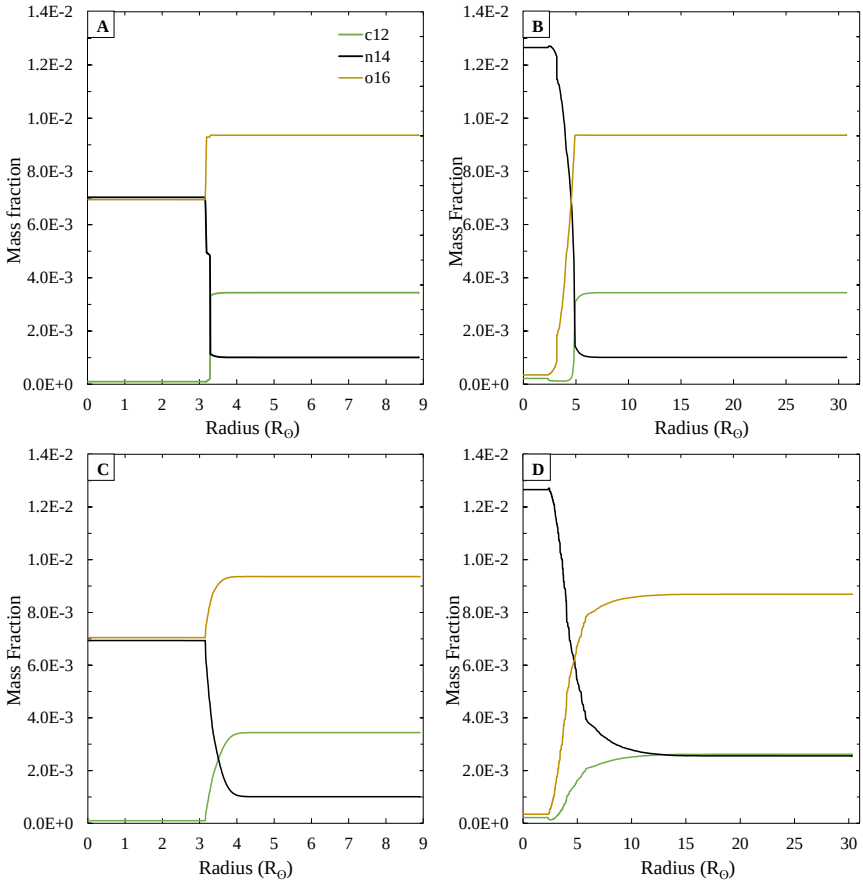

Figure 4.3: The same model as figure 4.2, but a plot of ^{12}C, ^{14}N, and ^{16}O mass fraction vs radius. These are catalysts for the CNO cycle and mixing can pull these elements to the envelope and surface of the star.

χ_n is the mass fraction of species n. D is the diffusion coefficient defined by:

$$D = D_{conv} + D_{sem} + D_{over} + f_c(D_{DSI} + D_{SHI} + D_{SSI} + D_{ES} + D_{GSF}) \qquad (4.13)$$

f_c is the angular momentum diffusion factor and is an adjustable parameter. In Higgins & Vink (2019) $f_c = 1/30$ and Brott et al. (2011) $f_c = 0.0228$. The equation used in MESA (see Appendix of Paxton et al. 2013) for the diffusion of angular

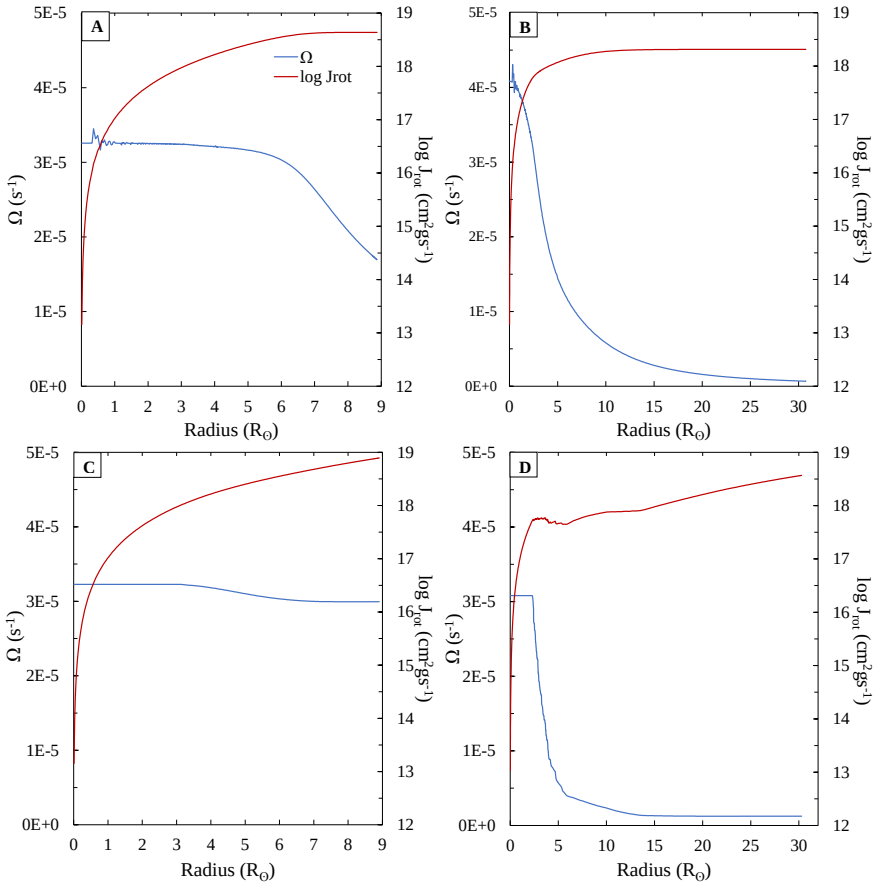

Figure 4.4: $\log J_{rot}$ & Ω vs radius for a $40 M_{\odot}$ star with $v_{in} = 200$ km s^{-1}. A & C are the star at $\sim 10^5$ years and B & D are at TAMS. A & B are with rotational mixing coefficients turned off and C & D turned on.

momentum is:

$$\left(\frac{\partial \omega}{\partial t}\right)_m = \frac{1}{I}\left(\frac{\partial}{\partial m}\right)_t \left[(4\pi r^2 \rho)^2 I \nu \left(\frac{\partial \omega}{\partial m}\right)_t\right] - \frac{2\omega}{r}\left(\frac{\partial r}{\partial t}\right)_m \left(\frac{1}{2}\frac{d \ln I}{d \ln r}\right) \tag{4.14}$$

Where I represents the moment of inertia at a mass coordinate. ν is the turbulent viscosity defined as:

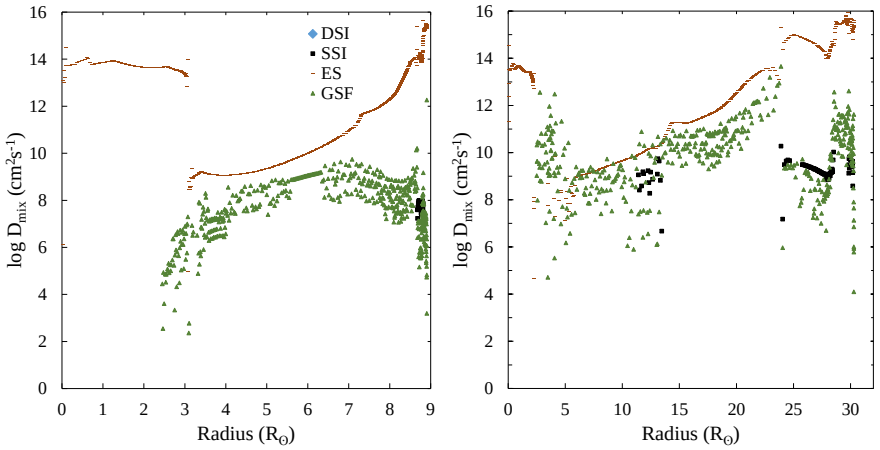

Figure 4.5: Plot of Log of the diffusion coefficients vs stellar radius for a $40M_{\odot}$ with $v_{init} = 200$ km s^{-1} at $\sim 10^5$ years left and at TAMS right.

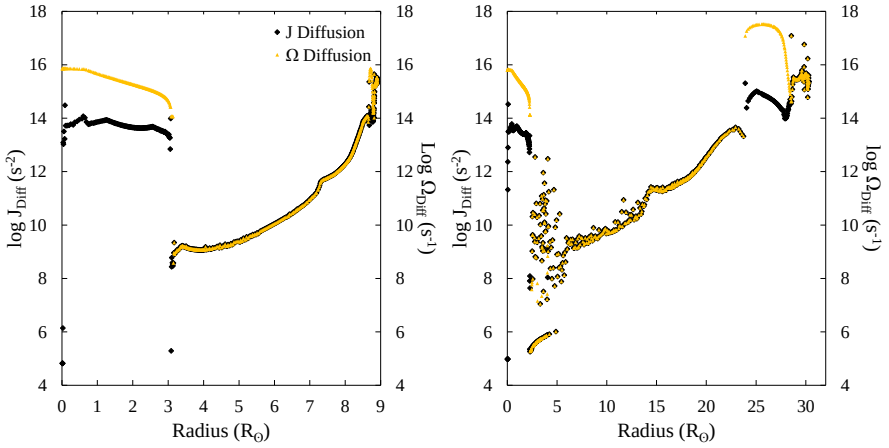

Figure 4.6: Combined diffusion coefficients versus radius for Ω and J diffusion for the model discussed in Figure 4.5

$$\nu = \nu_{conv} + \nu_{sem} + \nu_{over} + \nu_{DSI} + \nu_{SHI} + \nu_{SSI} + \nu_{ES} + \nu_{GSF} \tag{4.15}$$

The final two parameters are: f_ν, the angular momentum transfer factor and f_μ, the ∇_μ factor. f_ν is set to one for both Higgins & Vink (2019) and Brott et al. (2011). f_μ is a factor designed to adjust the sensitivity that rotation has on μ gradients.

This implies that angular momentum diffusion transfers all the angular momentum caused by the instabilities and circulations. Instead of the original definition of ∇_μ, its magnitude can now can be adjusted by f_μ given by $f_\mu \nabla_\mu$ (Heger et al. 2000). This parameter is set to 0.1 in both Higgins & Vink (2019) and Brott et al. (2011). The parameter values have been restricted by observations of surface abundances of nitrogen and helium for galactic O-type stars (Yoon et al. 2006). Figures 4.4 and 4.6 shows how the diffusion evolution of Ω and rotational angular momentum J_{rot} are effected when the circulations, instabilities, and rotation adjusting coefficients (f_μ and f_ν), are implemented.

4.4 Critical Velocity

A star is not solid, but gaseous. Therefore if spun up fast enough it can become oblate and even lose matter. As discussed above, $\vec{g}_{eff}$, excluding stellar luminosity effects, is dependent upon the centrifugal and gravitational forces on the star. When the rotation is high enough these two will become equal and therefore $\vec{g}_{eff} = 0$. The rotational speed at this condition is called the critical velocity defined in terms of rotational velocity Ω. The condition for Ω_{crit} as defined in Maeder & Stahler (2009):

$$\Omega_{crit}^2 = \frac{GM}{r^3} \tag{4.16}$$

MESA includes radiation pressure in equation 4.16 and therefore another term is included in g_{eff}. The new term includes the luminosity and Eddington luminosity (L_{Edd}) at which the outward force caused by radiation pressure is equivalent to the gravitational force going inward. The new equation is (Paxton et al. 2013):

$$\Omega_{crit}^2 = \Gamma_{factor} \frac{GM}{r^3} \tag{4.17}$$

$$\text{Where} \quad \Gamma_{factor} = (1 - \frac{L}{L_{Edd}}) \quad \text{and} \quad L_{Edd} = \frac{4\pi cGM}{\kappa} \tag{4.18}$$

As explained at the beginning of this section, rotation effects the spherical symmetry, and near Ω_{crit} this is at its maximum. The theoretical maximum equatorial radius a star could obtain is 1.5 times the polar radius (Newton 1642-1727). A plot of Ω vs. equatorial radius from Georgy et al. (2011) is shown in Figure 4.7. Higher Ω creates a larger deviation from r_p on the equator. At rotation velocities around this value the star will experience excess limb darkening, where T_{eff} at the equator will be less than at the poles. Limb darkening happens for non-rotating, solid body and differential rotating stars.

Maeder & Meynet (2012) describe a limitation on the 1D shellular approximations when stars are rotating near their critical velocity, because as shown in Figure 4.7, isobars deviate from spherical symmetry. Paxton et al. (2013) explain for stars near this rotational velocity the reliability of the models are uncertain. The stars in this study do not rotate near their critical velocity. Therefore it is still reasonable to use

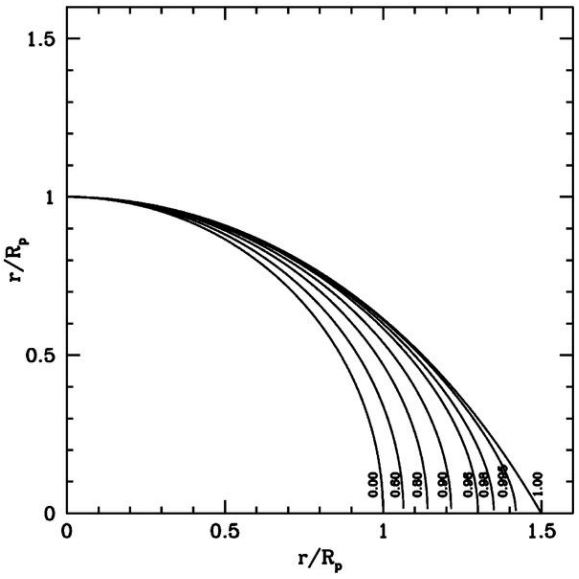

Figure 4.7: A plot of different initial rotating modeled stars. The y-axis shows the polar radius, equal to 1 and the x-axis shows the equatorial.

the 1D shellular approximation.

Table 4.1 summarizes the different coefficient values discussed above and the variables used in this work. Note in Table 4.1: "1" in the table implies MESA will calculate the diffusion coefficient for elements and/or angular momentum and "0" implies do not calculate the coefficient. Appendices A and B show the inlist syntax for the instabilities and circulations, where the acronym am is for angular momentum diffusion and D is for elemental diffusion.

Table 4.1: Rotation Parameters

Models	DSI	SSI	ES	GSF	ST	v_{surf} (km s^{-1})	f_μ	f_c
Brott	1	1	1	1	1	$0.4v_{crit}$	0.1	0.0228
Higgens & Vink	1	1	1	1	0	(0-500)	0.1	$0.0\bar{3}$

Brott uses the ST-Dynamo only for mixing of angular momentum and not for elemental mixing

Chapter 5

Binary Model

The majority of high mass stars ($M \geq 16\mathrm{M}_{\odot}$) observed in the night sky, are either in binary or multiple star systems (Duchêne & Kraus 2013). Binary star systems exhibit fascinating physical phenomenon not shown in single star systems. They can go through multiple different types of evolutionary phases and different paths of evolution depending on the star's separation distance and masses. In this work the stars are close enough that they experience extreme tidal torques that increase the binary separation (a), slow down the initial stellar rotation velocity, and increase mass loss through winds. Mass loss from the system also creates orbital angular momentum loss ($\dot{J}_{orb}$) and increases the separation. Tidal torque is one of the physical phenomena a close binary star system can experience. Depending on the separation distance of the binary system, the system will experience RLOF, where the more massive star evolves and begins donating matter to the less massive star. This processes has the most profound impact on a binary systems e.g., large changes in separation distance, masses, rotation velocity, and orbital angular momentum, in a short amount of time. The rate at which J_{orb} changes is influence by: gravitational radiation, magnetic breaking of both stars, spin orbit coupling, wind mass transfer, and inefficient mass transfer. In the following sections equations are defined and then simplified by the assumption that eccentricity e of all models are zero, implying a circular orbit. The assumption of $e = 0$ is valid due to strong tidal forces enforcing circularization of the

orbit (discussed in section 5.2.1).

5.1 Orbital Period & Separation Evolution

To initiate a model binary system in MESA the user must either define the orbital separation or the orbital period and also the initial masses of the stars. The majority of the basic physics of binary systems can be modeled by orbital mechanics and described accurately by the generalized form of Kepler's three laws of motion. To model the evolution of orbital period P_{orb} and a the general form of Kepler's third law of motion is used.

$$P_{orb}^2 = \frac{4\pi^2}{G(M_1 + M_2)} a^3 \tag{5.1}$$

M_1 and M_2 are the primary star and secondary star masses, respectively. Varying the total mass of the system while keeping the period constant implies the orbital separation will change. The longer the period, with mass held constant, the wider the separation of the system. In Equation 5.1 all physical quantities are varying in a binary model, M_1 and M_2 are changing due to the winds explained in chapter 6, and a and P_{orb} are changing due to mass loss, tidal torques, and other orbital dissipation physics discussed below.

The relationship between ω_{orb} and P_{orb} can be written in the following way:

$$\omega_{orb}^2 = \frac{4\pi^2}{P_{orb}^2} \tag{5.2}$$

Dividing both sides by π^2 in Equation 5.1 and using Equation 5.2, ω_{orb}^2 can be expressed as:

$$\omega_{orb}^2 = \frac{G(M_1 + M_2)}{a^3} \tag{5.3}$$

The square of J_{orb} is dependent ω_{orb}^2, the masses of the two stars, and a:

$$J_{orb}^2 = M_1 M_2 a^4 \omega_{orb}^2 \tag{5.4}$$

Substituting Equation 5.3 into Equation 5.4 and taking the square root yields the expression used by MESA (Paxton et al. 2015):

$$J_{orb} = M_1 M_2 \sqrt{\frac{Ga}{M_1 + M_2}} \tag{5.5}$$

To compute the evolution of the binary system, the evolution of the separation distance, and then the orbital period evolution, Paxton et al. (2015) model the evolution of $\dot{J}_{orb}$, through the varying quantities such as $\dot{M}_1$ (Mass loss or gain of the star), $\dot{M}_2$ (mass gain or loss of the secondary), S_1 , and S_2 (spin angular momentum of the primary and secondary stars). The varying quantities are affected by high wind mass loss, tidal torques, and spin-orbit coupling.

The following expression is used by MESA to model $\dot{M}_1$ and $\dot{M}_2$ in the binary model Paxton et al. (2015):

$$\dot{M}_1 = \dot{M}_{1,W} + \dot{M}_{RLOF}, \qquad \dot{M}_2 = \dot{M}_{2,W} - f_{mt}\dot{M}_{RLOF} \tag{5.6}$$

Here $\dot{M}_{1,W}$ and $\dot{M}_{2,W}$ are mass loss due to the primary star and secondary star winds, $\dot{M}_{RLOF}$ is mass loss due to RLOF and f_{mt} is a mass transfer efficiency parameter. Roche lobe overflow is not studied in this thesis so Equation 5.6 becomes:

$$\dot{M}_1 = \dot{M}_{1,W} \quad \text{and} \quad \dot{M}_2 = \dot{M}_{2,W} \tag{5.7}$$

Therefore changes in mass and binary mechanics due to mass loss are only because of massive stellar winds.

5.2 Orbital Angular Momentum Evolution

The orbital angular momentum of a binary system can change drastically if the stars separation distance is small. For massive compact binary models $\dot{J}_{orb}$ is effected by tidal torques, magnetic breaking of the gainer star, and inefficient mass transfer (matter loss from the system). The sections below present the theory and algorithms used in MESA to model $\dot{J}_{orb}$.

5.2.1 Tidal Torque & Synchronization

A tidal torque is created when two spherical celestial bodies create a strong differential gravitational force on each other. A wonderful example is the Moon and Earth's differential force on one another, which causes both the Moon and Earth to deviate from spherical symmetry. The Earth deviates ≈ 10 cm from spherical symmetry, and the Moon's deviation is ≈ 20 m (Carroll & Ostlie, 2007). The oceans exhibit the

greatest effect of the differential pull and create a bulge along the axis of the Earth and the Moon. However, bulges of the oceans do not follow a straight line to the Moon. This is because the Earth's rotation rate is faster than the Moon's orbital rate, so there is an angle between the tidal bulge and the Moon Earth-line. This slows down the rotation of the Earth due to friction caused by moving bulge along the surface of the Earth. Thus, angular momentum is transferred to the lunar orbit and the Earth-Moon separation distance grows.

In binary star systems, if the two stars are not tidally synchronized, they will experience a tidal torque. When the rotation rate of both stars is equal to the orbital velocity the system is said to be tidally locked. When the system is tidally locked no differential gravitation force will exist and therefore no tidal torque.

The full derivations and explanations of tidal effects in binary models are lengthy and mathematically intensive. To avoid this, the equations used in the model will be stated, and the papers where they are derived cited. This thesis focuses on the dynamical tides through radiative dissipation (Zahn 1975). Tidal torque requires a dissipation mechanism, such as the friction of the oceans on the surface of the Earth; for a star it is dependent upon viscous dissipation driven by either convection or radiation. Massive stars release a tremendous amount of radiation during the hydrogen burning phase and therefore dissipation by radiation is appropriate. Paxton et al. (2015) uses the expression from Hut (1981):

$$\dot{\Omega}_j = \left[\frac{3q^2}{r_g} \frac{k_a}{T_{typ}} \left(\frac{R_j}{a} \right)^6 \right] \tag{5.8}$$

$j = 1$ for the primary star. k_a is the apsidal motion constant of the primary star (Lecar et al. 1976), $q = \frac{M_2}{M_1}$ is the mass ratio of the two stars, and r_g is the radius of gyration (a unitless quantity) defined as:

$$I = M(r_g R)^2 \tag{5.9}$$

Apsidal motion is an oscillation of an elliptical orbit. For example the Moon, when orbiting the Earth, does not have the same orbital trace as the previous orbit. If apsidal motion exists, and if trace one is defined as orbit 1, and the next trace, orbit 2, then these two traces will not be the same. T_{typ} is the time scale in which significant changes occur in the orbital period. It is also known as the viscous dissipation timescale (Hut 1981) defined as:

$$T_{typ} = \frac{R^3}{GM\tau} \tag{5.10}$$

τ is the time lag of the tides. Equations 5.8-5.10 are all calculated in terms of the primary star and do not include differential rotation. Paxton et al. (2015) modified Equation 5.8 to involve the secondary star and differential rotation by the following expression:

$$\dot{\Omega}_{k,j} = \frac{\Omega_{orb} - \Omega_{k,j}}{\tau_{sync,j}}, \qquad \frac{1}{\tau_{sync,j}} = \frac{3}{(q_j r_{g,j})^2} \left(\frac{k_a}{T_{typ}}\right)_{c,j} \left(\frac{R_j}{a}\right)^6 \tag{5.11}$$

Here the index $j = 1, 2$ for the primary star and secondary star. The index k represents a specific cell of the interior of the star, as discussed in Chapter 3. $\tau_{sync,j}$

is the synchronization timescale which is the time it takes the stars' rotation to synchronize to their orbit. This is related to the circularization timescale, which is the time for the orbital eccentricity to effectively become 0.

The eccentricity of the system can be assumed to be 0 because the circularization timescale is short compared to the age of the stars. For example, using equation (43-45) in Hurley et al. (2002) and values from the models where $R \approx 8\mathrm{R}_{\odot}$, $M = 35\mathrm{M}_{\odot}$, $a \approx 41.5\mathrm{R}_{\odot}$, $q = 0.714$, and assuming that $\frac{MR^2}{I} = 14.3$, which is the value for the Sun, then $\tau_{circ,1} \approx 3.2 \times 10^5$ yrs. The secondary star's circularization timescale is approximately equal to the primary star. This is short compared to the models' full evolutionary timescale of ~ 7 Myrs.

The final term to discuss is $\left(\frac{k_a}{T_{typ}}\right)_{c,j}$ which is the convective viscous damping term from Hurley et al. (2002). Appendix C shows the various options that can be set for modeling the tidal interactions between both stars. This work adopts the value from Hut (1981), but instead of the convective dampening term ($\frac{k_a}{T_{typ}}$) defined in Equation 5.11 the term is:

$$\left(\frac{k_a}{T_{typ}}\right)_r = 1.9782 \times 10^4 \frac{MR^2}{a^5}(1+q_2)^{5/6} E_2 \quad yr^{-1} \tag{5.12}$$

Where $E_2 = 1.592 \times 10^{-9} M^{2.84}$ is the second-order tidal coefficient from Zahn (1977) . Equations 5.11 and 5.12 have a strong dependence on the separation. Plugging Equation 5.12 into 5.11 gives relationship of $\frac{1}{a^{11}}$. Therefore a decrease in orbital separation by a factor of 2 increases $\dot{\Omega}_{i,j}$ by a factor 2048. Also, the greater the

difference between Ω_{orb} from $\Omega_{i,j}$ the larger is $\dot{\Omega}_{k,j}$. If $\Omega_{rot} \gg \Omega_{orb}$ at the beginning then tidal effects will be strongest then. In addition, tidal torques can have drastic effects on the modeled stellar interior because of the inclusion of differential rotation. This enhances the mixing of heavy elements to the surface.

5.2.2 Spin-Orbit Coupling

Spin-Orbit coupling follows from the conservation of angular momentum. For a system not subjected to mass loss or RLOF the equation is (Paxton et al. 2015):

$$\delta J_{orb} = -\delta S_1 - \delta S_2 \tag{5.13}$$

However if mass loss is present the equation used by MESA, modified due to the absence of RLOF, for Spin-Orbit coupling is (Paxton et al. 2015):

$$\dot{J}_{ls} = -\frac{1}{\delta t}\left(\delta S_1 - S_{1,lost} + \delta S_2 - S_{2,lost}\right) \tag{5.14}$$

Where the δt is the timestep and δS_1 and δS_2 are the changes in spin in the timestep. Both spins of the stars are affected by the angular momentum loss or gained due to wind mass lost and tidal forces discussed in the previous section.

5.2.3 Mass Loss

Mass loss in a binary system can either be conservative, meaning when mass is being transferred between the two stars none is lost from the system, or nonconservative,

where some matter leaves the system entirely. Since both stars experience wind mass loss, the system is nonconservative. This has drastic affects on the evolution of the orbital parameters e.g., J_{orb}, S, a, and P_{orb}. Paxton et al. (2015) follow the work of Soberman et al. (1997) modeling the effects of mass loss in a binary model. The expression is in terms of the change in orbital angular momentum due to mass loss and is defined as:

$$\dot{J}_{ml} = \left[(\dot{M}_{1,W} + \alpha_{mt}\dot{M}_{RLOF})M_1^2 + (\dot{M}_{2,W} + \beta_{mt}\dot{M}_{ROLF})M_2^2\right] \frac{a^2}{(M_1+M_2)\frac{2\pi}{P_{orb}}} + \gamma_{mt}\delta_{mt}\dot{M}_{RLOF}\sqrt{G(M_1+M_2)a} \quad (5.15)$$

Here $\alpha_{mt}, \gamma_{mt}, \delta_{mt}$, and $\dot{M}_{RLOF}$ are the efficiency of mass transfer coefficients in the vicinity of the donor, accretor, circumpolar toroid, and the mass loss due to RLOF, respectively (Paxton et al. 2015). As discussed, mass transfer by Roche Lobe Overflow is not studied, therefore Equation 5.15 can be rewritten as:

$$\dot{J}_{ml} = \left[\dot{M}_{1,W}M_1^2 + \dot{M}_{2,W}M_2^2\right] \frac{a^2}{(M_1+M_2)} \frac{2\pi}{P_{orb}} \quad (5.16)$$

Note, discussed in the next Chapter, wind mass transfer is permitted in the models, but is not considered in the above equation.

5.2.4 Wind Mass Loss

The final contribute to $\dot{J}_{orb}$ considered in this study is angular momentum loss due to winds. Because winds remove the surface material of both stars they therefore

remove angular momentum as well. However when mass transfer is included, and if the net mass loss or gain does not remove the surface, then angular momentum loss is incorrectly modeled in the system. The wind mass loss option defined in MESA compensates for this allowing angular momentum to be lost from the star due to winds even if mass is being transferred onto its surface.

This option is required because wind mass transfer happens when both stars experience bi-stability jumps (Chapter 6), because one star is losing more matter then the other (thoroughly discussed in section 6.3.2 and Chapter 7).

Sections 5.2.1-5.2.4 complete the binary modeled mechanics used in this work, contributing to $\dot{J}_{orb}$ through: $\dot{M}_1$, $\dot{M}_2$, $\dot{\Omega}_{orb}$, and $\dot{\Omega}_j$. In addition to understanding $\dot{J}_{orb}$, the previous sections also provide information about the binary system evolution e.g., the evolution of a, P_{orb}, q, and M_{sys} (system mass). Finally $\dot{J}_{orb}$ can be summed in the following way:

$$\dot{J}_{orb} = \dot{J}_{ls} + \dot{J}_{ml} + \dot{J}_{mw} \tag{5.17}$$

5.2.5 Magnetic Breaking

Equation 5.17 represents all contributors to the change in the orbital angular momentum in this work. Magnetic breaking ($\dot{J}_{mb}$) and gravitational wave radiation $\dot{J}_{gw}$, are neglected. The gravitational wave radiation is insignificant in magnitude when comparing to the other contributors to $\dot{J}_{orb}$. Magnetic breaking can have a significant impact on the binary model and the reason it is not included needs to be addressed.

When there exists both a strong magnetic field and stellar wind a processes known

as magnetic breaking will occur. The ionized gases from the wind will follow along open fields out to the Alvén radius. This radius is defined when $v_\infty = v_A$ where v_A is the Alvén velocity:

$$v_A = \frac{B_A}{\sqrt{4\pi\rho_W}} \tag{5.18}$$

B_A and ρ_W are the magnetic field on the Alvén surface and the density of the wind. The wind material follows the magnetic field lines at a constant velocity, instead of slowing down with distance, and carries with it angular momentum from the material of the surface of the star. This is extremely efficient at slowing down the spin of the modeled star.

MESA is unable to model both spin orbit coupling and magnetic breaking. Paxton et al. (2015) follow the work of Rappaport et al. (1983) who assume the two stars to be initially tidally locked, which is not assumed in this work. However, an order of magnitude argument can be made to not include magnetic breaking in the models. The equation used by Paxton et al. (2015) is:

$$\dot{J}_{mb} = -6.82 \times 10^{34} \left(\frac{M_1}{M_\odot}\right) \left(\frac{R_1}{R_\odot}\right)^{\gamma_{mb}} \left(\frac{1d}{P_{orb}}\right) \text{dyn cm} \tag{5.19}$$

For the start of one of the models the primary star has $R \approx 8\text{R}_\odot$, $M_1 = 35\text{M}_\odot$, and $P_{orb} = 4$ days and therefore $\dot{J}_{mb} \approx -2 \times 10^{37}$ dyn cm. Now for the same system $\dot{J}_{ml} \approx -10^{41}$ dyn cm which is approximately four orders of magnitude larger. Magnetic breaking would only contribute $\approx 0.02\%$ to the overall change in $\dot{J}_{orb}$, thus it is reasonable to argue magnetic breaking can be ignored for this work .

Chapter 6

Massive Star Winds

Massive stars are thought to be the cosmic engines that drive star formation in a galaxy by dumping large amounts of matter and energy into the ISM. This leads to the ionization of the ISM which can be observed as shock fronts and "wind-blown bubbles". Massive stars also enrich the ISM with metals from their processed nuclear material. This is important for theories of the evolution of the early universe and galaxy formation. There are two cases for high mass loss from massive single stars. One, mass is lost due to their winds. Two, at the end of their lives, massive stars explode as supernovae ejecting a tremendous amount of matter at an extremely high velocity.

A star will have winds if $\vec{g}_{rad} + \vec{g}_{pressure} > \vec{g}_{grav}$ near the photosphere. That is, the acceleration of matter outward due to radiation and gas pressure is greater than the acceleration due to gravity inward. Matter will be continually accelerated outwards beyond the photosphere until the radiative acceleration becomes minimal and then it will move at a constant velocity (v_∞) out to “infinity” (Milne 1926).

The amount of radiation generated in a star's core, the physics of the photosphere, and the opacity play a large role in the value for v_∞ and the mass loss $\dot{M}_W$. In the following sections I will explain the equations of massive star winds and their importance to this study. The majority of the next section's theory is based on Puls et al. (2008) and Vink (2015).

MESA models stars, and not the physics and dynamics of the ISM. Approximations and assumptions, discussed in the last section, must be made to model shocks and wind-blown bubbles and to compare to observations.

6.1 Line Driven Winds

Wind theory was first discussed by Milne (1926), who argued that photons carried momentum and transferred this to metal ions in the photosphere of massive stars, thus creating winds. However, according to Lucy & Solomon (1970) and Castor et al. (1975) (CAK) if the moving metal ions in the photosphere were to transfer momentum to the more abundant helium and hydrogen atoms this would significantly increase $\dot{M}_W$ (Puls et al. 2008). The equation of momentum transfer between photons, ions, and free electrons can be defined as:

$$\Delta p = h/c(v_{in}\cos\theta_{in} - v_{out}\cos\theta_{out}) \tag{6.1}$$

Here h is Planck's constant and c is the speed of light. v_{in} and v_{out} are the velocity of the ions or free electrons before and after the momentum transfer due to the photon at angles of θ_{in} and θ_{out}. The change in the angle from absorption to re-emission of photons on an metal ion and the Doppler effect is the framework of momentum transfer by line[1] driving. Integrating over all line scatterings or rather all re-emission losses and gains provides an acceleration in radial direction defined as g_{rad}^{line}.

[1]Stellar absorption or emission **lines** are created by discrete transitions of electrons in atoms

Under specific criteria (see Puls et al. 2008) the theory of line driven winds can be modeled by the 1D fluid approximation. This approximation assumes the wind is homogeneous, stationary, of uniform density, and spherically symmetric. The density is assumed to be high enough that there is sufficient transfer of momentum due to Coulomb interactions between metal ions and helium and hydrogen atoms. There is an increase in momentum of heavier elements, due to the absorption of photons, that exists when the spectral energy distribution peaks in the UV. Therefore heavy elements are able to distribute a large amount of momentum to the more abundant helium and hydrogen atoms in the photosphere. The continuity and momentum balance equations are needed to model winds for the 1D fluid approximation. The continuity equation is defined as:

$$\dot{M} = 4\pi r^2 \rho(r) v(r) \tag{6.2}$$

The above equation states that the amount of matter entering an area has to be equal the amount of matter leaving that area. Next is the momentum balance equation for a static case:

$$v\frac{dv}{dr} = -\frac{GM}{r^2} - \frac{1}{\rho}\frac{dP}{dr} + g_{rad} \tag{6.3}$$

Where $g_{rad} = g_{rad}^{line} + g_{rad}^{cont}$ is the radiative acceleration due to line driving and the continuum[2]. The equation of state can be expressed as $P = v_s^2 \rho_W$, where v_s is the

[2]A free electron has no specific energy required to make bound-free, free-free, and free-bound transitions and therefore photons of any wavelength can create these transition. Therefore a continuum of radiation will be created.

isothermal speed of sound. A simple definition of the speed of sound for an ideal gas is:

$$v_s = \sqrt{\frac{\gamma P}{\rho}} \tag{6.4}$$

For an ideal monotonic gas $\gamma = \frac{5}{3}$. Using Equations 6.4 and 6.2 and substituting them into Equation 6.3 (see Puls et al. 2008) this becomes:

$$(1 - \frac{v_s^2}{v^2})v\frac{dv}{dr} = -\frac{2v_s^2}{r} - \frac{dv_s^2}{dr} - \frac{GM}{r^2} + g_{rad} \tag{6.5}$$

Using Equation 6.5 to derive $\dot{M}$ and v_∞ proves to be challenging. The difficulty lies in accurately modeling g_{rad} (Vink 2015 and Puls et al. 2008).

The first step, in order to find a solution to g_{rad}, is determining the Thomson acceleration for free electrons using the Thomson opacity (Puls et al. 2008). The Thomson opacity is $\sigma_e = \frac{n_e \sigma_T}{\rho}$, which is given units of cm^2/g. Here $\sigma_T = 6.652 \times 10^{-25}\text{cm}^2$ is the Thomson free electron cross section. The Thomson acceleration from Puls et al. (2008) is defined as:

$$g_{rad}^{TH} = \frac{1}{c\rho}\frac{\sigma_e L}{4\pi r^2} = g_{grav}\Gamma \tag{6.6}$$

Here Γ is the Eddington's parameter (see Equation 4.18). However, free electron scattering is not the strongest contributor to g_{rad}. Line scattering by photons is. This is because the cross section of a free electron is much smaller than the cross section of an atom for a photon that is at the energy for an allowed transition for

a bound electron in that atom. Even though this only works for a very narrow band of photon frequencies per transition, it can still be magnified significantly when integrated over all frequencies and for different metal ions in the photosphere. In addition, the strength of the line driving is amplified due to the Doppler shifts at varying stellar wind radii. This is due to photons impacting on moving atoms which broadens the allowed frequencies for the bound-bound transitions to take place. To give an example of the magnitude difference, writing the ratio of the force of line driving by bound electrons over free electrons (known as the "Q-value") from Gayley (1995):

$$Q_{value} = \frac{F_{bound}}{F_{free}} \propto \frac{\nu_i}{f_i} \tag{6.7}$$

f_i and ν_i are the transition frequency and line frequency, respectively. For hot star winds (peaking in the UV) $f_i \sim 10^7$ s^{-1} and $\nu_i \sim 10^{15}$ s^{-1} giving $Q_{value} \sim 10^7$. Therefore the force provided by a bound electron is 10^7 larger than a free electron.

The line acceleration equation stems from the Sobolev (1960) approximation; which assumes that the local physical quantities and velocity gradient (dv/dr) do not vary over a length of $\Delta r \approx \frac{v_{th}}{(dv/dr)}$ known as the Sobolev length (see Puls et al. 2008 for a more in depth explanation). v_{th} for an ideal gas is:

$$v_{th} = \sqrt{\frac{k_b T}{m}} \tag{6.8}$$

where k_b is the Boltzmann constant and m is the mass of the particle. Therefore the line acceleration for a single line of frequency ν and with line optical depth τ_ν can be expressed as:

$$g_{rad,i}^{line} = \frac{L_\nu \nu}{4\pi r^2 c^2} \left(\frac{dv}{dr}\right) \frac{1}{\rho}(1 - e^{-\tau_\nu}) \tag{6.9}$$

Here L_ν is the luminosity of a specific line frequency. $\tau = \frac{\bar{\kappa}}{(dv/dr)}$ where $\bar{\kappa}$ and λ are the frequency integrated line-opacity and wavelength of transition, respectively. τ_ν, is the optical depth, for which Carroll & Ostlie (2007) give a nice explanation: "The optical depth may be thought of as the number of mean free paths from the original position to the surface, as measured along the ray's path." See Equation 2.6 for the definition of mean free path l. When $\tau_\nu \gg 1$ the gas is optically thick, which means it takes longer for a photon to escape from the star. Where as a gas is optically thin when $\tau_\nu \ll 1$. For Equation 6.9 when the lines are optically thin then the $g_{rad,i}^{line}$ has the same $1/r^2$ dependence as Equation 6.6. However when the lines are optically thick then $g_{rad,i}^{line}$ depends on dv/dr see (Puls et al. 2008).

To determine the total acceleration of all the lines following CAK, who used a line-strength distribution function to sum over all lines, the total g_{rad}^{line} expressed as the ratio of total line acceleration over the Thomson acceleration is:

$$\frac{g_{rad}^{line}}{g_{rad}^{TH}} = M(t) = k_f \left(\frac{\sigma_e v_{th}}{dv/dr}\right)^{-\alpha_T} \tag{6.10}$$

The above equation is a power law distribution for modeling the line acceleration. See a more detailed explanation in Castor et al. (1975) or Puls et al. (2000). k_f and $M(t)$ are force multipliers. k_f is defined as the measure of the number of lines stronger than Thomson scattering. α_T can be seen as the ratio of the line acceleration of optically thick lines over the sum of all lines (Puls et al. 2008). Using Equations 6.5 and 6.10 to derive the velocity of the wind as a function of r, v_∞, and $\dot{M}_W$ and expressing them for the CAK method gives:

$$v(r) = v_\infty \left(1 - \frac{R}{r}\right)^{0.5} \tag{6.11}$$

$$v_\infty = \left(\frac{\alpha}{1-\alpha_T}\frac{2MG(1-\Gamma)}{R_\star}\right)^{0.5} = \left(\frac{\alpha_T}{1-\alpha_T}\right)^{0.5} v_{esc} \tag{6.12}$$

$$\dot{M}_W = (kL)^{1/\alpha'} \left(M(1-\Gamma)\right)^{1-1/\alpha'} \tag{6.13}$$

Here $\alpha' = \alpha_T - \delta_i$. The δ_i parameter can be thought as describing the ionizion in the wind. α_T, k_f, and $\delta_i a$ all have to be determined observationally. According to Puls et al. (2008) for O-stars, the parameter $\delta_i = 0.1$ and if $\alpha_T \approx 2/3$ therefore gives $\alpha' \approx 0.6$. However the power law solution does not always model the lines well due to various dependencies, e.g. α_T as a function of metallicity $\alpha_T(Z)$ (see for instance Vink et al. 1999 and Vink et al. 2001 for a metallicity dependent wind).

Note that MESA solves for v_∞ in a different way. It assumes $\dot{M}_W$ is already defined by an algorithm set by the user (discussed in the next section). Then it calculates v_∞ in the following way:

$$v_\infty = \frac{\kappa_s \dot{M}_W}{4\pi R_\star \tau_\infty} \tag{6.14}$$

Where τ_∞ and κ_s is the optical depth and opacity just below the surface of the star.

6.2 Metal Dependent Winds

Following the previous derivation from section 6.1 (see Vink et al. 2001 for full derivation) the theory for line driven winds for $\dot{M}$ and v_∞ can be written in terms of the metallicity Z of the star. A general expression of Equation 6.10 which accounts for ionization effects of the wind becomes:

$$M(t) = k_f \left(\frac{\sigma_e v_{th}}{dv/dr} \right)^{-\alpha_T} \left(\frac{n_{e11}}{W} \right)^{\delta_i} \tag{6.15}$$

Here n_{e11} is the electron density given in units of 10^{11} cm^{-3}. W is the dilution factor and δ_i is discussed in Section 6.1. W is meant to account for departures from local thermal equilibrium (LTE) due to the dilution of the continuum radiation (Castor et al. 1975). For example, when the lines of hydrogen are optically thin, then the hydrogen line radiation escapes which creates a departure from LTE. Puls et al. (2000) and Abbott (1982) showed that the force multiplier parameter k_f can be written as a function of metallicity, Vink et al. (2001) defined it as:

$$k_f(Z) \propto Z^{1-\alpha} \tag{6.16}$$

From Equation 6.13 it can be shown that $\dot{M} \propto (k_f)^{1/\alpha'}$. Therefore the relationship between $\dot{M}$ and Z can be expressed in the following way (Vink et al. 2001):

$$\dot{M}_W \propto Z^m \tag{6.17}$$

Where $m = \frac{1-\alpha_T}{\alpha_T-\delta_i}$. For the values discussed above $m \approx 0.8$ for O-stars. However according to Vink et al. (2001) the force multiplier α_T is also dependent on Z therefore v_∞ is dependent on metallicity. They state that $v_\infty \propto Z^q$ where q is an adjustable parameter. However according Vink et al. (2001) there are specific conditions where Equations 6.16 and 6.17 might not always hold true. The limits include at high and low Z values. For high Z a continual increase in Fe abundance may no longer provide a significant increase in $\dot{M}_W$ and v_∞. For lower Z values Fe may no longer dominate, but C, N, and O lines, though weaker then the driving force of Fe lines, may start to be the main contributors to $\dot{M}_W$ and v_∞. The Vink et al. (1999) and Vink et al. (2001) derivation of $\dot{M}_W$ follows the work of CAK, but they use an improved Sobolev approximation code to follow the theory. See Vink et al. (1999) for a detailed description of their approach.

6.2.1 Bi-Stability Jumps

Pauldrach & Puls (1990) discovered that at a temperature around 19.3 kK when modeling P-Cygni, a luminous blue variable, there were jumps in both v_∞ and $\dot{M}_W$. Later Lamers et al. (1995) showed that at around 21 kK there are significant changes; either $\dot{M}_W$ decreased but terminal velocity increased, or $\dot{M}_W$ was lower but v_∞ was higher.

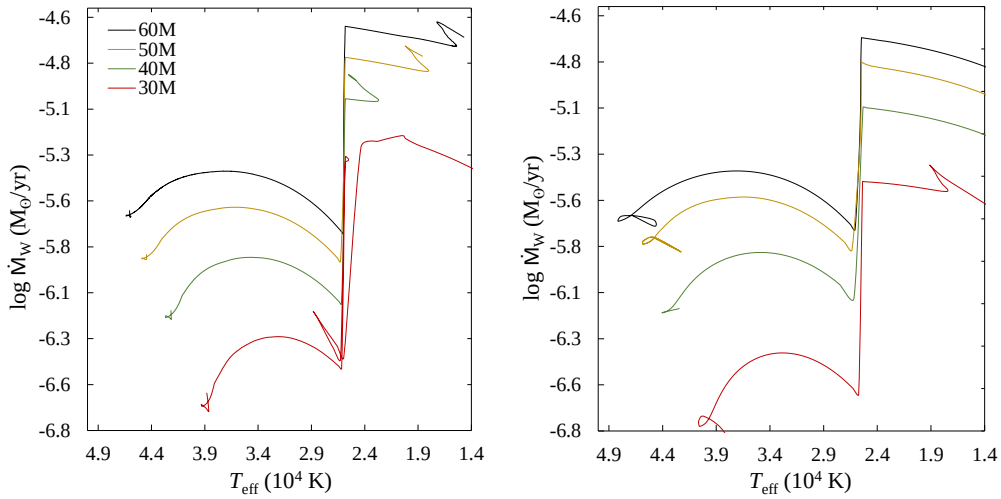

Figure 6.1: Single star models of the Bi-stability jump for Higgins & Vink (2019) left and Brott et al. (2011) right. The difference between the jumps depends upon the different abundances, wind scheme, and initial parameters used. For example, a stark contrast can be seen for the $30M_\odot$ model.

The physical reasons for these "bi-stability jumps" are described in Vink et al. (1999). From their models Vink et al. (1999) determined that C, N, and O are important line drivers in the supersonic part of the wind that contribute to the line acceleration in massive stars. They are also important for lower Z winds. For the subsonic part of the wind Fe lines are the most important line drivers. In addition they note specifically that $\dot{M}_W$ is dependent on the subsonic part of the wind and v_∞ is dependent on the supersonic. Therefore $\dot{M}_W$ is dependent heavily on line acceleration of Fe.

The bi-stability jump is dependent on Fe lines because at around 21 kK FeIV (tripley ionized Fe) recombines to FeIII (doubly ionized Fe). FeIV lines contribute to $\dot{M}_W$ in the extreme ultraviolet (EUV) when the stars T_{eff} is high, such as at

the beginning of the $40M_{\odot}$ model in Figure 6.1. Even though it has few scattering lines, the majority of Fe is ionized to FeIV. As the star's T_{eff} evolves closer to 21 kK (T_{Jump}) then the peak of SED is in the UV so FeIV recombines to FeIII making a higher ρ, but lower v_{∞}. Also, the optical depth of the wind increases and since FeIII has more scattering lines $\dot{M}_W$ increases. Even though the wind is slower, the jump exists because there is a runaway recombination effect when FeIV recombines to FeIII throughout the wind.

The Vink wind scheme, that includes this jump, is used in this study (Vink et al. 2001). Vink et al. (2001) determined the size of the jump using the ratio of v_{∞}/v_{esc} that was determined by Lamers et al. (1995) for Galactic early-type supergiants to be $v_{\infty}/v_{esc} = 2.3$ and for late-type stars $v_{\infty}/v_{esc} = 1.3$. These values are used in Vink et al. (2001) and in the routine in MESA shown in Appendix D.1. Along with the Vink wind scheme Brott et al. (2011) used the "Dutch" wind scheme, which is based on multiple papers (Glebbeek et al. 2009 and reference therin).

6.3 Enhanced Wind Mass Loss & Binaries

The wind factor, stellar rotation, and tides effect the stellar wind mass loss rate. The wind factor simply increases or decreases the rate of mass loss by taking an $\dot{M}_W$ scheme and then multiplying it by a constant. This can be written in the following way for the Vink et al. (2001) wind scheme programmed in MESA:

$$\dot{M}_{Wf} = f_v \dot{M}_W \tag{6.18}$$

where $\dot{M}_{Wf}$ is the final calculated wind mass-loss rate $\dot{M}_W$ is from the Vink et al. (2001) wind scheme and f_v is known as the Vink factor.

6.3.1 Stellar Rotation

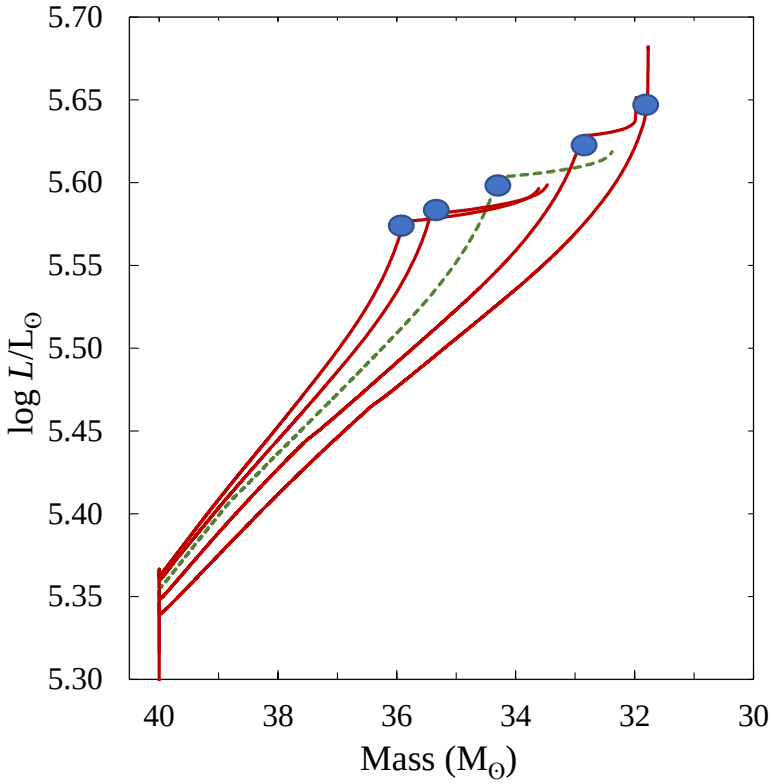

Figure 6.2: Same as Figure 2.5 however enhanced winds due to rotation is used. The blue dots represent TAMS.

Stars that are fast rotators can experience enhanced wind mass loss at the equator. Friend & Abbott (1986) and Bjorkman & Cassinelli (1993) re-derived CAK's theory

for winds to include rotation for a 1D hydrodynamic case. Rotation changes the winds according to Puls et al. (2008) by an increase in mass loss due to deviations from spherical symmetry around the equator. Essentially Equation 6.5 has an added centrifugal term on the right hand side (g_{cent}). This added term is directed outwards at the equator and therefore increases wind mass loss (see Figure 6.2). Therefore the wind mass loss will be largest when the star is near its Ω_{crit}. To include rotation into the wind mass loss, MESA follows the approach of Friend & Abbott (1986) & Bjorkman & Cassinelli (1993) where the wind enhanced mass-loss rate due to rotation prescription is:

$$\dot{M}_W(\Omega) = \dot{M}_W(0) \left(\frac{1}{1 - \Omega/\Omega_{crit}} \right)^{\xi} \tag{6.19}$$

where $\dot{M}_W(0)$ is the wind mass loss with out rotation and ξ is a fitting parameter used by Bjorkman & Cassinelli (1993) to constrain to Friend & Abbott (1986) results. From Bjorkman & Cassinelli (1993) the MESA default value is $\xi = 0.43$ and Ω_{crit} is defined in Equation 4.16. From Equations 6.19 and 4.18 one can see that as a star's luminosity reaches the Eddington Luminosity then $\Omega_{crit} \to 0$ and therefore $\dot{M}(\Omega) \to \infty$. Also, when $\Omega = \Omega_{crit}$ the same divergance will happen. In MESA this problem is resolved by a min function (see Equation (27) in Paxton et al. 2013).

There are different prescriptions for mass loss increased by rotation (see for instance Ekström et al. 2012). In addition gravitational darkening can also be included (Maeder & Meynet 2000). The two different works I am following use Equation 6.19. However Higgins & Vink (2019) do not include Equation 4.16 for matching their re-

sults to observations, but use it for a comparison study. In MESA this mass loss enhanced by rotation is turned on by setting omega_pow = 0.43. When reproducing the results of Higgins & Vink (2019) enhance mass loss due to rotation was not included. However, for Brott et al. (2011) and the various velocity models this is set to the 0.43 value.

Models	$Wind_{hot}$	$Wind_{cold}$	f_v	ξ
Brott	Vink	Dutch	1	0.43
Higgens & Vink	Vink	-	(0.1-3)	(0/0.43)

6.3.2 Tides

There are two cases in a binary models that can be studied: enhanced winds due to tidal forces and wind mass transfer. Introduced below are the equations that model these two mechanisms and examples are provided for each.

Equation 6.5 shows the forces involved to create mass loss through winds. In a binary model when the separation distance is small e.g. for the model presented in the previous Chapter $a \approx 41.5\mathrm{R}_{\odot}$ (determined by $P_{orb} = 4$ days and $M_1 = 35\mathrm{M}_{\odot}$, $M_2 = 25\mathrm{M}_{\odot}$) the stars experience a strong external gravitational force caused by the gravitation attraction of both stars. This adds an additional term to Equation 6.5 that increases wind mass loss rate for both stars and is called tidally enhanced winds. The algorithm used to model enhanced mass loss due to winds is based on Tout & Eggleton (1988):

$$\dot{M}_{tew} = \dot{M}_W \left(1 + B_W \min\left[\left(\frac{R}{R_L}\right)^6, (0.5)^6\right]\right) \tag{6.20}$$

Where $\dot{M}_{tew}$ is the mass-loss rate due to tidal enhanced winds, B_W a tidal enhancement coefficient which can be constrain by observations. In MESA the default is $B_W = 1 \times 10^4$, which is the same as in Tout & Eggleton (1988). $\dot{M}_W$ in Eggleton (1983) is Reimers (1975) wind mass loss rate, but here follows from the Vink et al. (2001) and Glebbeek et al. (2009) prescriptions. R_L is the Roche Lobe radius given in units of solar radii and is defined in Eggleton (1983) as:

$$R_{RL,j} = \frac{0.49 q_j^{2/3}}{0.6 q_j^{2/3} + \ln(1 + q_j^{1/3})} a \tag{6.21}$$

q_j is the mass ratio (for example $q_1 = M_2/M_1$). For the binary discussed in the magnetic breaking section ($R_1 \approx 8\mathrm{R}_\odot$, $M_1 = 35\mathrm{M}_\odot$, $M_2 = 25\mathrm{M}_\odot$ and $a \approx 41.5 R_\odot$), $q_1 \approx 0.714$ implying $R_{RL,1} \approx 14.5\mathrm{R}_\odot$ and finally $\dot{M}_{tew} \approx 157 \times \dot{M}_{1,w}$. Therefore at the beginning of this model the wind mass loss from the primary star is enhanced by two orders of magnitude. This enhancement factor, shown in Appendix C, is applied to both stars.

6.3.3 Wind Mass Transfer

Mass transfer can happen due to the winds of both stars. The wind material, which is lost from both stars and is still in the vicinity of the binary system, can be accreted by either the primary or secondary by passing through the lost mass of the other star. In addition to accreting matter onto either star, wind material can affect the orbital velocity as a source of drag (Bondi & Hoyle 1944). Wind mass transfer is especially

important for massive stellar winds in binary models. The wind mass acceretion used is based on the theory of Bondi & Hoyle (1944) but MESA applies the equations from Hurley et al. (2002):

$$\dot{M}_{2A} = \frac{-1}{\sqrt{1-e^2}} \left(\frac{GM_2}{v_W^2} \right)^2 \frac{\alpha_W}{2a^2} \frac{1}{(1+v_r^2)^{3/2}} \dot{M}_{1,W} \tag{6.22}$$

v_w is the velocity of the wind, which is not the same wind velocity calculated by Vink et al. (2001) or Glebbeek et al. (2009). It is based on a modified escape velocity from Hurley et al. (2002):

$$v_W^2 = 2\beta_W \frac{GM}{R_j} \tag{6.23}$$

Where β_W is based on the spectral type of either the primary or secondary. In MESA β_W is set to 1/8 for both the primary and secondary. v_r^2 is the ratio of the square of orbital velocity to the square wind velocity defined as:

$$v_r^2 = \frac{v_{orb}^2}{v_W^2} \tag{6.24}$$

Where v_{orb} is the binary orbital velocity defined as:

$$v_{orb}^2 = \frac{GM_{sys}}{a} \tag{6.25}$$

Since the orbital eccentricity is set to zero Equation 6.22 becomes:

$$\dot{M}_{jA} = -\left(\frac{GM_j}{v_{W,3-j}^2} \right)^2 \frac{\alpha_W}{2a^2} \frac{1}{(1+v_{3-j}^2)^{3/2}} \dot{M}_{3-j,W} \tag{6.26}$$

The parameter α_W is set to 3/2 following the work of Hurley et al. (2002). Bondi & Hoyle (1944) accretion assumes a spherically symmetric steady-state accretion rate. A condition was created by Hurley et al. (2002) for the case of high eccentricity e such that the secondary, for example, can accrete more than the primary is losing through its winds. Other examples of deviations from the Bondi & Hoyle (1944) theory can be non-uniform density clouds (clumpy winds) and oblate stars due to rotation. Therefore Hurley et al. (2002) created the following condition to account for these inconsistencies:

$$|\dot{M}_{2A}| \leq 0.8|\dot{M}_{1,W}| \tag{6.27}$$

MESA uses 0.5 instead of the 0.8 and generalizes the condition for both stars, thus rewriting Equation 6.27:

$$|\dot{M}_{jA}| \leq 0.5|\dot{M}_{3-j,W}| \tag{6.28}$$

Equation 6.26 and 6.28 are used to model the wind mass transfer in the binary models. Wind mass transfer is important for high mass systems, but the previously mentioned equations work well for two stars with different mass loss rates, such as $\log \dot{M}_1 \approx 10^{-5}$ and $\log \dot{M}_2 \approx 10^{-7}$. However this only happens when the modeled stellar winds experience the bi-stability jump discussed in chapter 7.

6.4 Shocks & Wind Blown-Bubbles

The mass loss rate of O and B stars are so great it can have a significant impact on the surrounding ISM. Shocks and wind blown-bubbles can be caused by supernove,

single O stars, or multiple O stars. Two great observational examples are the Rosetta nebula, shown in Figure 6.4 (multiple stars contributing) and ζ Ophiuchie (an O9 star) shown in Figure 6.5 . These bubbles and shocks are important because they can lead to star formation and re-ionization of the ISM. The radius and expansion rate of the shell are dependent upon the physical properties of the the star's winds and local ISM. When the winds interact with the ISM this can causes a dense shell to form. Wind blown bubbles provide a useful comparison between models and observations.

Most models today use hydrodynamic evolution codes accounting for a multitude of variables e.g., non-uniformity in the density of the ISM and magnetic fields, 2-dimensions to model observed shocks and bubbles. Unfortunately the information provided by MESA does not cover the ISM, therefore assumptions and approximations (more than rotation and winds) have to be used to predict the observational properties of a bubble. The majority of the theory is based upon the works of Castor et al. (1975), Weaver et al. (1977) & Weaver et al. (1978). These papers do well in explaining the basic characteristics of HII regions and, to first order, the emission line spectrum provided by massive stellar winds (Hensler 2008).

Weaver et al. (1977) follows the 1D-fluid approximation of a wind discussed in section 6.1. However, they assume that $\dot{M}_W$ and v_∞ are constant throughout the stellar lifetime. Another assumption is the ambient ISM is of uniform atomic density n_0. Finally the star is assumed to be stationary within the ISM. After the ZAMS, over time, a bubble will form with characteristics shown in Figure 6.3. The following

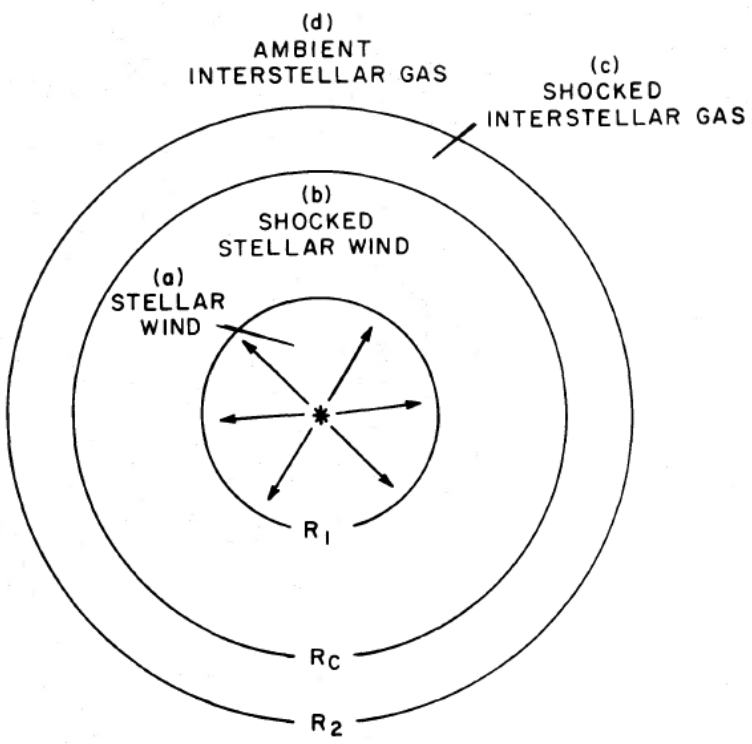

Figure 6.3: Figure 1 from Weaver et al. (1977). Starting from the star going outward, R_1 is the stellar wind and is region (a). Region (b) from R_1 to R_C is shocked stellar wind, consisting of a hot almost isobaric gas (Castor et al. 1975). Region (c), R_c to R_2 is swept interstellar gas shell and final region (d) ambient interstellar medium.

equations will be used to calculate the possible characteristics of the bubbles created by the binary models (Castor et al. 1975, Weaver et al. 1977). The first equation is the mechanical luminosity, which is described as the luminosity generated by the stellar wind interacting with the ISM:

$$L_W = \frac{1}{2}\dot{M}v_\infty^2 \tag{6.29}$$

The total radius of the bubble can be calculated from the density n_0 of the ISM, mechanical luminosity, and the age of the star. This is expressed in the following

Figure 6.4: Rosetta nebula (NGC 2237). The entire nebula is roughly 130 lyrs (light Years) across and 5500 lyrs away with a Mass $\sim 10,000 M_{\odot}$. Image was taken with the Schmidt telescope at the California Institute of Technology's Palomar Observatory on March 29, 1998 & January 18, 1997. Blue (DSS-II): IIaJ emulsion + GG395 Red (DSS-II): IIIaF emulsion + RG610 Image credit: NASA the DSS-II and GSC-II Consortia)

Figure 6.5: False color image of a bow shock from ζ Ophiuchie observed with the Spitzer telescope on 12/18/2012. Observations were in the infrared with false coloring: blue for 3.6 and 4.5 μm, 8.0 μm for green, and red 24 μm. The star is $\sim 20 M_{\odot}$ and is ~ 458 lyrs away. Image credit: NASA/JPL-Caltech

way:

$$R_2(t) = 27 n_0^{-1/5} L_{36}^{1/5} t_6^{3/5} \text{pc} \tag{6.30}$$

Where $L_{36} = L_W/(10^{36} \text{ergs s}^{-1})$ and $t_6 = t/(10^6 \text{ yrs})$. The unit pc stands for parsec which is ~ 3.26 lys. The final equation is the expansion rate of the bubble into the ISM.

$$v_2(t) = 16 n_0^{-1/5} L_{36}^{1/5} t_6^{-2/5} \text{km s}^{-1} \tag{6.31}$$

Weaver et al. (1977) used Equations 6.29-6.31 to study ζ Pup, a Galactic O4 star with a mass $\approx 53.1 M_{\odot}$, to predict the Gum nebula's v_2 and R_2 (Bouret et al. 2012). According to observations, ζ Pup had an $\dot{M} \approx 7 \times 10^{-6} M_{\odot}$ yr^{-1} and $v_{\infty} \approx 2700$ km s^{-1}. The ISM density near ζ Pup is ≈ 0.25 cm^{-3}, which gave $R_2 = 126$ pc and

$v_2 = 25$ km s^{-1}. This agrees with the observed characteristics of the nebula.

To make a prediction of observables, I use PIMMS - Portable, Interactive Multi-Mission Simulator, provided by NASA. PIMMS will be discussed more in Chapter 8, however to use PIMMS five observational properties of the bubble are required as inputs. The temperature and luminosity from region (b) must be known. In addition, the flux, calculated from the luminosity and the distance to the system, the column density as seen from the observer are needed for inputs. The column density is the surface density of hydrogen between the source and the observer. The value for this is discussed in Chapter 8. The flux is determined in the following way:

$$F = \frac{L_b}{4\pi r^2} \tag{6.32}$$

Where L_b is the luminosity in region (b) from Weaver et al. (1977):

$$L_b = 3.8 \times 10^{33} n_0^{18/35} (\dot{M}_6 v_{2000})^{37/35} t_6^{16/35} \text{ergs s}^{-1} \tag{6.33}$$

Where $\dot{M}_6 = \dot{M}_W/(10^{-6}\text{M}_\odot \text{ yr}^{-1})$ and $v_{2000} = v_\infty/(2000 \text{ km s}^{-1})$. The peak temperature of region (b) is required to calculate the spectral energy distribution to be used by PIMMS. This is done in the following way:

$$E_{peak} = k_b T_b s \tag{6.34}$$

Where k_b is the Boltzmann constant, $k_b = 8.617 \times 10^{-5}$ eV K^{-1}. T_b is shown in Weaver

et al. (1977) as:

$$T_b = 1.6 \times 10^6 n_0^{2/35} (\dot{M}_6 v_{2000})^{8/35} t_6^{-6/35} \text{ K} \tag{6.35}$$

In the models shown in chapter 7 this gives a peak value in the soft X-rays ~ 0.2 keV. Finally, the number density of region (b) is required to determine the ease of observing the bubble. The higher the number density the easier it will be to observe. The number density in region (b) is as follows:

$$n_b = 0.01 n_0^{19/35} (\dot{M}_6 v_{2000})^{6/35} t_6^{-22/35} \text{cm}^{-3} \tag{6.36}$$

Using Equations 6.30-6.36, PIMMS, and an assumed distance, I will be able to predict a possible count-rate of a modeled bubble. The count-rate will be determined for two X-ray telescopes Chandra and X-ray Multi-Mirror Mission-Newton (XMM). This will be the connection between my models and future observations.

Chapter 7

Computation Results

All binary models used Higgins (private communication) inlists unless otherwise specified (for instance the Brott et al. 2011 inlists). For sections 7.1-7.3 the primary star mass was set to $M_1 = 35\mathrm{M}_\odot$ and the secondary mass was set to $M_2 = 25\mathrm{M}_\odot$, which gives a mass ratio $q_1 \approx 0.714$. A q_1 value of ~ 0.7 is used as a constraint for setting the initial masses of the primary star star and secondary. This mass ratio is used throughout the literature. The period of ~ 1.5 to ~ 5 days is commonly used to model close binary systems, therefore the initial period is set to 4 days. This gives a separation distance $a \approx 41.5\mathrm{R}_\odot$. The eccentricity is set to 0 and is constant throughout the evolution. For simplicity, both the primary star and secondary's initial surface rotation are equivalent. The tidal enhancement factor was set to the default of $B_W = 10^4$. In all sections models were run until either no acceptable solution was found (small time steps), or terminated when $\frac{v}{v_{crit}} = 1$. This happens near the onset of RLOF when the primary star's envelope expands past the L1 point near core hydrogen exhaustion (TAMS)[1] As noted earlier, evolutionary data past RLOF are not plotted or discussed. Tables 7.1 and 7.2 give the initial conditions and labelling system for the following sections. The primary star is referred to as the primary and the secondary star is referred to as the secondary.

[1] Hydrogen exhaustion is defined when there is $\sim 1\%$ hydrogen in its core. This value for hydrogen exhaustion is used throughout the literature.

Table 7.1: Initial conditions for each model set up per section.

Section	$M_{Primary}$	$M_{secondary}$	$< q >$	a	Inlists Used
-	$M_\odot$	$M_\odot$	-	$R_\odot$	-
7.1-7.3	35	25	0.714	41.5	(Higgins & Vink 2019)
7.4	35	25	0.714	41.5	(Higgins & Vink 2019) (Brott et al. 2011)
7.5	25-60	20-40	0.68 ± 0.07	37.7-49.2	(Higgins & Vink 2019) (Brott et al. 2011)

Table 7.2: Model parameter values discussed in the following sections with corresponding labels.

Model Label	α_{ov}	f_{vink}	v_{rot}	W_{tides}	W_{trans}
			(km s^{-1})		
v1	0.1	1.0	100	ON	ON
v2	0.1	1.0	200	ON	ON
v3	0.1	1.0	300	ON	ON
v4	0.1	1.0	400	ON	ON
v5	0.1	1.0	500	ON	ON
v1off	0.1	1.0	100	OFF	OFF
v2off	0.1	1.0	200	OFF	OFF
v3off	0.1	1.0	300	OFF	OFF
v4off	0.1	1.0	400	OFF	OFF
v5off	0.1	1.0	500	OFF	OFF
v1t	0.1	1.0	100	ON	OFF
v3t	0.1	1.0	300	ON	OFF
a1	0.1	1.0	100	ON	ON
a3	0.3	1.0	100	ON	ON
a5	0.5	1.0	100	ON	ON
vf05	0.1	0.5	100	ON	ON
vf1	0.1	1.0	100	ON	ON
vf15	0.1	1.5	100	ON	ON
vf3	0.1	3.0	100	ON	ON

7.1 Rotational Velocity

Varying the rotational velocity is studied extensively because the rest of the models e.g., vf05-vf3, show many similarities to v1-v5. Three different types of systems

are presented to emphasize different physical processes. The first set of figures include tidally enhanced winds from Tout & Eggleton (1988) and wind mass transfer from Bondi & Hoyle (1944) (models v1-v5). A series of models were made ignoring both these mechanisms (v1off-v5off) and another set just ignoring wind mass transfer (v1toff and v3toff).

7.1.1 Pre Bi-stability Jump

The bi-stability jump for v1-v5 happens at $t_{system} \approx 6.4$ Myr. After the jump, until the termination of the models, the system is extremely dynamic. The physical characteristics of the binary model change on short timescales in comparison to the nuclear timescale. The primary and secondary reach the jump temperature (T_{jump}) at approximately the same time for v1 and v2, however this is not true for v3-v5. The bi-stability jump for the primary is smaller than the jump of the secondary for v1 and v2, thus causing a wind mass transfer event (the spike in Figure 7.12).

The location of (1) and (3) in Figure 7.1 shows the start of the model and a hook like feature for both the primary and secondary. The hook itself is the result of the high initial rotation velocity. The v5 model provides the most prominent form of this feature for both stars.

The equatorial radii of both stars are larger than the polar radii due to the high rotational velocity. For example, $R_{eq}/R_{polar} = 1.14$ for the primary for v5. The deviation from radial symmetry causes a decrease in T_{eff}. As the stars evolve the

rotational velocity decreases due to tidal torques, spin-orbit coupling, and Ω diffusion due to instabilities.

In the beginning of this evolutionary hook g_{eff} is small because g_{cent} is large due to the high v_{init} (note that $\vec{g}_{eff} = \vec{g}_{grav} - \vec{g}_{cent} - \vec{g}_{rad}$). Proceeding to the top of the hook, g_{eff} increases since the value of g_{cent} has fallen due the decrease of v_{rot} (see Chapter 4). The luminosity is lower at the beginning of the hook than at the top because g_{eff} decreases and so the pressure gradient decreases throughout the star (Based on Equation 4.6). Therefore the luminosity generation in the core is lower. Then g_{eff} increases and the pressure gradient increases, so the central core density rises, which leads to an increase in energy output in the core. The star's rotation slows, R_{eq} contracts, and the luminosity increases which also leads to an increase in the surface temperature. This creates the hook feature for all models of the primary and secondary.

For a star with the mass of the primary, T_{eff} would continually decrease while L would remain constant during the MS stage (see Figure 3.1). However as shown in Figures 7.1 and 7.2 the luminosity of the primary decreases dramatically during the MS. Starting from the location of (1) on the evolutionary tracks and going towards (2) in Figure 7.1, the primary's T_{eff} decreases by ~ 0.225 dex and $\log L$ by ~ 0.5 dex in ~ 7.6 Myrs. The significant decrease of $\log L$ in this time frame is fascinating. The primary is losing a significant portion of its envelope due to high wind mass loss and g_{eff} is decreasing rapidly. The Mass-Luminosity vector points downwards starting

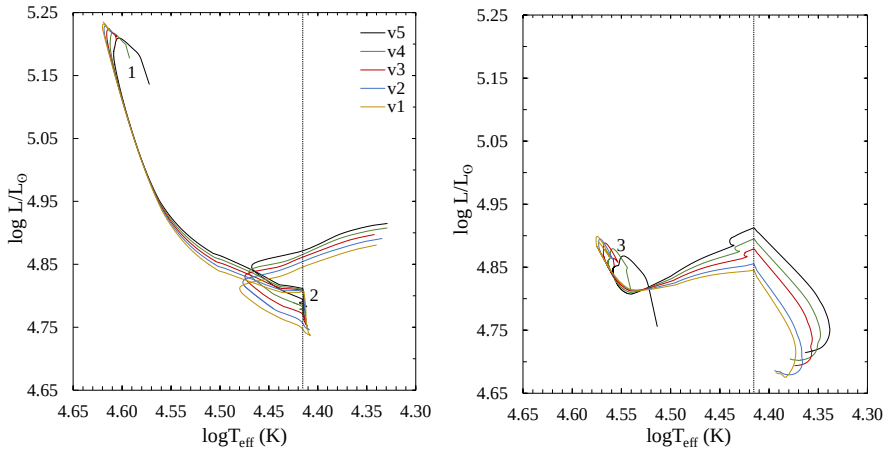

Figure 7.1: Evolutionary tracks on the HR-diagram for the primary (left) and secondary (right). Five models are presented with various rotational Velocity. (1) and (3) give the location of the beginning of model in the HR-Diagram. (2) shows the location of hydrogen exhaustion for the primary. The vertical dashed line shows the approximate bi-stability jump temperatures for both the primary and secondary.

from (I) and going down towards (II) in Figure 7.2 because $\dot{M}_W$ is so high (see Figure 2.4 for how $\dot{M}_W$ effects the "ML-vector"). Since the mass of the star decreases the luminosity will decrease (see Equation 2.15).

Wind enhancement due to rotation and tides, discussed in Chapters 5 and 6, contributes to the high $\dot{M}_W$ for both stars. The example from section 6.3.2 shows the contribution to $\dot{M}_W$ from tides was $\sim 157\dot{M}_W(0)$, which is a significant increase. Enhanced winds due to rotation contribute $\sim 1.7\dot{M}_W(0)$ for the primary in model v5, therefore tides and winds will amplify each other. The contribution of tidally enhanced winds is shown by the comparison of $\dot{M}_W$ for v1-v5 and v1off-v5off models (see Figure 7.7). After $\sim$ 2 Myr the wind mass loss of the primary decreases by a factor of 30. If the separation distance increases (which it does, see Figure 7.3) then wind enhanced mass loss due to tides will decrease. The primary's rotational speed,

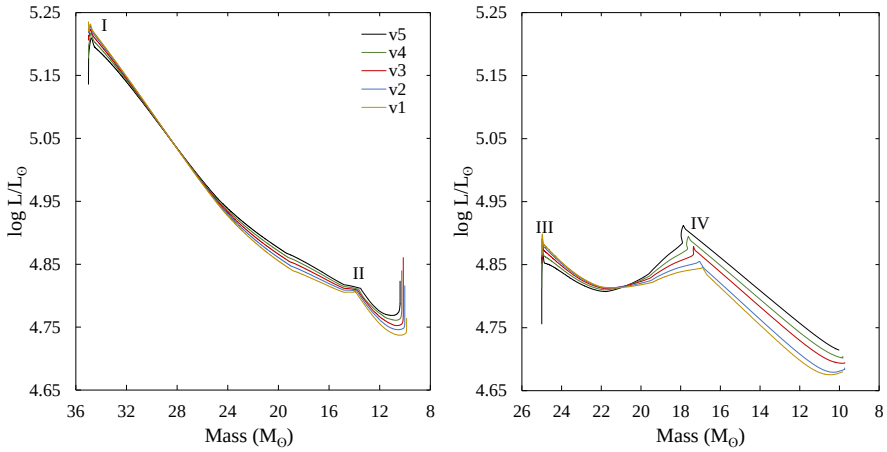

Figure 7.2: Mass-Luminosity plane for the primary (left) and secondary (right). (I) and (III) show the start of the models. (II) and (IV) are the locations when the primary reaches its first bi-stability jump and secondary reaches its bi-stability jump.

shown in Figure 7.12, decreases quickly before ~ 2 Myrs, due to tides and mass loss, and therefore enhanced winds due to rotation will decrease. The total mass lost from the primary is tremendous. At the termination of models v1-v5 the final mass of the primary is $\approx 10 M_{\odot}$ as shown in Figure 7.2.

The secondary is a more interesting case than the primary. Instead of the luminosity decreasing continually throughout it's evolution, the evolutionary track performs a bigger loop, L increases afterwards, and then decreases dramatically below $\log T_{eff} \approx 4.0$ as shown in Figure 7.1. The decrease after the loop and after the black-dash line is consistent with the argument of high mass loss. The secondary's "ML vector" points down giving the steep slope after the loop. Then, later on in its lifetime, it decreases at the same slope as the primary. The change in $\log T_{eff}$ past the black-dash line in Figure 7.1 is caused by the secondary's radius slightly decreasing, therefore increasing the surface temperature. The reason for the sudden drop in $\log L$

is due to the bi-stability jump of the secondary, discussed in the next section.

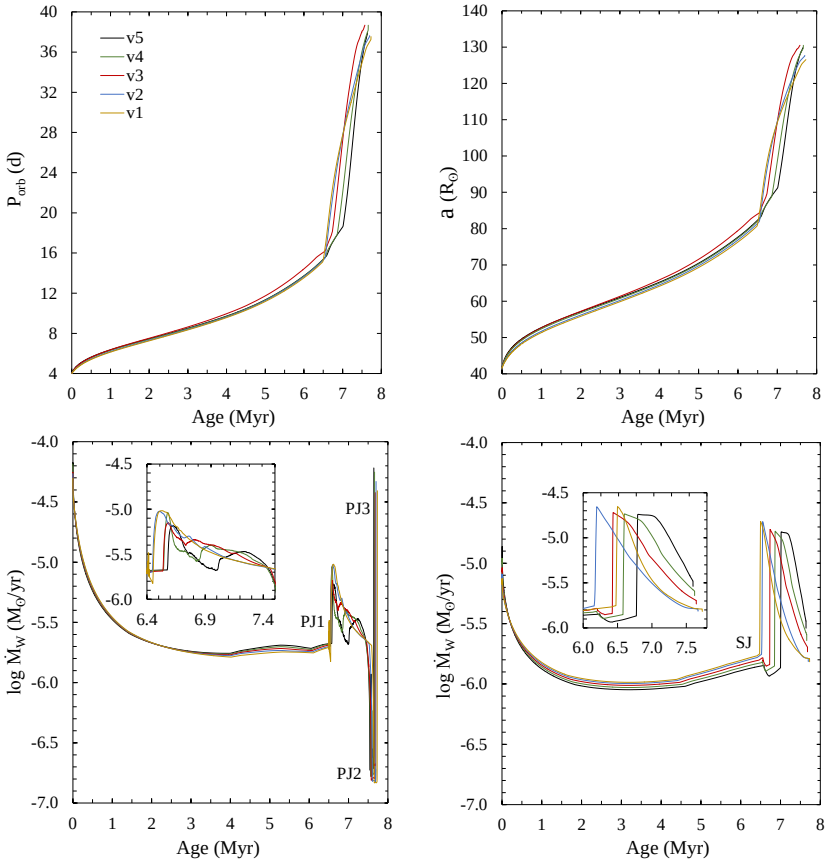

Figure 7.3: Period & separation vs age for various v_{init} (top). Mass loss rate vs Age for the primary (bottom left) and secondary (bottom right) for various v_{init} (bottom). PJ1 PJ2 and PJ3 show the location of the primary's first, second, and third bi-stability jump. SJ shows the location of the start of the secondary's bi-stability jump. The insets are meant to emphasize the large increase of $\dot{M}_W$ due to the jumps.

7.1.2 Bi-Stability Jump

The bi-stability jump of both stars causes the system to be extremely dynamic. During this period the hows an evolutionary loop caused by it reaching the TAMS. The

secondary performs an elongated evolutionary hook in the HR-Diagram due to it reaching its T_{Jump} (black-dash line in 7.1). $\dot{a}$ and $\dot{P}_{orb}$ increase during this time period from $t \sim 6.4$ Myr onward. The location of the dash black and green lines, shown in Figure 7.4, indicate that $\dot{P}_{orb}$ increases due to the bi-stability jumps. v_{rot} increases for v3-v5 near this location and then decreases immediately afterwards. There is a spike in the ^{14}N surface abundance due to wind mass transfer for both the primary and secondary.

The primary's evolutionary track performs a loop beginning at (2) in Figure 7.1. At the beginning of the loop the luminosity decreases, while the temperature remains the same. Then the temperature increases quickly and the luminosity increases slightly. The primary's radius begins to increase quickly at $\log T_{eff} \sim 4.45$ and therefore $\log T_{eff}$ decreases to ~ 4.35 which is the end of the model. The loop exists because the primary has reached hydrogen core exhaustion, has hydrogen shell burning, and is slowly initiating core helium burning.

For a typical model at TAMS the envelope of the star is expanding, which decreases $\log T_{eff}$, while the core temperature and density continually increase. When the core density and temperature are high enough to initiate helium core burning the core's energy generation will increase. During the onset of helium burning the radius will increase dramatically so $\log T_{eff}$ decreases. This evolutionary feature is shown in Figure 3.1. The primary follows the same evolutionary features, but the change in $\log L$ and $\log T_{eff}$ are more dramatic, leading to a loop like feature. This loop feature

can be attributed to the high $\dot{M}_W$ (see figure 7.7 for the magnitude difference) because, before the onset of this evolutionary phase, the primary reaches T_{jump} (dash dotted line in Figure 7.1).

As indicated in Figure 7.1, the primary actually evolves to T_{Jump} three times, twice from the hot side of the jump and once from the cold side. Note that T_{Jump} is not always constant throughout the evolution of the primary and secondary, it lies within the range of $4.414 \leq \log T_{eff} \leq 4.42$. First the temperature and luminosity continually decrease and the mass loss rate remains the same until the primary crosses T_{Jump} the first time (location II in Figure 7.2). Then the core reaches hydrogen exhaustion (2 in Figure 7.1) and the luminosity generation by hydrogen burning decreases. Then hydrogen shell burning begins, the luminosity generation increases slightly and the star's radius does not change. Therefore $\log T_{eff}$ and $\log L$ increase and the primary approaches $\log T_{Jump}$ again, but from a lower to higher temperature. Finally, the star expands rapidly because of the hydrogen shell burning and the core starts helium burning. Therefore $\log T_{eff}$ decrease and the primary reaches the jump again near the termination of the model. However each time the primary reaches the bi-stability jump it has different physical characteristics e.g. the $\log L$ and the mass are different. Therefore the magnitude of the jump is different, since the $\dot{M}_W$ is dependent on mass and luminosity.

Explaining the characteristics of $\dot{M}_W$ for the primary near the bi-stability jumps is straight forward. The star reaches the bi-stability jump (PJ1 shown in Figure 7.3)

from the hot side, therefore there is an increase in $\dot{M}_W$. Next the star goes through the evolutionary path describe above, therefore the star approaches the jump from the cool side of T_{Jump} (PJ2), thus leading to a decrease in $\dot{M}_W$. Then, very rapidly, the star approaches again from the hot side of the jump (PJ3), which causes yet another jump in $\dot{M}_W$.

It takes the primary $\sim 7 \times 10^4$ yrs to perform this loop. Therefore any physical changes because of this loop, for instance the binary separation, happens on short timescales in comparison to the system age. This leads to the discontinuity-like feature near the end of the models in Figure 7.3. After PJ1 the primary evolves to T_{Jump} again and therefore reaches PJ2 where $\log \dot{M}_W$ value is ~ -5.5. Finally, in $\sim 3 \times 10^3$ yrs the primary evolves past T_{Jump} for the third time (PJ3), and now $\log \dot{M}_W$ is ~ -4.4.

The dramatic decrease of $\dot{M}_W$ at PJ2 has to do with FeIII ionizing to FeIV. As described in chapter 6, FeIV does not have many lines and is not a significant contributor to $\dot{M}_W$. Only when the majority of Iron is in FeIV state, when T_{eff} is greater then T_{Jump}, does FeIV significantly contribute to $\dot{M}_W$. When FeIII ionizes to FeIV at T_{Jump}, only a small fraction of iron is in the FeIV state at this temperature, leading to a lower $\dot{M}_W$. The sudden decrease in $\dot{M}_W$ is due to the quick ionization of FeIII to FeIV throughout the wind.

According to Keszthelyi (private communication), the bi-stability jump has not been constrained by observations for the evolutionary transition of TAMS to helium

core burning. Keszthelyi et al. (2017) provide a brief description of the uncertainty of modeling the bi-stability jump during TAMS and near core helium burning. As described above, the stellar parameters of the primary are changing drastically on short timescales. Therefore, from this point on, I will only focus on the primary's bi-stability jump before TAMS. Therefore the labeling of primary jump 1 (PJ1) will simply become PJ now that PJ2 and PJ3 will no longer be included in the discussion.

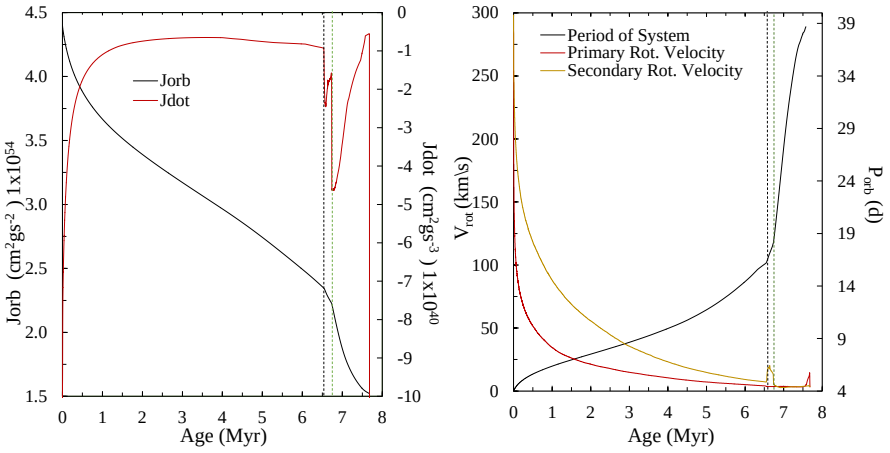

Figure 7.4: J_{orb} and $\dot{J}$ plotted vs. Age (left) and primary rotation, secondary rotation, and period vs Age (right) for the v3 model. The black-dash lines indicates the primary's first jump. The green dash-lines shows the location of the secondary's jump.

For $\log T$ between 4.46 and 4.51 the primary is less massive then the secondary. Since secondary's mass is higher and $\dot{M}_W$ is lower than the primary, the seconary's luminosity increases. Then the secondary reaches the bi-stability jump and its luminosity decreases significantly (black dash-line shown in Figure 7.1). When the secondary reaches the jump (see Figure 7.3) the mass loss rate is so high that the

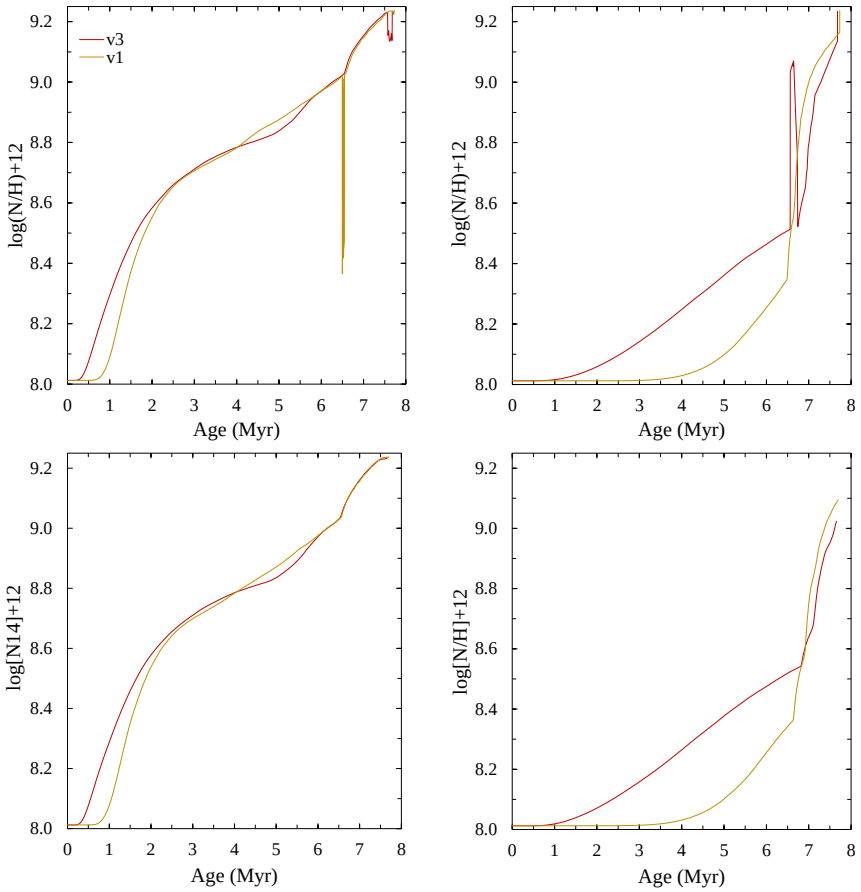

Figure 7.5: ^{14}N surface abundance vs. Age for the primary (left) and secondary (right) for v1 and v3. The top two graphs include wind mass-transfer and the bottom two graphs do not.

$\log L$ decreases dramatically, as seen in Figure 7.2. Near the termination of the models, the relative amount of mass loss for both the primary and secondary are the same, as shown by the slope of the ML-plane. The "bump" in the HR-diagram for v3-v5 at $\log T \approx 4.4 - 4.45$ in the secondary's plot is due to the decrease in $\dot{M}_W$ of the secondary and bi-stability jump of the primary (See Figure 7.6).

The ratio of $\dot{M}_W$ below the jump temperature to above the jump temperature for the primary is $\dot{M}_{W,cool}/\dot{M}_{W,hot} \sim 3.46$. For the secondary the ratio of $\dot{M}_W$ is

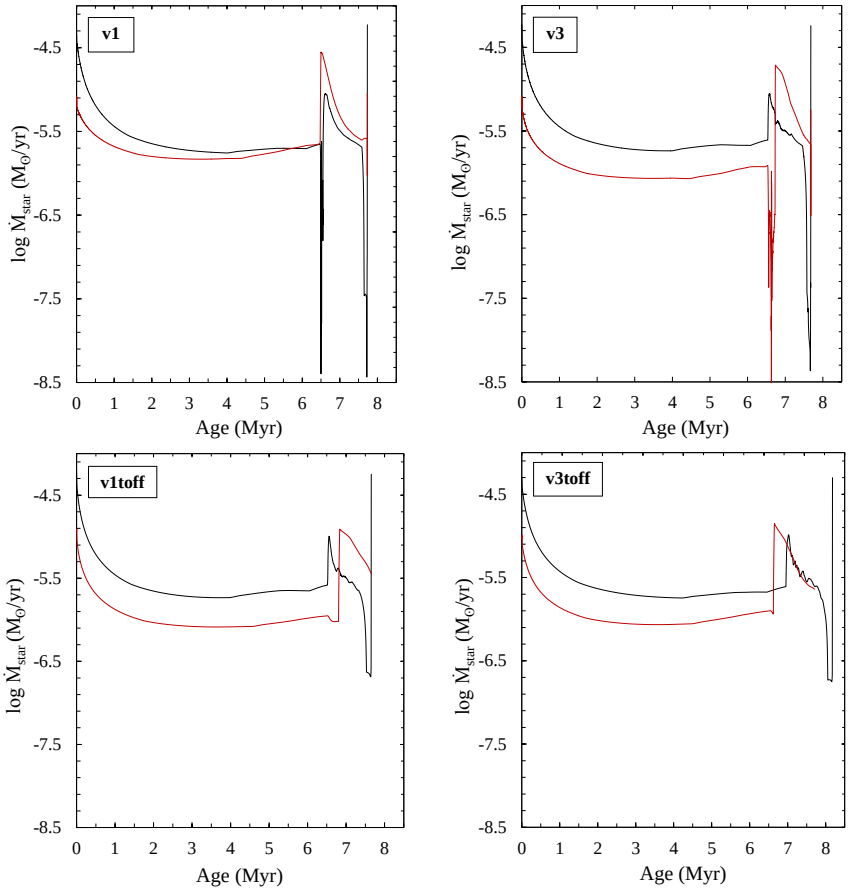

Figure 7.6: $\dot{M}_\star$ vs Age for the primary (left) and secondary (right) for wind mass-transfer included in the models (top) and not included (bottom).

$\dot{M}_{W,cool}/\dot{M}_{W,hot} \sim 13.26$. There is a difference because the secondary is more massive and has a higher luminosity at its bi-stability jump, its ratio of $\dot{M}_{W,cool}/\dot{M}_{W,hot}$ will be larger than the primary. Note the oscillatory behavior of $\dot{M}_W$ near PJ is due to the primary maintaining the same temperature (near $\log T_{Jump}$), but both the luminosity and mass are decreasing during this period (see Figure 7.1).

In Figures 7.3 and 7.4 there is a clear indication of the bi-stability jumps of the secondary and primary. For Figure 7.3 the separation and period evolve at the same

rate up to PJ and SJ. Afterward the slope increases. The difference bewtween v1-v2 and v3-v5 in Figure 7.4 is due to wind mass transfer by the bi-stability jumps.

As shown in Figure 7.12 there is a sudden increase in rotational velocity for v3-v5 during this time. Comparing the data for rotation velocity for v3toff and v3 during this time shows that a jump in rotational velocity does not occur. Wind mass transfer, due to the bi-stability jump of the primary, is spinning up the secondary's surface for v3-v5. For v1 and v2 PJ and SJ line up such that the secondary does not gain any matter (see Figure 7.6) and therefore there is not a dramatic increase in v_{rot} for either star. This is the reason for the different slopes when comparing v1 and v2 to v3-v5 for a and P_{orb} as shown in Figure 7.3. a and the period are changing because of how large $\dot{M}_W$ is for both the primary and secondary. $\dot{J}_{ml}$ is always negative and $\dot{J}_{ls}$ is general positive (occasionally $\dot{J}_{ls}$ is negative, but this does not happen frequently). As the system evolves, $\dot{J}_{ml}$ is ~ 10 times larger then $\dot{J}_{ls}$, therefore a and P_{orb} increase due to the loss of orbital angular momentum. Finally the black and green dashed lines shown in Figure 7.4 indicates the effects the bi-stability jumps have on J_{orb}, $\dot{J}_{orb}$, and period of the primary and secondary. The bi-stability jump, caused by the recombination of FeIV to FeIII, affects the binary characteristics and therefore can not be ignored.

7.1.3 Tidally Enhanced Winds & Wind Mass Transfer

The tidal enhancement factor, as described above, has a large impact on the models. For v1off-v5off the lifetime of the system is shorter than v1-v5, where the model terminates at $t \approx 2.5$ Myr (See Figure 7.7). The primary and secondary evolutionary tracks exhibit typical characteristics of an O and B star (Shown in Figure 7.8). The change in the mass from the beginning of the model to end is only a few solar masses, which allows the primary to burn through its fuel faster. There is a deviation in the beginning of the models, but this is due to a high v_{init} and the contribution of enhanced winds due to rotation. Note that the primary and secondary of the v1off-v5off models do not experience the bi-stability jump (shown in Figure 7.7). The mass loss rate are more appropriate for stars of their respective masses. The comparison emphasizes the strength that tidally enhanced winds have on the model binary systems. Due to this large impact on the binary system, the tidal enhancement parameter B_W, was investigated for v3.

Wind mass transfer using the Bondi & Hoyle (1944) method is not shown in the $\dot{M}_W$ plots, however it is shown in the $\dot{M}_\star$ vs. age plots. $\dot{M}_\star$ is the total mass loss rate ($\dot{M}_{RLOF}$, wind mass transfer, and $\dot{M}_W$) of a model star. Shown in Figure 7.6, there is a clear indication of wind mass transfer near the location of PJ and SJ. The spike in Figure 7.12 is due to the primary accreting matter from the secondary. The secondary's surface has less ^{14}N then the primary's surface. Therefore the primary's ^{14}N surface abundance will decrease during the wind mass transfer. While for higher

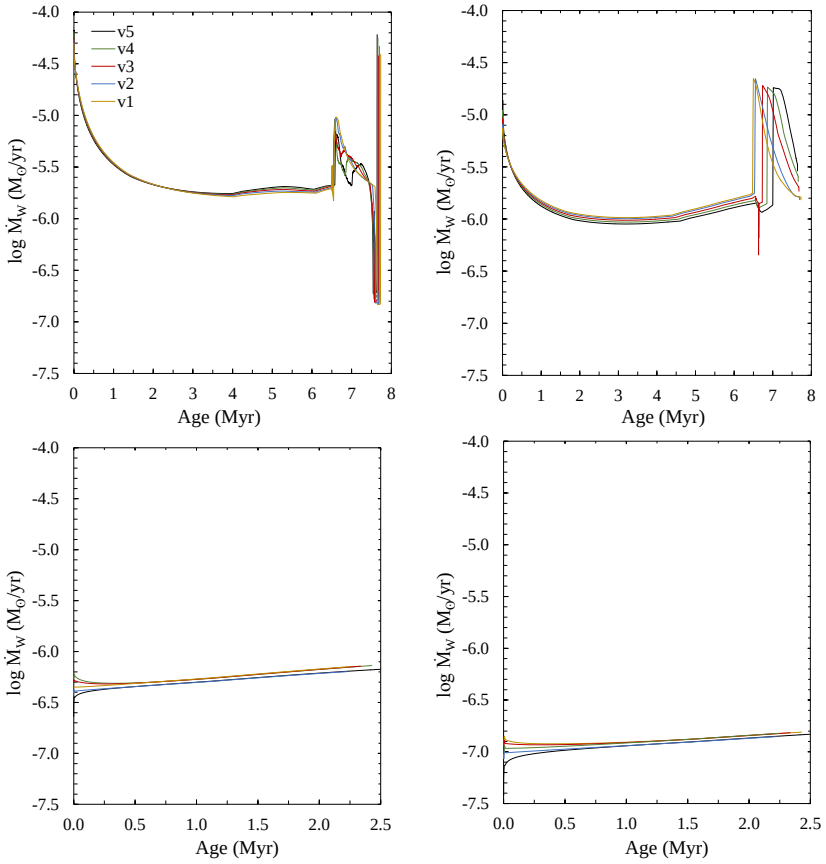

Figure 7.7: $\dot{M}_W$ vs age for the primary (left) and secondary (right). The top two graphs include tidally enhanced winds and wind mass-transfer (models v1-v5). The bottom graphs do not include these effects (v1off-v5off)

velocity's models v3-v5 PJ is shifted from SJ, then accretion will happen onto the secondary's surface. Therefore the secondary will have an increase in surface ^{14}N as shown in Figure 7.12 near 6.5 Myr.

There is a benefit of plotting the primary and secondary on the same graph (Figure 7.6). For example, for v1 the primary and secondary $\dot{M}_\star$ are almost identical after 5 Myrs, while this is not true for v1toff. What is even more interesting is the PJ happens at the same time as SJ as discussed above. The $\dot{M}_W$ for SJ is larger than

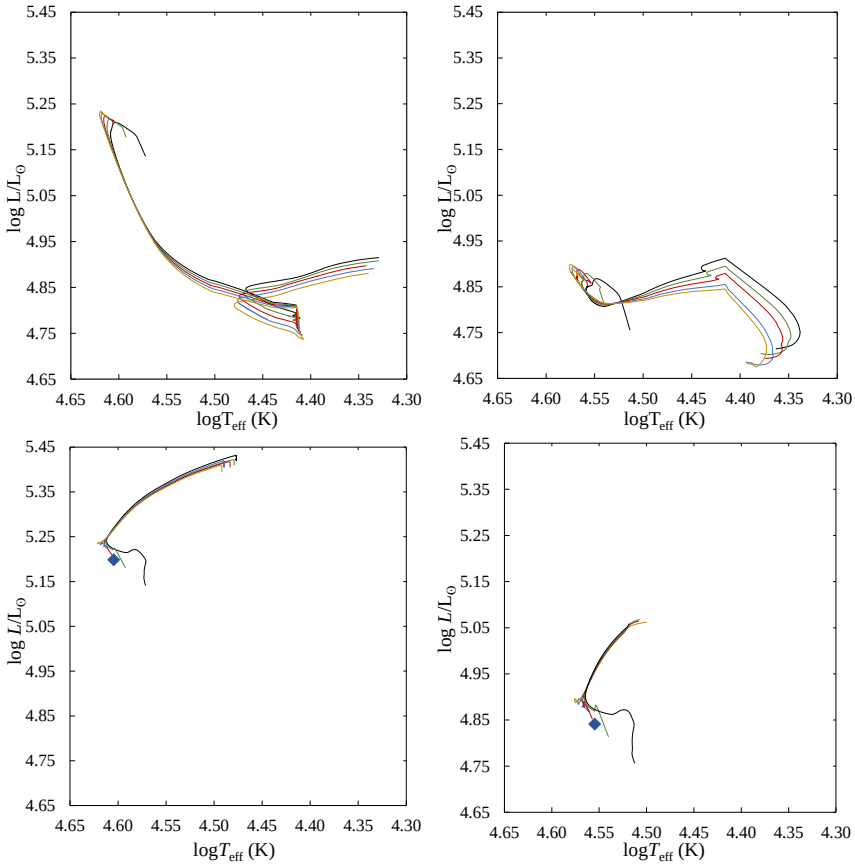

Figure 7.8: HR-diagram for the primary (left) and secondary (right) for models using tidally enhanced winds and wind mass-transfer (top). The bottom graphs do not include these effects. The blue diamond indicates the location of the start of the models.

for PJ, so $\dot{M}_\star$ of the primary evolves differently. However this is not the case for v3 and v3toff. This is due to tidally enhanced winds, which will drastically change $\dot{M}_\star$.

The orbital period for v1off-v5off only differ from their starting values (4 days) by about a day. $\dot{M}_W$ of the primary and secondary are low enough that throughout the evolution $|\dot{J}_{ml}| \leq |\dot{J}_{ls}|$ and therefore $\dot{J}_{orb}$ is positive and the orbital period will decrease. Overall $\dot{J}_{ml}$ for v1off-v5off is an order of magnitude lower than $\dot{J}_{ml}$ for

v1-v5.

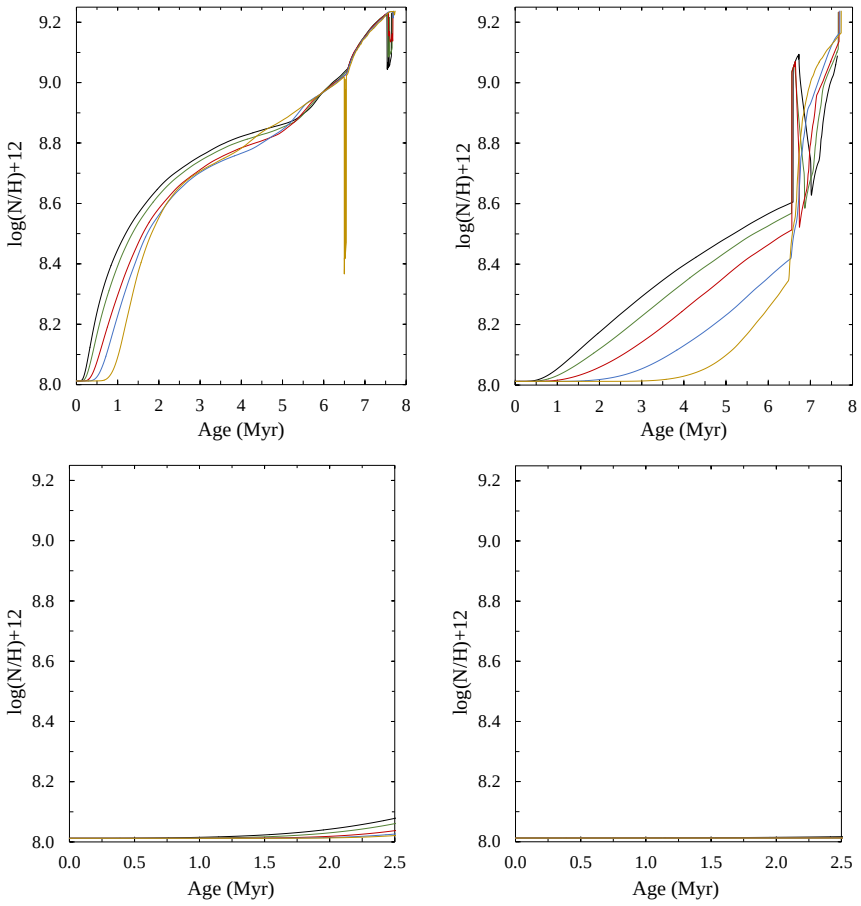

Figure 7.9: ^{14}N surface abundance vs. Age for the primary (left) and secondary (right). The top graphs include tidally enhanced winds and wind mass transfer (v1-v5). The bottom do not include them (v1off-v5off)

7.1.4 Surface Abundance & Rotation

^{14}N surface abundances for massive rotating binary stars are of great interest. The observed ^{14}N surface appears to be higher for slow rotating B stars, and lower for fast rotating O stars. The connection between these two cases is the focus of Maeder

& Meynet (2012), Higgins & Vink (2019), Brott et al. (2011), and Ekström et al. (2012). The relationship between the ^{14}N surface abundances and surface rotation is believed to be due to rotational mixing inside stars that were initially fast rotators. This was briefly discussed in Chapter 4. In binary systems, mass transfer, mass loss, tidal forces and mixing due to tidal dissipation can also lead to this connection (see Langer 1998 for the theory of mass transfer and ^{14}N surface abundances).

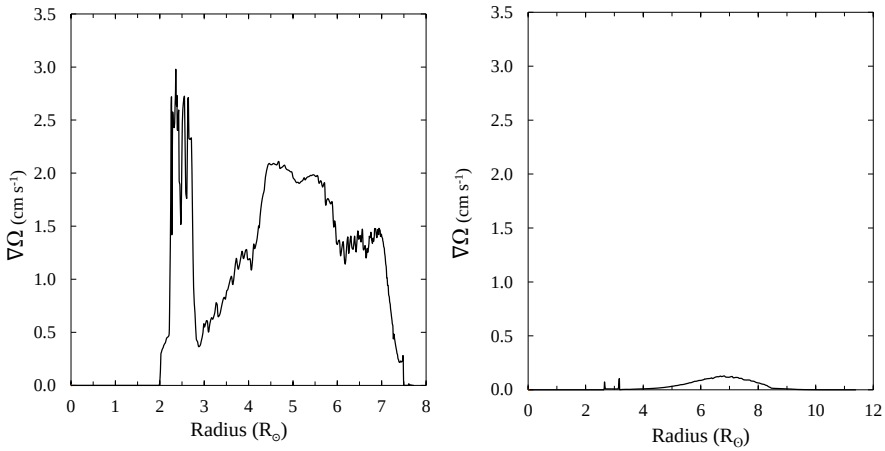

Figure 7.10: Shear vs. Radius for the primary of v3 at $t \sim 2.2$ Myr (left) and v3off at $t \sim 2.5$ Myr (right)

For v5off the ^{14}N abundance changes by just under 0.2 dex for the primary and there is a minute change in the secondary. The surface rotational velocity decreases but stops decreasing near $v_{rot} \sim 100$ km s^{-1} for both the primary and secondary for v1off-v5off. There are three reasons for the low ^{14}N surface abundance for the v1off-v5off models compared to v1-v5. First, as shown in Figure 7.10, the shear in the envelope is small for v3off in comparison to v3. This implies v3off has nearly

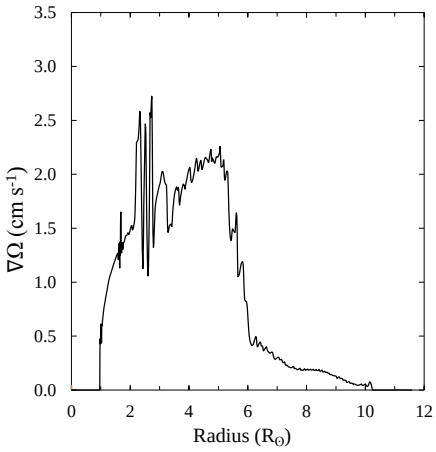

Figure 7.11: Shear vs. Radius for the primary of of v3 at $t \sim 7.62$ Myr.

uniform rotation throughout its interior. While, clearly shown in Figure 7.11, v3 has differential rotation in the envelope. Note that the convective core for v3 for the top two panels are at $R \sim 2\mathrm{R}_{\odot}$ since the shear is ~ 0. This is because convection enforces solid body rotation in the core of massive stars. The strength of chemical mixing is dependent on turbulence and horizontal differential rotation. Therefore the surface and envelope of v3 will be more ^{14}N rich than v3off. Second, the $\dot{M}_W$ for v1-v5 is so high that it causes "stripping" of the envelope revealing the nitrogen-rich interior.

The change in ^{14}N surface abundance for v3 is 1.2 dex for both stars as shown in Figure 7.12. Thus the dramatic increase of ^{14}N is due to the strength of $\dot{M}_W$. This envelope is enriched in ^{14}N due to α_{ov} drawing ^{14}N out of the core into the envelope (discussed in Chapter 2). In addition, the rotational induced circulations and instabilities also contribute to the enrichment of ^{14}N in the envelope (see Chapter 4).

For the ^{14}N surface abundance, the primary's evolutionary pattern closely resem-

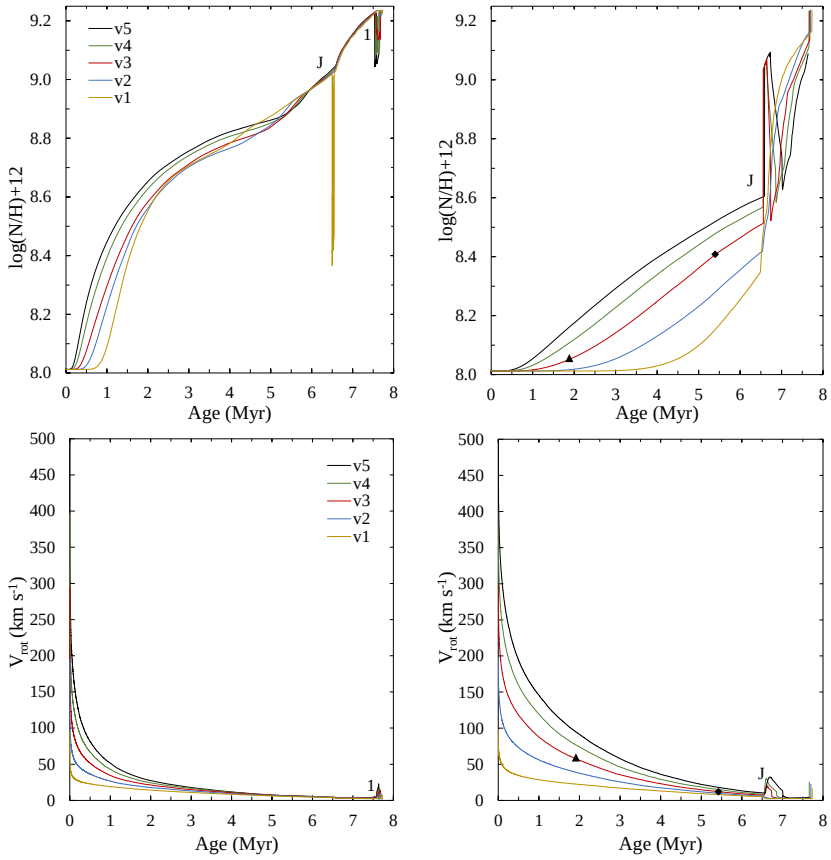

Figure 7.12: Panel of the Surface ^{14}N abundance vs Age (top) and rotational velocity vs age (bottom) for the primary (left) and secondary (right) for v1-v5 models. The Black triangle and diamond are the location when the total mass of the system is $45M_{\odot}$ and $35M_{\odot}$, respectively. The system age at the black triangle is $\sim$ 1.9 Myrs and for the diamond $\sim$ 5.4 Myrs. The letter J is the location of the first bi-stability jump of the primary and the bi-stability jump of the secondary. The location of 1 in the primary's graph is the location of the two other jumps.

bles Figure 1 in Higgins & Vink (2019). However the difference is $\approx$ 0.5 dex which could be attributed to a difference in $\dot{M}_W$ and initial mass. The secondary's ^{14}N abundance and Ω evolution are rather interesting before the onset of the bi-stability jump. Shown in Figure 7.12 are deviations between v1-v5 which develop after $\sim$1 Myr. There are also small deviations from v1-v5 that can be seen in the HR-Diagram. The

specific angular momentum[2] of matter that is lost from the surface causes v_{rot} to decreases. Since $\dot{M}_W$ for the primary is nearly 10 times greater than the secondary in the beginning, the primary's surface rotation rate will decay more quickly. Also, $\dot{M}_W$ for the primary is always significantly higher than the secondary, also leading to greater decrease in v_{rot} than the secondary.

When the system mass is $\sim 45 M_\odot$ the ratio of v_{rot} the primary to the secondary's is ~ 2.6. This is shown by the triangle in Figure 7.12. At this time, the ^{14}N surface mass fraction of the primary is ~ 3.2 times greater than the secondary's as shown in Figure 7.12. Therefore, at this evolutionary period the primary is rotating slower but is more nitrogen-rich than the secondary. This evolutionary period shows, in these models, that a slower rotating nitrogen-rich massive star exists because of high wind mass loss due to binarity. So the reason for slow rotating nitrogen-rich B stars observed in the Large Magellanic Cloud (see Figure 1 in Hunter et al. 2008) may be enhanced winds in binary systems.

When the mass of the system is $\sim 35 M_\odot$ the ratio of the surface rotation of the secondary over the primary is ~ 2. The ratio of the primary over the secondary's ^{14}N surface mass fraction ~ 2.9. However at this point both the secondary and primary are slow rotators, where the primary's v_{rot} is ~ 6.34 km s^{-1} and secondary's v_{rot} is ~ 12.9 km s^{-1}. At the termination of the models both the primary and secondary are slow rotators and the ratio of their surface ^{14}N is ~ 1. The secondary's high mass

[2]specific angular momentum is angular momentum per unit mass (cm^2 s^{-1})

loss rate due to the bi-stability jump is peeling of the layers of envelope at the end of the models and revealing the ^{14}N rich envelope . This is why the secondary's ^{14}N and surface rotation are similar to the primary's when approaching RLOF.

Note that the binary mass is more useful for observations than the system age. The age of the system is difficult to determine from observations. So, if the separation distance and period can be determined from observations, then, by using the general form of Kepler's 3^{rd} law, the binary mass can be determined.

As described above, the models experience a wind mass transfer event at PJ and SJ. This is shown in Figure 7.12 for the primary and secondary; also the little "bump" in Figure 7.12 for the secondary. After PJ and SJ, the evolution of v_{rot} and ^{14}N surface abundance continue approximately the same evolutionary trend. When MESA accounts for mass lost from the primary it does this by removing the surface cell. Then MESA will accrete the mass lost from the primary onto the secondary, therefore creating a new cell surface on the secondary. The matter of this cell has the specific angular momentum and ^{14}N surface abundance of the primary. Therefore if there is a large difference of ^{14}N surface abundance of the primary compared to the secondary this will cause a spike in the graphs. Then MESA will diffuse the properties of the cell into the interior by e.g., convection and/or ES-circulation. Therefore as the system ages, and if mass transfer stops, the physical quantity's evolution will approximately follow its original path. I would like to note that accreting specific angular momentum is a little different, because the accreted matter gains additional

specific angular momentum by "falling" down the gravitational well of the secondary. This is why the secondary's rotational rate increases rapidly during RLOF.

Varying the velocity between models v1-v5, as shown in the HR-diagram, has little effect until close to the beginning of PJ. The main sequence width is increased slightly around this region. Turning the tidal enhancement factor on and off has drastic effects on the models, as discussed in the next section. One interesting evolutionary feature is the loop in the primary's HR-diagram which results in the multiple bi-stability jumps (PJ,PJ2, and PJ3) in Figure 7.3. The evolution of the surface velocity decreases quickly for the primary and decays slower for the secondary. The orbital parameters e.g., P_{orb}, a, and $\dot{J}_{orb}$ follow the same trend up to the location of the bi-stability jump. This is not surprising, since all quantities depend on the mass loss rate (see Equation 5.16).

7.1.5 Tidal Enhancement Factor B_W

Two papers, Han et al. (1995) and Han (1998), constrained the value of the Tout & Eggleton (1988) B_W parameter from observations (See Equation 6.20). Han et al. (1995) created a grid of models by varying B_W, ranging from $0 - 10^4$, to match observations of Be stars. Han et al. (1995) found a value $B_W = 500$ reproduced the observations. Han (1998) focused on double degenerate binary stars and found $B_W = 10^3$ closely reproduced observations. Frankowski & Tylenda (2001) derived a more complex formula to model tidally enhanced winds. For the Frankowski &

Tylenda (2001) formula, the B_W would be smaller than the values used by Tout & Eggleton (1988), Han (1998), and Han et al. (1995). Note that these values were constrained from observations of lower mass stars $\sim (1 - 1.5 M_{\odot})$.

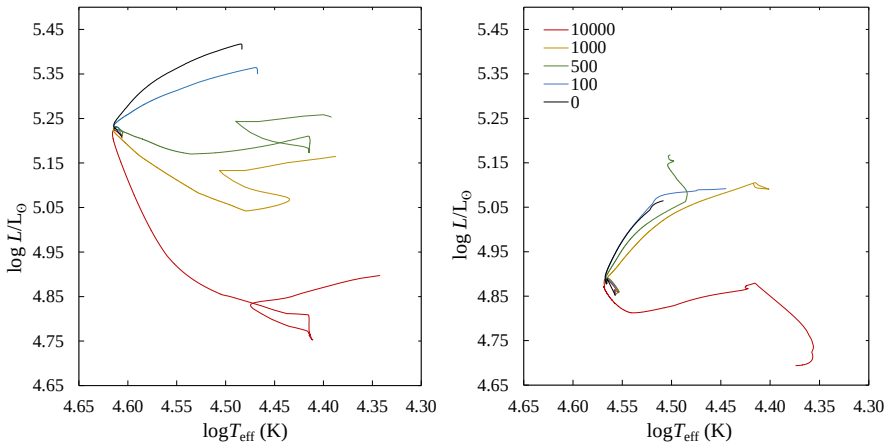

Figure 7.13: HR-diagram for the primary (left) and secondary (right) for v3 with different initial B_W values. $B_W = 10000$, $B_W = 1000$, $B_W = 500$, $B_W = 100$, and $B_W = 0$ are for the red, gold, green, blue, and black lines, respectively.

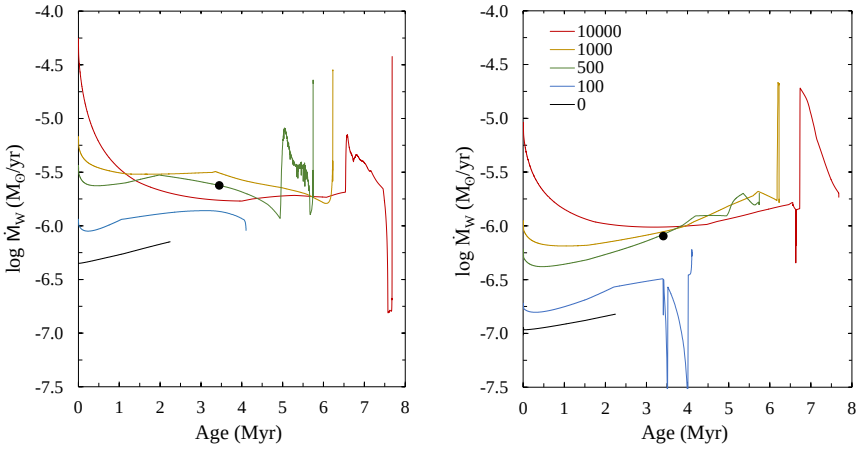

Figure 7.14: Mass loss rate vs Age for the primary (left) and secondary (right) for v3 with different initial B_W values (labeling disussed in Figure 7.13). The black circle shown on the $B_W = 500$ track indicates the beginning of mass transfer by RLOF.

The v3 parameters were used for models using different values of the tidal enhanced wind coefficient B_W. Shown in Figure 7.13, changing B_W from 10^4 to 0 has drastic effects on the binary models. There are two prominent features that can be seen on both Figures 7.13 and 7.14. First is the increase in the age of the system when increasing B_W from 0 up to 10^4. There is a correlation of an increase in mass loss rate and the age of the system. The higher B_W the longer the age of the system until termination. A large $\dot{M}_W$ lowers the star mass and therefore slows the rate of hydrogen burning. For example, for the primary at $t \sim 3$ Myr the core hydrogen mass fraction is 0.482 for $B_W = 10^4$ and 0.414 for $B_W = 500$. Thus for values of $B_W = 0$ or $B_W = 100$ the primary has more mass, and therefore goes through H burning faster and reaches TAMS sooner. This relation is also shown in Section 7.3 for all models (vf05-vf3). Second, when $B_W = 500$, from 4 Myr until the model terminates, mass transfer by RLOF [3] exists. Figure 7.14 shows that the PJ is reached for $B_W = 500$. Note that the red evolutionary track is model v3, which was discussed previously and reaches PJ and SJ. The mass transfer rate by RLOF is small enough ($\dot{M}_{RLOF} \approx 10^{-15} \mathrm{M}_\odot\ \mathrm{yr}^{-1}$) that the secondary does not spin up past its v_{crit}. Changing this parameter along with tidal dissipation has the ability to prevent RLOF events in close binaries. In addition, the increase of $\dot{M}_W$ due to the primary's jump slows the increase of mass loss by RLOF. Since $\dot{a}$ is affected by the bi-stability jump, the increase of $\dot{a}$ is able to prevent the increase of mass transfer by ROLF (see Figure

[3] In this case the majority of the evolution happens during RLOF. Therefore the data were not removed for the B_W cases.

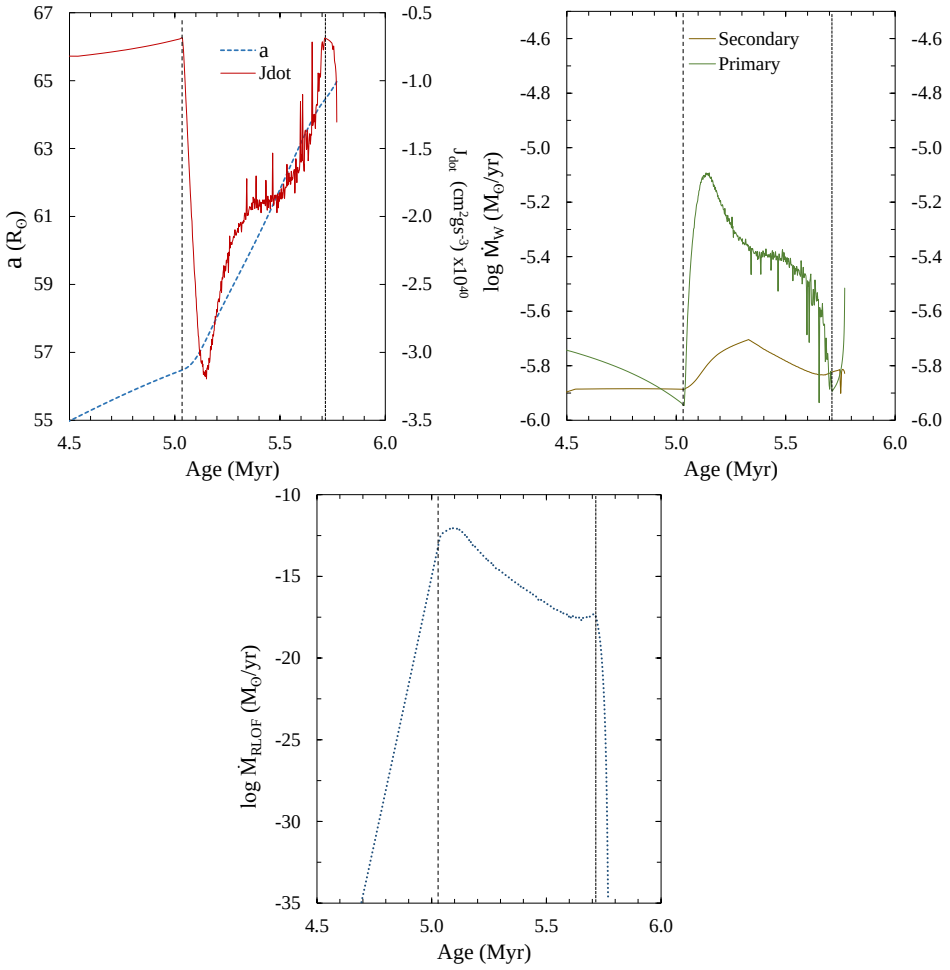

Figure 7.15: Panel of a and $\dot{J}$ vs Age (top left), $\dot{M}_W$ for the primary and secondary (top right) and $\dot{M}_{RLOF}$ vs Age (bottom center). The dashed line at ~ 5 Myrs indicates the beginning of the Primary's bi-stability jump and the dashed line at ~ 5.7 Myrs is the end of the bi-stability jump.

7.15). This enables the model to evolve longer before the secondary begins to reach its break-up velocity. Therefore, the combination of the bi-stability jump, a lower B_W, and altering the period may prevent a RLOF in a close binary system.

Shown in Figure 7.13, as B_W decreases $\log L$ increases, which is not surprising since the primary has more mass due to a lower mass loss rate. This phenomenon is

also shown in Figure 7.16 and is discussed further in depth in the following section. It would be beneficial if B_W was constrained by observations of close massive binary systems for more accurate modeling of $\dot{M}_W$.

7.2 Wind Factor

The wind factor coefficient can increases or decreases the wind mass loss rate by altering its value. The primary exhibits the evolutionary loop for all vf models shown in Figure 7.16. The evolutionary loop for the primary happens at lower $\log L$ for higher values of f_v. Described above, this evolutionary loop represents the TAMS to the onset of helium burning in the HR-diagram for the primary. The reason for the apparent dependency of luminosity on f_v is simple. When the mass loss rate decreases the primary and secondary have higher masses, therefore a higher $\log L$ and shorter lifetimes (see Equation 2.15).

The secondary's evolutionary track, for various values of f_v, resembles model v1, but at different $\log L$. However the secondary evolutionary track for vf3 has a quick increase in $\log L$ and then performs a loop at the end of the evolutionary track. Near the end of vf3 model the secondary has reached the TAMS and then is slowly initiating core helium burning. In the ML-plane (Figure 7.18) the primary experiences PJ at approximately the same mass (sudden decrease in the slope), while the secondary experiences its bi-stability jump at different masses. The shift of the bi-stability jump vs. age is not surprising. If $\dot{M}_W$ is lower the system age will be

shorter (discussed above). Therefore the bi-stability jump will appear to be shifted to the left in Figure 7.18. Apparently, the secondary is more sensitive to a change in mass loss rate than the primary. Note that dashed line goes through the "kink" in all models for the secondary's track in Figure 7.16, because this is the location of the secondary's T_{Jump}.

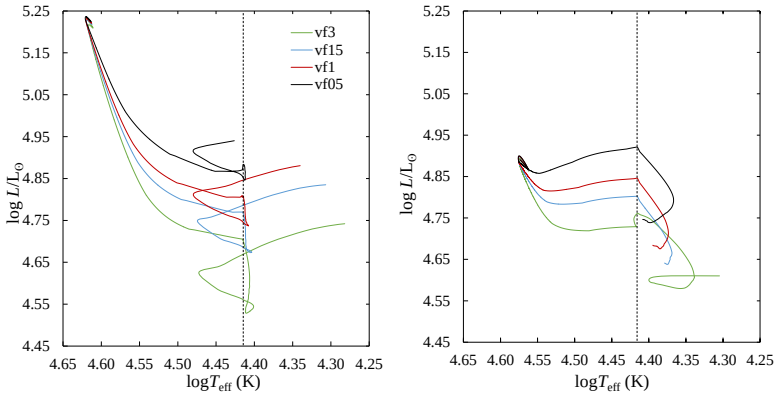

Figure 7.16: HR-Diagram for the primary (left) and secondary (right) for various values of f_v. The vertical black dash line indicates the approximate location of the jump temperature.

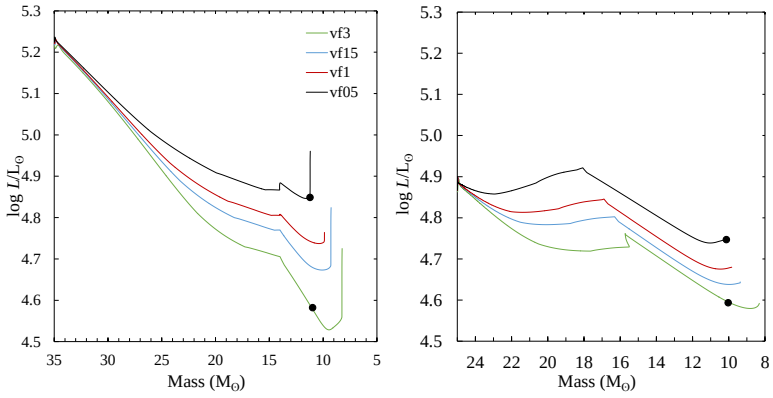

Figure 7.17: Mass Luminosity plane for the primary (left) and secondary (right) for various vales of f_v. The black circles are meant to emphasize the difference of $\log L$ between vf05 and vf3 for the same mass.

As noted above, if a bi-stability jump happens during or past the TAMS, I do not discuss it. However, I would like to explain why vf05 experiences the bi-stability jump (shown in Figure 7.18), but does not cross the T_{Jump} for the primary as shown in Figure 7.16. The jump temperature for the Vink et al. (2001) scheme is dependent on the metallicity and the physical properties of the star. So in the case of vf05, $\log T_{Jump} \approx 4.426$ instead of the location of the black dashed line. Therefore at the end of the vf05 model the primary reaches the bi-stability jump.

The ML-plane shows the difference in final mass and $\log L$ indicated by the black circles in Figure 7.21. For both the primary and secondary it is clear that an increase of the f_v decreases the final $\log L$ and mass of the system.

The evolution of ^{14}N surface abundance (Figure 7.18) and size of the evolutionary loop in the HR-diagram for vf05, vf15 and vf3 are different then models v1-v5. For instance at $\sim 1 - 2.5$ Myr the slope of the ^{14}N abundance changes drastically for vf3 and vf15, is constant for vf05 and dips slightly for vf1. The primary is losing a tremendous amount of material in the beginning, ($\log \dot{M}_W \approx -4.0$) for vf3. Therefore more surface layers of the star are being blown away in a short amount of time for vf3 compared to v1, thus the envelope that is more nitrogen-rich is being exposed.

The vf3 ^{14}N surface abundance evolution levels off between 2 and 4 Myr, as shown in Figure 7.18. The slight increase of ^{14}N surface abundance for vf3 for the primary is due to internal mixing within this time period. The star proceeds through the evolutionary loop stage and ^{14}N abundance begins to increase due to the PJ. For

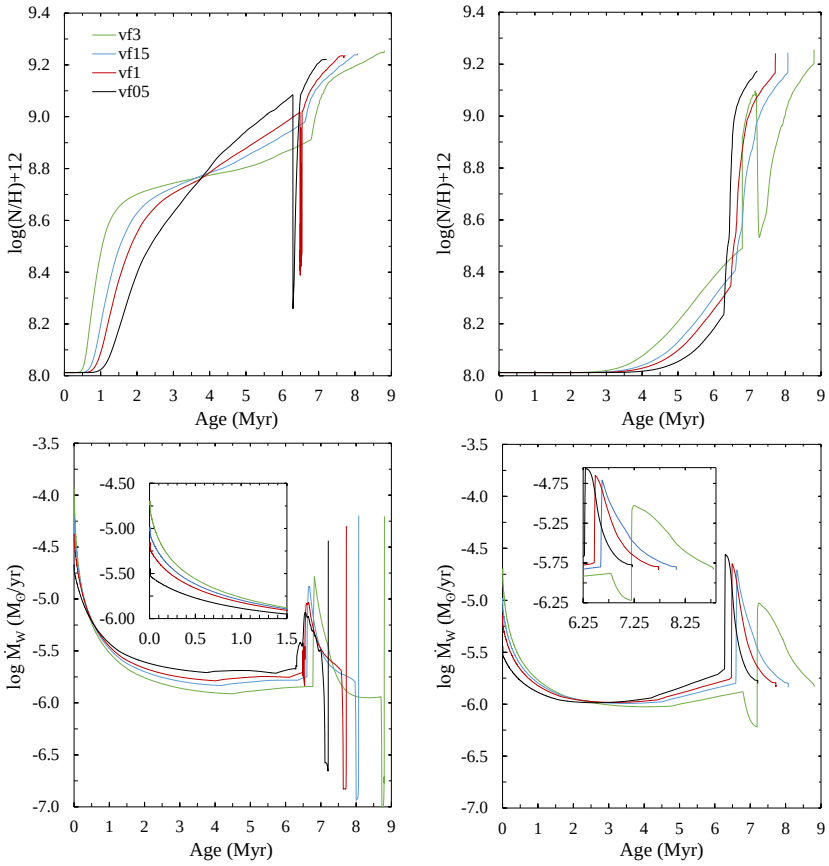

Figure 7.18: ^{14}N surface abundance vs age (top) and $\dot{M}_W$ vs age (bottom) for the primary (left) and secondary (right) for various vales of f_v. Inset of the primary is to indicate the mass loss rate at the beginning of the evolution. The secondary inset is meant to emphasize the bi-stability jump.

vf05 the mass loss is low enough at the beginning that the surface layers are slowly being peeled away and giving a gradual increase of the ^{14}N surface abundance. For vf05 the primary experiences a mass transfer event as in model v1, while the secondary experiences a mass transfer event for only the model vf15. The characteristics of the ^{14}N jump in the secondary shown in Figure 7.18 resemble that of models v3-v5.

As shown in Figure 7.19, the system experiences the bi-stability jump at different

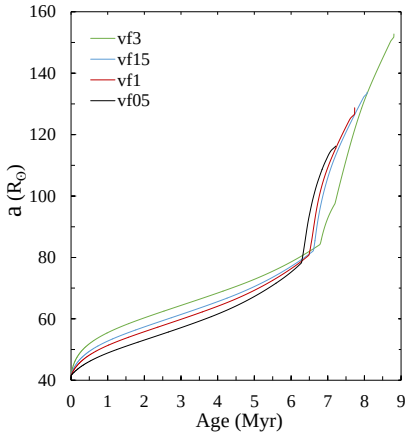

Figure 7.19: Separation vs. age for different f_v values.

ages. In addition, it is easy see the drastic change in $\dot{a}$ due to the bi-stability jumps in the plot. The evolution of the magnitude of $\dot{M}_W$ for SJ of vf3, though lower than vf05-vf13, decays slower than vf05-vf15. Therefore $\dot{a}$ will remain constant on a longer timescale. Figure 7.19 shows that, by changing the f_v, the bi-stability jump has an effect on the change in the binary separation over time.

Changing f_v, as expected, changes the total amount of mass lost from the system at the termination of the models. Higher values of f_v allows the system to evolve longer due to the lower masses of both the primary and secondary. The two interesting cases are the surface ^{14}N and the PJ characteristics at different values of f_v.

7.3 Convective Overshoot

Convective overshoot, as discussed in Section 2.3, has the ability to lengthen the lifetime of the star by having hydrogen pulled from the envelope to the interior of

the star, providing more nuclear fuel over a star's lifetime. Figures 7.20 and 7.21 show a clear indication of the difference in age of the onset of the bi-stability jump and termination of the models. For example, the bi-stability jump for a1 happens at ≈ 6.4 Myr, but for a5 the jump happens later at ≈ 8.2 Myr.

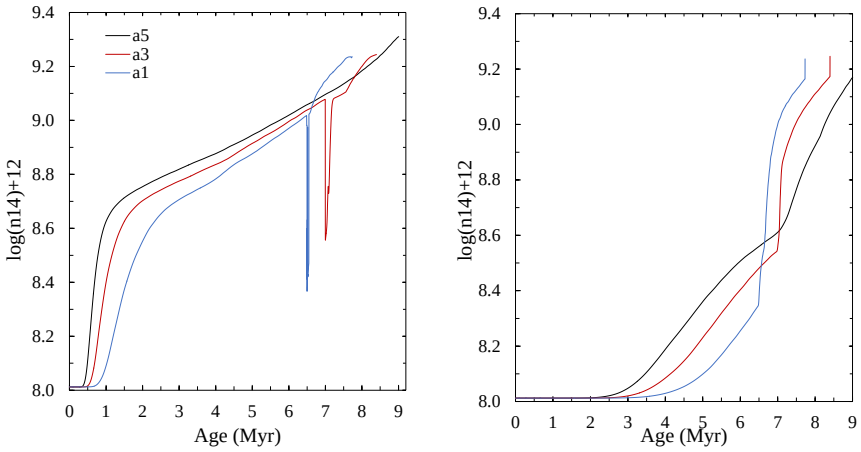

Figure 7.20: ^{14}N surface abundance vs Age for the primary (left) and secondary (right) for α_{ov}

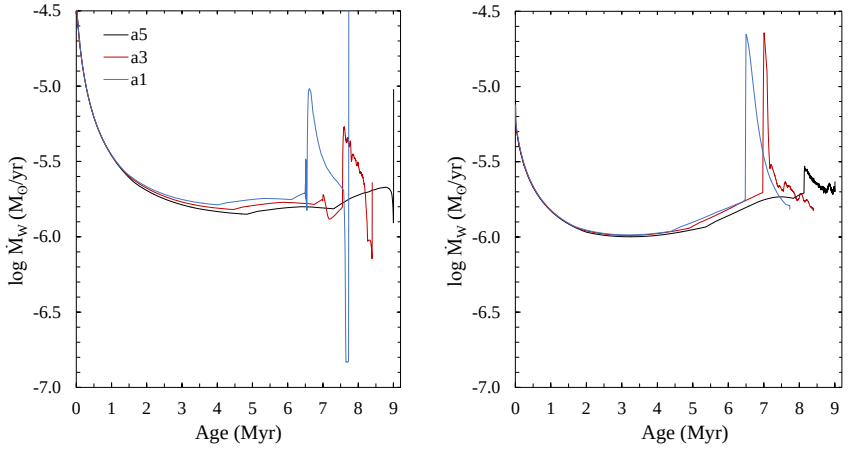

Figure 7.21: $\dot{M}_W$ vs. Age for the primary (left) and secondary (right) for α_{ov} values

The primary, for v1-v5 and vf05-vf3, reaches the TAMS and then helium burning at lower mass, $\log L$, and T_{eff} compared to a5. Core hydrogen exhaustion and then helium burning provide an increase in the luminosity generation from the core and, if the radius remains constant or shrinks, an increase in surface temperature. Convective overshoot allows the primary to remain more massive and compact during the TAMS to helium burning for a5 compared to a1 and a3. Figure 7.23 shows the final mass for a5 of the primary and secondary are higher than a1.

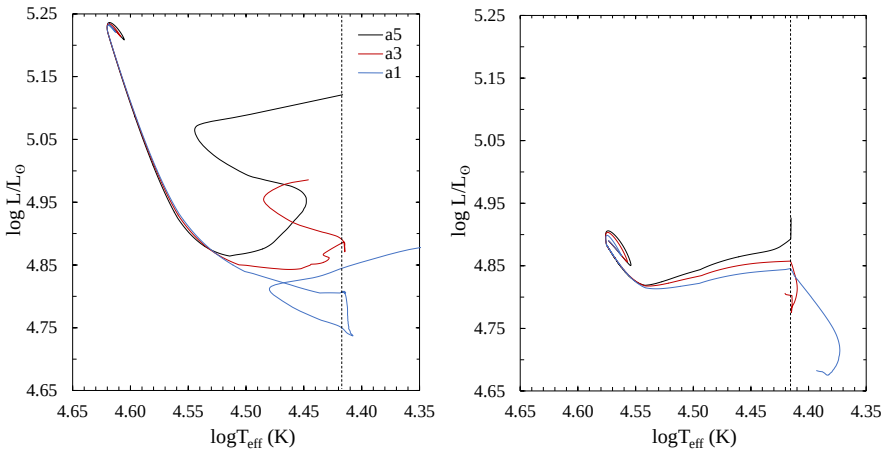

Figure 7.22: HR-diagram for different α_{ov} values for the primary (left) and secondary (right). The black dash-lines indicate the location of jump temperature.

a3 reaches the PJ closer to the TAMS then a1. The primary's bi-stability jump of a3 is smaller due to the difference in $\log L$ and M. The a5 model never reaches the PJ before the onset of RLOF. Note that the primary jump occurs before TAMS. The a3 model reaches SJ and the magnitude of the jump is significantly higher than the PJ of a3. Also, model a5 of the secondary does not reach SJ. The jump that is shown

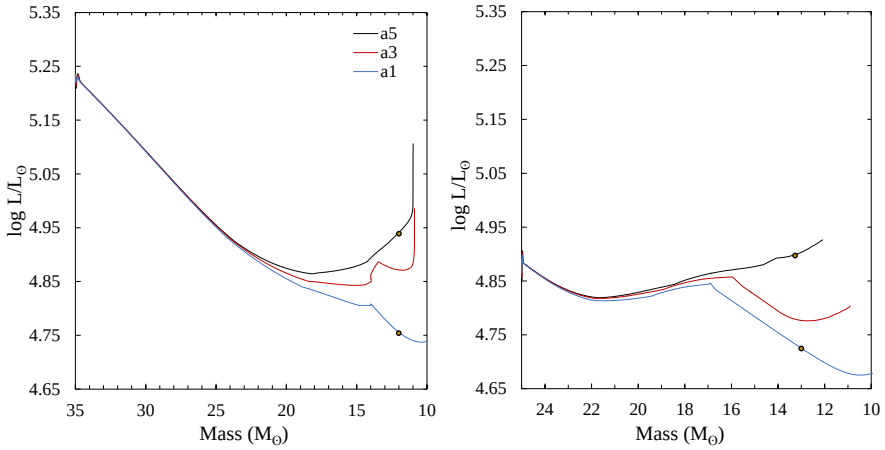

Figure 7.23: Mass-Luminosity plane for different values of α_{ov} for the primary (left) and secondary (right). The black circles are meant to emphasize the difference of a1 and a5 for $\log L$ at the same mass

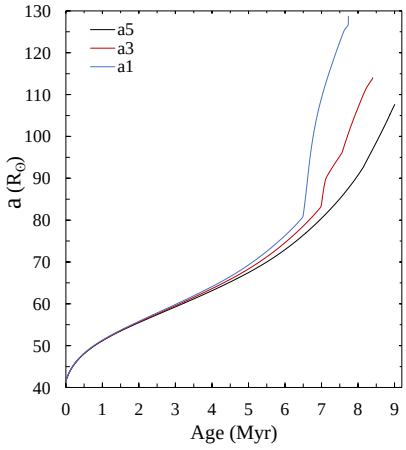

Figure 7.24: Binary separation vs Age for different values of α_{ov}.

in Figure 7.21 of the secondary happens during hydrogen exhaustion. Apparently a convective overshoot value of 0.5 allows the secondary to reach hydrogen exhaustion. This is interesting because the secondary does not reach hydrogen exhaustion for models v1-v5, vf05-vf3, a1, and a3. Since a5 is able to keep the primary more compact and allow the system to age longer, then the secondary is able to reach hydrogen

exhaustion

The deviation in Figure 7.20 from a1 before the onset of the bi-stability jumps is the result of the mixing provided by overshoot. Higher values of α_{ov} implies greater mixing of elements and the Figure provides the best example. Processed nuclear material from the CNO cycle are drawn out into the envelope and surface as discussed in Chapter 2.

Changing α_{ov}, from lower a1 to higher a5, appears to create a more smooth evolution for all physical characteristics (binary and stellar) near the end of the models. The time for the secondary and primary to go through the TAMS to helium burning processes for a5 is longer than a1. Therefore the physical changes of the models for a5 during this period are less drastic than a1. As discussed in Section 7.1.3, the bi-stability jump is shown to affect $\dot{a}$, which is shown in Figure 7.19 by altering the value of f_v. The SJ and BJ do alter $\dot{a}$ for different values of α_{ov} as shown by a1 and a3 in Figure 7.24.

Therefore increasing α_{ov} increases the final mass, $\log L$, and age. The age increases because a higher value of α_{ov} extends the primary's time on the MS, thus preventing a RLOF event. For higher values of α_{ov} the primary and secondary mass are larger from the TAMS to onset of core helium burning. If the mass increases then the luminosity will increase since both are roughly proportional to each other (See equation 2.15).

7.4 Brott & Higgins Comparison

When creating the models for Higgins and Brott comparison, the masses, period, and eccentricity were the same as discussed at the beginning of this Chapter. For Higgins $\alpha_{ov} = 0.3$ and $v_{init} = 120$ km s^{-1} for the primary and $\alpha_{ov} = 0.5$ and $v_{init} = 250$ km s^{-1} for the secondary. Enhanced winds due to rotation was not implemented for Higgins. This was done to follow the work of Higgins & Vink (2019). f_v was set to one for both models. I included gold_tolerance in the provided inlists for greater restriction on energy conservation. All other parameters provided by Higgins (private communication) were not changed. For the Brott models, $v_{init} = 267$ km s^{-1} for the primary and $v_{init} = 271$ km s^{-1} for the secondary. Both the primary and secodary's α_{ov} was set to 0.335. Note that both models terminated because MESA was unable to find an acceptable solution (therefore a small δt).

I would like to note the different initial stellar parameters between the Higgins and the Brott models besides v_{init} and α_{ov}. First, the Brott model includes the Spruit-Taylor dynamo for diffusion of angular momentum while the Higgins model does not. When looking at the Brott model data, the SP-dynamo is occasionally the strongest contributor to mixing in the envelope. Therefore it can effectively keep the envelope and surface rotation from decaying quickly. In addition, the Spruit-Taylor dynamo has the ability to enforce solid body rotation. Second, the initial abundances are different between the models (See Table 2.3). This will have an effect on the stellar winds and the surface nitrogen enrichment (See chapters 2, 4, and 6). Finally different

mixing theory and opacity tables are implemented (See table 2.2).

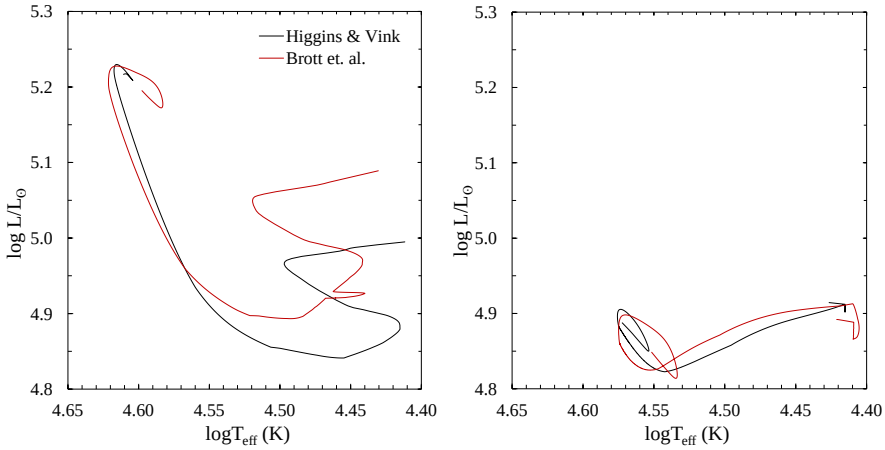

Figure 7.25: HR-Diagram for the primary (left) and secondary (right) comparing the Higgins model and the Brott model in binaries

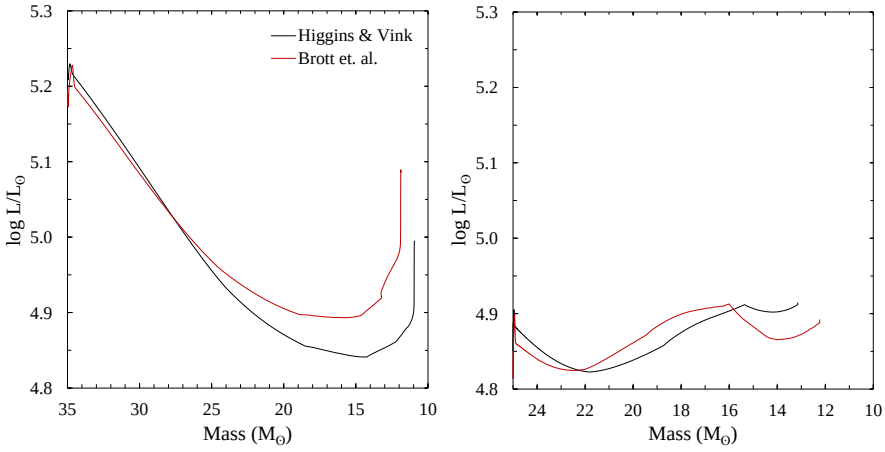

Figure 7.26: Mass-Lumionsity plane for the primary (left) and secondary (right) for the comparison of the Higgins model and the Brott model.

Starting with Figure 7.25, the primary for the Higgins model does a small hook towards the end of its evolution. Its evolutionary path closely resembles that of a3. This is not surprising, because Higgins' initial settings for the primary for v_{init}

and α_{ov} are approximately the same as model a3 (however enhanced winds due to rotation are included for a3). The initial velocity differs by 20 $km\ s^{-1}$ between Higgins model and a3. Actually, all primary graphs of Higgins have approximately the same characteristics as a3.

The primary for the Brott model initially starts to perform a large hook resembling the primary of v3-v5 models. However extremely close to the beginning of the hook the primary closely resembles the secondary's v1-v5 models. The difference between Higgins and Brott's primary in the start of the evolution is due to the Brott model having a higher initial rotation rate and rotational enhanced wind mass loss is included. The primary's evolution for both models after the hook feature resemble each other until hydrogen exhaustion.

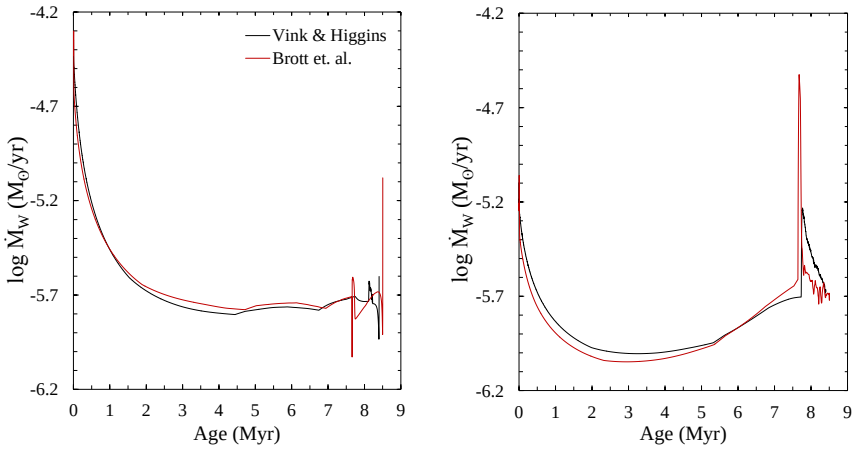

Figure 7.27: $\dot{M}_W$ vs Age comparison for the primary (left) and secondary (right) for the Higgins model and the Brott model.

The differences in the initial abundances and α_{ov} causes the deviation in the evo-

lutionary tracks when comparing Brott and Higgins primaries. Recall that changing v_{init} does not cause a large difference in the evolutionary track in the HR-Diagram when there is a large $\dot{M}_W$. However, as discussed in section 7.3, α_{ov} does have a large effect on the evolution of the primary. The Brott models have convective overshoot value of 0.335 and for Higgins it is 0.3. Therefore the Higgins primary should be cooler and less luminous. This is clearly the case, as shown by Figure 7.25. The Brott primary track resembles the a3 and a5 models near hydrogen exhaustion to helium burning. Shown in the mass-luminosity plane (Figure 7.27) the final mass and luminosity is lower for Higgins compared to Brott. There are two reasons for the difference in mass and luminosity. First, as described previously, the initial abundances of the two models differ. Brott's metallicity is lower than Higgins (see Figure 7.28), and therefore the envelope is more nitrogen-poor than Higgins. This will lead to more fuel for the core of Brott's primary implying a more compact, higher mass, less evolved star. Second, the inclusion of the Spruit-Taylor dynamo may lead to a more hydrogen rich core. The Spruit-Taylor dynamo may enhance chemical mixing by its influence on the rotational velocity through other circulations and instabilities. Higgins' secondary evolutionary track preforms a small loop in the beginning like a5. However, v_{init} for the Higgins secondary is higher than a5 (v_{init} = 100 km s^{-1}) so the hook is more prominent. The more prominent hook is due to the larger change in r_{eq} because the decrease in the secondary's rotational speed is larger (discussed in Section 7.1). After the loop-like feature the secondary follows nearly the same

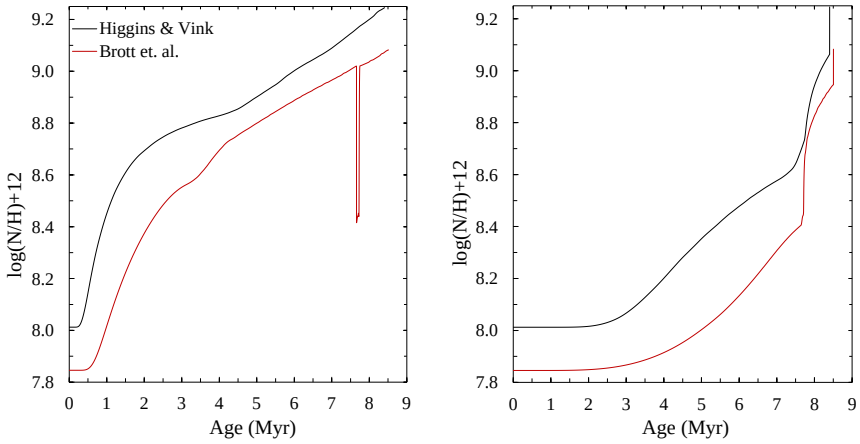

Figure 7.28: ^{14}N surface abundance vs Age comparison for the primary (left) and secondary (right) for the Higgins and Brott models.

evolutionary path as a5. The slight deviations are due to the higher initial rotation velocity of Higgins model. The secondary's evolutionary track for both Brott and Higgins deviates slightly. This is not surprising since the difference in convective overshoot between the models is larger than the primary, where Higgins secondary's convective overshoot is $\alpha_{ov} = 0.5$ and Brott's secondary is $\alpha_{ov} = 0.335$.

The $\dot{M}_W$ for both Higgins and Brott are nearly identical. This is not surprising, since Brott uses the "Dutch" wind scheme and, when $T_{eff} \leq 10$ kK and surface $^1H < 0.4$ it will switch to Nugis & Lamers (2000) wind scheme, otherwise the "Dutch" wind scheme applies the Vink et al. (2001) wind scheme. The "Dutch" T_{eff} and surface ^1H conditions are not reached in Brott's model and therefore both the Brott and Higgins models use the Vink et al. (2001) scheme. Unfortunately, as shown in Figures 7.27 and 7.25 the bi-stability jump for both stars for Brott's models happens at TAMS moving towards helium core burning and therefore the results are not reliable. The

Higgins primary and secondary also experience the bi-stability jump at the TAMS.

The ^{14}N surface evolution of both models closely resemble each other for both the primary and secondary. The $\approx$ 0.2 dex difference for the initial ^{14}N surface abundance in Figure 7.28 is due to the difference in initial abundances of the two models. The differences in evolution can be attributed to the difference in v_{init}, α_{ov}, and different types of instabilities used (ST-dynamo for Brott). See sections 7.1 and 7.3 for the influence of v_{init} and α_{ov} on the ^{14}N surface abundance for both the primary and secondary. The sudden change in ^{14}N abundance at $\sim$ 8 Myrs is due to the bi-stability jump (See section 7.1).

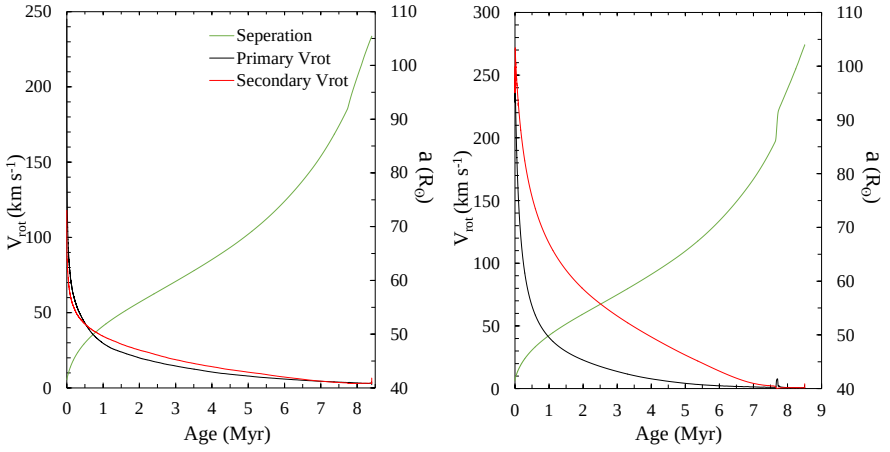

Figure 7.29: Binary separation, primary and secondary rotation vs Age for the primary (left) and secondary (right). The left graph is the Higgins model and the right graph is the Brott model.

The surface velocity for the secondary of Brott decays slower than Higgins models as shown in Figure 7.29. The primary for Brott is has less shear in its envelope than the Higgins primary. This could be due to the inclusion of the Spruit-Taylor

dynamo in Brott's model, which may be effectively "smoothing" out the shears and preventing the surface rotation rate from decreasing quickly. The change in the period and separation for both Brott and Higgins are gradual and follows the same relationship as v1-v5 from the beginning of the model to 5 Myrs. However unlike the the sudden change in $\dot{a}$ in models v1-v5 due to the bi-stability jumps, Higgins and Brott $\dot{a}$ only gradually increase. The $\dot{a}$ for Higgins and Brott's models follows closely for models a3 and a5.

7.4.1 Grid of Masses

I end this chapter with an analysis of the result of varying secondary and primary masses using Brott and Higgins parameters. I created a grid of models for the primary and secondary by using the condition that $q \approx 0.7$ and changing the primary mass by increments of $5M_{\odot}$. Starting from the highest mass binary system to the lowest, the primary and secondary masses are as follows: (60+40) $M_{\odot}$, (55+40) $M_{\odot}$, (50+35) $M_{\odot}$, (45+30) $M_{\odot}$, (40+30) $M_{\odot}$, (35+25) $M_{\odot}$, (30+20) $M_{\odot}$, and (25+20) $M_{\odot}$. The (35+25)$M_{\odot}$ is used as a base comparison since it was discussed in depth. For Higgins models ranging from (35+25) $M_{\odot}$ to (60+40) $M_{\odot}$ the evolutionary track is the same for the primary. The only difference of course is the increase in $\log L$ and $\log T_{eff}$ at the end of the model, which can be attributed to the increase in the primary's mass.

For the (25+20) $M_{\odot}$ system, the primary's evolutionary track shows the loop feature shown in the v1-v5 models. The secondary track resembles the v1-v5 models.

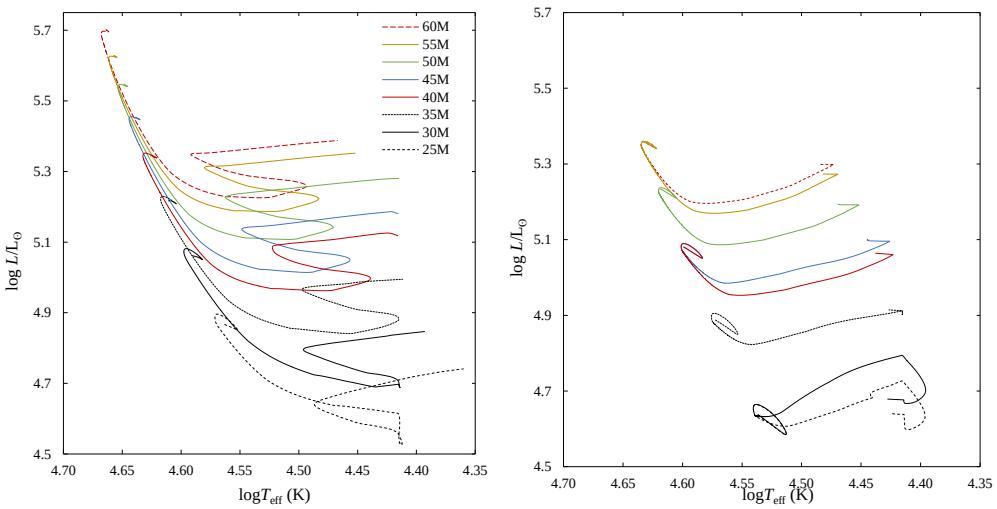

Figure 7.30: HR-Diagram of the Higgins model for the primary (left) and secondary (right) for different primary and secondary masses.

Apparently near this mass range the Higgins models will reproduce the track of the v1-v5 models. Therefore the bi-stability jump may be more prominent in binaries with lower masses using the Higgins parameters. Binary masses between (40+30) $M_\odot$ and (60+40) $M_\odot$ reach TAMS sooner and therefore will not reach the PJ. The secondary's evolutionary track, in this mass range, behaves like the a5 model which did not reach SJ. Therefore the bi-stability jump will not happen pre-RLOF for binary masses in the ranges of (40+30) $M_\odot$ to (60+40) $M_\odot$.

The Brott model is fascinating because either below or above the (35+25) $M_\odot$ evolutionary track shows the same feature. Unlike the Higgins model for (25+20) $M_\odot$ binary system, Brott's primary evolutionary track does not exhibit the loop-like feature. However the secondary for Brott follows closely that of Higgins for the (25+20) $M_\odot$. The reasoning follows from previous arguments; the initial values of

v_{init} and α_{ov} for the secondary are close for Higgins and Brott, thus their evolutionary tracks will be similar.

It appears there is a transition between the (25+20) $M_{\odot}$ and (35+25) $M_{\odot}$ binary systems where the evolutionary tracks are vastly different for both the primary and secondary. At lower masses the secondary clearly reaches its bi-stability jump as shown in Figures 7.30 and 7.31. The primary performs a loop like feature for the Higgins case at (25+20) $M_{\odot}$. This transition can also be seen between a1 and a3 models and comparison between vf05 and vf3. It may have to do with the combination of the mass of the primary and secondary and $\dot{M}_W$ near this period of evolution.

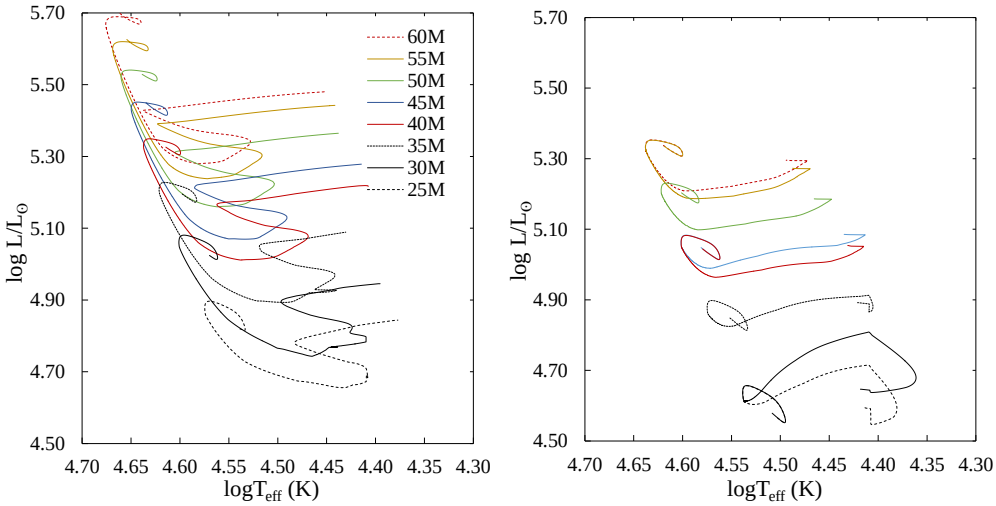

Figure 7.31: HR-Diagram of the Brott model for the primary (left) and secondary (right) for different primary and secondary masses.

Chapter 8

Count Rates from Predicted Wind-Blown Bubble Using PIMMS

Using the numerical outputs of the models, predictions can be made for future observations. This includes the wind-blown bubbles discussed at the end of Chapter 6. Observations can determine the: M_{sys}, M_1, M_2 a, v_{orb}, P_{orb}, the ^{14}N surface abundance, $\dot{M}_W$, v_∞, and T_{eff}. However some characteristics will be easier to determine than others, for instance, T_{eff}. All the characteristics of the models presented can be used to either check the literature for possible candidates or predict future observations using PIMMS (discussed in the next section). However, using $\dot{M}_W$, t_{sys} and v_∞ a predication can be made regarding the observability of a wind-blown bubble.

Several assumptions need to made to model the bubbles: the ambient ISM density n_0, the foreground absorption column density N_h, and the distance to the binary system, r. These parameters, and values discussed in the section, are based on Strickland & Stevens (1998). They follow the work of Weaver et al. (1977) and Weaver et al. (1978) to model bubbles around massive O and Wolf-Rayet stars within the first 10-20 thousand years.

8.1 Wind-Blown Bubbles

As discussed at the end of Chapter 6, stars, when surrounded by an ISM that is dense enough, will create "Wind-Blown bubbles" or a shock fronts. Regions within the bubbles are hot ($T \sim 10^6$ K, as shown in Table 8.1) in comparison to $T \sim 100$ K for the ISM . In region (b) soft X-rays[1] are produced by Bremsstahlung radiation[2]. There are currently two telescopes that can observe soft X-rays, the Chandra X-ray Observatory and X-ray Multi-Mirror Mission-Newton (XMM).

The expansion velocity and current radius can be found by assuming an ambient ISM density of $n_0 = 10$ cm^{-3} (Strickland & Stevens 1998) and using equations 6.30 and 6.31 (shown in Table 8.1). In Table 8.1 H60M+40M and H25M+20M implies using Higgins & Vink (2019) parameters for a system of mass with (60 +40) $M_\odot$ and (25 +20) $M_\odot$, respectively. The reference to "High" and "Low" has to do with the size of the bubble: at the end of the evolution the bubble's radius is larger and earlier it is smaller. This can give an observer an order of magnitude estimate for radius of the bubble produced by the various models.

The information in Table 8.2 is important for using PIMMS to predict the required observing time. In order to calculate the flux of an object, as shown in Equation 6.32, the object distance needs to be known. I use $r = 2$ kpc which follows the work of Strickland & Stevens (1998). This is reasonable, as OB stars, though few in number,

[1]Soft X-rays have photon energies below ~ 5 keV as shown in Table 8.2

[2]Bremsstahlung radiation is caused by electron scattering, in the case of region (b), this would be due to either electron scattering off of a free electrons or protons

are extremely luminous. In addition, the bubbles themselves are luminous in the soft X-rays. However, interstellar absorption due to material along the line of sight to the bubble can cause the source flux to be substantially attenuated.

Table 8.1: ISM and Bubble Characteristics

Model	L_{Mech}/L_{36}	t_6	R_2	v_2
-	-	-	(pc)	(km s^{-1})
H60M+40M	1109	5.92	319	31.9
vf3	115	8.81	257	17.3
a5	8.824	9.01	156	10.3
Higgins High	8.390	8.4	148	10.4
Higgins Low	124.7	0.19	5.14	26.96
v3	10.15	7.68	146	11.3
Brott High	3.18	8.5	77.54	5.4
Brott Low	49.83	0.28	17.36	36.68
H25M+20M	0.14	10.9	75.9	4.13
Bv3	0.13	5.77	52	5.29
v3off	0.007	3.95	23.1	3.46

L_{Mech}/L_{36} is the mechanical luminosity divided by 10^{36} ergs s^{-1} and t_6 is the age of the system divided by 10^6 yrs. The data is organized by the size of the predicted bubble.

8.1.1 Possible Observation

To use PIMMS five parameters need to be input. They are the unabsorbed flux of the object as seen from the telescope, N_h, and kT_b (the hot gas temperature in energy units for region (b)). The flux and kT_b are calculated as shown in Tables 8.3 and 8.4. Strickland & Stevens (1998) used $N_h = 3.16 \times 10^{21}$ cm^{-2} for their models. The final two parameters are the input and ouput energy range. Both are set to (0.1-2) keV for

Table 8.2: Bubble Characterstics for Region (b)

Model	n_b	T_b	L_b	R_c
-	(cm^{-3})	(K)	(ergs s^{-1})	(pc)
Multiplier	10^{-3}	10^6	10^{35}	-
H60M+40M	14.5	3.16	824	169
vf3	7.89	2.83	110	136
a5	3.00	1.23	0.32	82.7
Higgins High	4.98	2.31	5.23	78.5
Higgins Low	72.2	2.68	5.71	4.32
v3	5.63	2.46	7.56	77.3
Brott High	5.05	2.32	8.11	65.1
Brott Low	50.0	2.59	3.14	14.6
H25M+20M	1.83	1.51	0.033	40.3
Bv3	2.42	1.34	0.012	27.3
v3off	1.80	1.10	0.00037	12.2

L_b, T_b, n_b are the luminosity, temperature, density of region (b) and R_c is the radius from the star to the shock interstellar gas (Shown in Figure 6.3).

this exercise. The input/output energy range sets the spectral bandwidth that will be used to calculate the count-rate. Chandra and XMMs energy ranges are (0.2-10) keV and (0.4-10) keV, respectively.

Table 8.3 shows the calculations for Chandra's ACIS-I instrument for the various models while Table 8.4 shows XMM values. The count-rates had to be adjusted for the size of the bubble. PIMMS assumes the object fills the telescope field of view. However the bubbles above, based on their size and distance, have angular sizes larger then the field of views of the telescopes. Therefore the ratio of the array area over the bubble area was calculated. Then taking the ratio times the PIMMS output gives the correct count-rate.

However, some of the model bubbles are enormous. Therefore using Chandra

would be prohibitive. The required observing time to observe the entire bubble using Chandra would be long. For example, the bubble predicted for model v3 subtends 7^o and the count-rate is 0.026 counts/s for Chandra, while XMM's predicted count-rate for v3 is 1.316 counts/s. Therefore XMM might be more fruitful for the larger modeled bubbles, because of its larger field of view. Note that the count-rate for the predicted bubble of v3off is so low for both Chandra and XMM the likelihood of finding the bubble is minuscule.

Columns 2-5 in Tables 8.3 and 8.4 are the input parameters for PIMMS. The last column in each table are the corrected outputs from PIMMS for both Chandra's ACIS-I instrument and XMM's thin instrument. ACIS-I was used because it has a square field of view. The thin instrument for XMM was used because it provided the highest count-rate. Between Higgins High and Lower bound the count rates may be fruitful for an observation. A proposal could be made to observe a younger binary system for the Higgins model, for which R_2 is small, n_b is high, and the count-rate is high. The above argument made for the Higgins model can be applied for the Brott model as well. The generation of Bremsstahlung radiation will increase when n_b is high because there are more electron and proton scattering events. Therefore the amount of flux coming from the bubble will grow and the predicted count-rates will increase.

Tables 8.5-8.10 presents the numerical output for the evolution of the primary star, secondary star, and binary parameters of the Higgins and Brott models. I used

Table 8.3: Parameter Inputs for PIMMS & Count Rates for Chandra ACIS-I

Model	kT_b keV	Source Flux erg/cm^2/s (10^{-9})	Count Rate counts/s (10^{-3})
H60M+40M	0.272	688	1520
vf3	0.244	91.8	214
a5	0.106	0.26	0.299
Higgins High	0.199	4.37	13.9
Higgins Low	0.231	4.77	9040
v3	0.212	6.32	26.8
Brott High	0.200	1.69	9.75
Brott Low	0.223	2.65	202
H25M+20M	0.130	0.028	0.0429
Bv3	0.116	0.001	0.0178
v3off	0.095	0.00031	0.000844

Table 8.4: Parameter Inputs for PIMMS & Count Rates for XMM Thin

Model	kT_b keV	Source Flux erg/cm^2/s (10^{-9})	Count Rate counts/s
H60M+40M	0.272	688	51.3
vf3	0.244	91.8	8.41
a5	0.106	0.26	0.00640
Higgins High	0.199	4.37	0.7532
Higgins Low	0.231	4.77	386.2
v3	0.212	6.32	1.316
Brott High	0.200	1.69	0.528
Brott Low	0.223	2.65	9.11
H25M+20M	0.130	0.028	0.00565
Bv3	0.116	0.001	0.00307
v3off	0.095	0.00031	0.000234

M_{sys} as an evolutionary variable because it changes so drastically and M_{sys} can be determined observationally. Typically the numerical output of models are presented by specific evolutionary stages of the binary system or stars themselves e.g. TAMS or the onset of RLOF. However RLOF is not studied here and the primary star reaches TAMS near the end of the models. Therefore intervals of $M_{sys} = 5\mathrm{M}_{\odot}$ were used instead of a binary or single star evolutionary stage.

All physical quantities of the six tables can be determined observationally as explained throughout this thesis. The evolution of each quantity for the Higgins and Brott models has been explained in chapter 7. If an observer were to find the bubble, at say $t_{sys} \approx 4$ Myr then hopefully they will be able to determine the binary mass, $\log L$ and $\log T_{eff}$ of the primary and secondary stars. Using these values as constraints and using the information provided in Tables 8.5-8.10 to match the model information to observed values. Matching the tables data to an observation result may be the connection between the grid of models and observations.

Table 8.5: Stellar Evolution Information from Higgins model

M_{sys} ($\mathrm{M}_{\odot}$)	M_1 ($\mathrm{M}_{\odot}$)	$\log L_1$ ($\mathrm{L}_{\odot}$)	$\log T_{eff,1}$ (K)	M_2 ($\mathrm{M}_{\odot}$)	$\log L_2$ ($\mathrm{L}_{\odot}$)	$\log T_{eff,2}$ (K)
60	35	5.22	4.61	25.0	4.89	4.57
55	30.7	5.11	4.6	24.3	4.86	4.57
50	26.8	5.00	4.58	23.3	4.84	4.56
45	23.2	4.92	4.55	21.9	4.82	4.54
40	19.8	4.87	4.52	20.3	4.84	4.52
35	16.5	4.87	4.52	18.5	4.86	4.49
30	13.6	4.85	4.44	16.5	4.90	4.44
25	11.4	4.88	4.42	13.7	4.90	4.42

Table 8.6: Stellar Evolution Information from Higgins Model

M_{sys} ($M_\odot$)	$v_{rot,1}$ (km s^{-1})	$\log(N/H)_1 + 12$	$v_{rot,2}$ (km s^{-1})	$\log(N/H)_2 + 12$
60	245	8.01	118	8.01
55	60.1	8.01	53.0	8.01
50	35.2	8.31	38.0	8.01
45	20.7	8.68	25.8	8.01
40	11.8	8.82	15.4	8.15
35	6.69	8.95	8.70	8.42
30	4.3	9.1	4.30	8.58
25	3.03	9.22	3.07	9.01

Table 8.7: $\dot{M}_W$ & Binary Evolution from Higgins Model

M_{sys} ($M_\odot$)	T (days)	a ($R_\odot$)	$v_{orb,1}$ (km s^{-1})	$v_{orb,2}$ (km s^{-1})	$\log \dot{M}_{W,1}$ ($M_\odot$ yr^{-1})	$\log \dot{M}_{W,2}$ ($M_\odot$ yr^{-1})	q
60	4.00	41.5	219	306	-4.36	-5.18	0.714
55	4.78	45.4	212	268	-4.91	-5.50	0.792
50	5.79	50	203	234	-5.35	-5.76	0.869
45	7.15	55.6	191	202	-5.67	-5.97	0.945
40	9.05	62.5	177	173	-5.79	-6.00	1.03
35	11.9	71.6	161	144	-5.77	-5.92	1.12
30	16.3	84	143	118	-5.74	-5.74	1.21
25	23.6	101	119	98.6	-5.68	-5.55	1.21

Table 8.8: Stellar Evolution Information from Brott model

M_{sys} ($M_\odot$)	M_1 ($M_\odot$)	$\log L_1$ ($L_\odot$)	$\log T_{eff,1}$ (K)	M_2 ($M_\odot$)	$\log L_2$ ($L_\odot$)	$\log T_{eff,2}$ (K)
60	35.0	5.20	4.60	25.0	4.85	4.55
55	30.8	4.61	5.11	24.2	4.84	4.57
50	26.9	5.01	4.58	23.2	4.83	4.56
45	23.2	4.94	4.56	21.9	4.83	4.55
40	19.6	4.90	4.53	20.4	4.85	4.52
35	16.3	4.89	4.50	18.7	4.89	4.48
30	13.6	4.91	4.47	16.4	4.91	4.42
25	12.3	4.96	4.44	12.7	4.88	4.41

Table 8.9: ^{14}N & v_{rot} Evolution from Brott model

M_{sys} ($M_\odot$)	$v_{rot,1}$ (km s^{-1})	$\log(N/H)_1 + 12$	$v_{rot,2}$ (km s^{-1})	$\log(N/H)_2 + 12$
60	247	7.85	257	7.85
55	92.4	7.85	182	7.85
50	39.6	8.04	114	7.85
45	18.0	8.48	68.4	7.85
40	6.60	8.74	36.8	7.94
35	2.22	8.89	13.4	8.14
30	1.05	9.00	2.41	8.38
25	0.655	9.06	0.736	8.90

Table 8.10: $\dot{M}_W$ & Binary Evolution from Brott Model

M_{sys} ($M_\odot$)	P_{orb} (days)	a ($R_\odot$)	$v_{orb,1}$ (km s^{-1})	$v_{orb,2}$ (km s^{-1})	$\log \dot{M}_{W,1}$ ($M_\odot$ yr^{-1})	$\log \dot{M}_{W,2}$ ($M_\odot$ yr^{-1})	q
60	4.00	41.5	219	306	-4.37	-5.12	0.714
55	4.80	45.6	211	269	-5.08	-5.65	0.787
50	5.81	50.1	202	234	-5.47	-5.90	0.861
45	7.15	55.6	191	202	-5.70	-6.04	0.942
40	9.04	62.5	178	172	-5.77	-6.02	1.04
35	11.8	71.5	163	142	-5.72	-5.65	1.15
30	16.2	83.7	143	119	-5.69	-5.72	1.21
25	23.2	100	111	108	-6.49	-6.35	1.03

Chapter 9

Summary

9.1 Conclusion

Two single star models (Higgins & Vink 2019 and Brott et al. 2011) were used to study the interactions and evolution of a close massive binary system using MESA. Higgins & Vink (2019) parameter values were used to model the observations of the detached massive binary system HD 166734, while Brott et al. (2011) created an extensive grid of models to match the observations of Hunter et al. (2008). Four parameters were varied and studied extensively as follows: the initial rotation rate (v_{init}), step convective overshoot (α_{ov}), wind factor (f_v), and the tidal enhancement factor (B_W) using the inlist provided by Higgins (private communication). A comparison was made between the Higgins & Vink (2019) and Brott et al. (2011) models using their parameters that were constrained to observations. A grid of different primary and secondary masses was created using the parameter values of Higgins & Vink (2019) and Brott et al. (2011). In the majority of models, the bi-stability jump temperature was reached, which induces a dramatic increase in the mass loss rate. Finally, using the data from the models, the temperature, luminosity and radius of a wind-blown bubble were calculated. The calculated values were used to estimate the count rate for observations with the Chandra X-ray Observatory and XMM using PIMMS.

Varying v_{init} slightly increases the main sequence width. However the evolutionary

tracks remain, in most part, the same for different values of v_{init}. The final ^{14}N surface abundance for the lowest and highest v_{init} did not change, implying that v_{rot} was not the only contributor to the change in ^{14}N surface abundance. Not allowing for tidal enhanced winds and wind mass transfer clearly showed how influential $\dot{M}_W$ is on the ^{14}N surface abundance and the rotational velocity. After about 2 Myrs the ratio of the rotation velocities of the secondary star to the primary star was ~ 2.6 and for the ^{14}N surface abundance of the primary to secondary was ~ 3.6. Therefore the primary star was more nitrogen-rich but rotated slower. $\dot{M}_W$ due to binarity may be the reason for slow rotators that have a high ^{14}N surface abundance in the LMC (Hunter et al. 2008).

The Mass-Luminosity plane provided insight when changing the mass loss rate parameters for tidally enhanced winds and increasing the rate of mass loss by the wind factor (f_v). As f_v and B_W values increased the final luminosity and mass of the system decreased. This follows the theory of the mass luminosity plane where an increase in these parameters would make the "ML-vector" point downward on the plot, and a decrease of the parameters will move it up on the plane. When $B_W = 500$ the system experiences mass transfer by Roche Lobe overflow, but the secondary does not spin up. Therefore for lower values of the tidally enhanced wind parameter and if the secondary and/or primary reaches their bi-stability jump, than it is possible that a Roche-lobe overflow event may be prevented in massive close binary systems. For models when $f_v = 1.5$ and $f_v = 3$ for the primary the wind mass rate was so high the

increase of ^{14}N surface abundance vs. age slowed. The high mass loss rate is stripping the surface of the primary and therefore exposing the nitrogen-rich envelope.

When increasing α_{ov} from 0.1 to 0.5 the age of the system increased. This is not surprising, because for higher α_{ov} the amount of hydrogen being drawn from the envelope to the core increases. Therefore, the primary star remains compact and reaches the TAMS later. There is a slight deviation after 5 Myrs for ^{14}N surface abundance vs age for various α_{ov} values. Higher values α_{ov} are extracting more CNO-cycle elements to the envelope.

When comparing the Higgins and the Brott models, the deviations in the beginning of the evolutionary track in the HR-Diagram were due to the difference in v_{init} for the primary, and also the use of rotationally enhanced winds for the Brott models. Both models shared similarities for the evolution of the secondary, however this was not true for the primary. This is partly due to the difference in v_{init} and α_{ov}. For example, the difference can be seen between Higgins' primary and Brott's primary, where $\alpha_{ov} = 0.3$ and $v_{init} = 120$ km s^{-1} for Higgins' primary and for Brott's primary $\alpha_{ov} = 0.365$ and $v_{init} = 267$ km s^{-1}.

The deviations in the tracks could also be attributed to the inclusion of the Spruit-Taylor dynamo mixing angular momentum. In addition Brott et al. (2011) use a lower metallicity than Higgins models which can also induce the deviation. Both the Higgins and Brott models did not experience the bi-stability jump before the TAMS. Between the primary and secondary mass ranges of (25 + 20) $M_\odot$ to (35 + 25) $M_\odot$ for both

Higgins and Brott models there appears to be a transition period where there is a noticeable difference in the evolutionary tracks of both the primary and secondary. For Higgins' (25 + 20) $M_{\odot}$ model, both the primary and secondary will experience the bi-stability jump. For Brott's (25 + 20) $M_{\odot}$ model only the secondary will experience the bi-stability jump. For system masses around (60 + 40) $M_{\odot}$ the system terminates before either Higgins or Brotts models reach the bi-stability jump before TAMS.

The changes to the binary system were due to the large mass loss rate of both the primary and secondary. The contribution to spin-orbit coupling and tides were two orders of magnitude smaller than the change in orbital angular momentum due to mass loss. The bi-stability jump provided the greatest example of this. The significant increase of the mass loss rate due to the bi-stability jump does increase $\dot{a}$ and $\dot{P_{orb}}$. This was clearly shown in the $\dot{J}$ graphs for different v_{init}. It appears the bi-stability jump does have an impact on the evolution of the binary system. When the jumps of the secondary and primary overlap, depending the magnitude of jumps of both, the primary or secondary will experience mass transfer. This was clearly shown in the majority of the ^{14}N surface abundance plots.

Wind blown-bubble calculations were made using the equations of Weaver et al. (1977) and Weaver et al. (1978). From the information from the models, and using PIMMS, soft x-ray count rates were estimated. A broad range of calculated count rates were created for the Higgins and Brott models to use to compare to binary and stellar model characteristics. With this information it may be possible to propose for

observation time for either of the telescopes.

In all models that included the tidally enhanced winds, the primary and secondary became slow rotators and nitrogen rich near the end of the model. The primary early on in its evolution was more nitrogen rich and rotating more slowly then the secondary. The bi-stability jump does have a noticeable effect on binary mechanics, and may prevent a RLOF event. A future study would need to be made to see if this is true.

9.2 Future Work

Possible future work would include searching the literature for observed systems or proposing for observing time on the Chandra X-ray Observatory. When performing this thesis it was found the Tout & Eggleton (1988) coefficient B_W was large and the value has not been constrain for massive binary star observations. It would be beneficial to have more accurate value since the range of values used in the literature is large. The location of the jump temperature is believed to be lower than what is used in MESA $T \approx$20 kK. This change would prevent binary models from ever experiencing the jump. A new grid of models would need to be created to account for this new jump temperature. Finally, expanding the model grid to include the metallicities of the Small and Large Magellanic Cloud would expand the possible observed sample size.

Acknowledgments

This research would not have been possible without the help of Erin Higgins and Zsolt Keszthelyi. I would like to thank the MESA community for allowing me to use MESA for my research project and the help they provided whenever issues arose. I would like to express my sincere gratitude to my advisor Dr. Paul Eskridge for his patience, wealth of knowledge, wisdom, and encouragement during the completion of my thesis. I would like to thank my committee members Dr. Rebecca Bates and Dr. Analía Dall'Asén for their insightful suggestions and comments.

I am grateful to my friends and fellow colleges for their support throughout my academic career. I am indebted to my brother Tim and my sisters Samantha and Melissa for their words of encouragement, help, and support. A heartfelt thanks goes to my loving parents Tom, Jennifer, and Ingrid who were always there for me. My sincere thanks go to my grandparents and the rest of my family.

Bibliography

Abbott, D. C. 1982, The Astrophysical Journal, 259, 282

Alfvén, H. 1942, Nature, 150, 405

Angulo, C., Arnould, M., Rayet, M., et al. 1999, Nuclear Physics A, 656, 3

Asplund, M., Grevesse, N., & Sauval, J. 2004, Astronomy & Astrophysics of the Pacific Conference Proceedings

Bahcall, J. N., Basu, S., Pinsonneault, M., & Serenelli, A. M. 2005, Astrophysical Journal, 618, 1049

Baker, N., . R. K. 1959, Zeitschrift fur Astrophysik, 48, 140

Bjorkman, J. E., & Cassinelli, J. P. 1993, Astrophysical Journal, 409, 429

Böhm-Vitense, E. 1958, Zeitschrift fur Astrophysik, 46, 108

Bondi, H., & Hoyle, F. 1944, Monthly Notices of the Royal Astronomical Society, 104, 273

Bouret, J. C., Hillier, D. J., Lanz, T., & Fullerton, A. W. 2012, Astronomy & Astrophysics, 544, A67

Brott, I., de Mink, S. E., Cantiello, M., et al. 2011, Astronomy & Astrophysics, 530, A115

Carroll, B., & Ostlie, D. 2007, An Introduction to Modern Astrophysics, 2nd edn. (SFP Addison-Wesley), 1278

Cassisi, S. 2007, in IAU Symposium, Vol. 241, Stellar Populations as Building Blocks of Galaxies, ed. A. Vazdekis & R. Peletier, 3–12

Castor, J. I., Abbott, D. C., & I., K. R. 1975, Astrophysical Journal, 195, 157

Chu, S., Ekström, L., & Firestone, R. 1999, The LUND/LBNL nuclear data search, version 2.0, february 1999

Cox, J. P., & Giuli, R. T. 1968, Principles of Stellar Structure (Gordon and Breach)

Duchêne, G., & Kraus, A. 2013, Annual Review of Astronomy & Astrophysics, 51, 269

Eggenberger, P., Meynet, G., Maeder, A., et al. 2008, Astrophysics and Space Science, 316, 43

Eggleton, P. P. 1983, Astrophysical Journal, 268, 368

Ekström, S., Georgy, C., Eggenberger, P., et al. 2012, Astronomy & Astrophysics, 537, A146

Frankowski, A., & Tylenda, R. 2001, Astronomy & Astrophysics, 367, 513

Fricke, K. 1968, Zeitschrift fur Astrophysik, 68, 317

Friend, D. B., & Abbott, D. C. 1986, The Astrophysical Journal, 311, 701

Gayley, K. G. 1995, The Astrophysical Journal, 454, 410

Georgy, C., Meynet, G., & Maeder, A. 2011, Astronomy and Astrophysics, 527, A52

Glebbeek, E., Gaburov, E., de Mink, S. E., Pols, O. R., & Portegies Zwart, S. F. 2009, Astronomy and Astrophysics, 497, 255

Goldreich, P., & Schubert, G. 1967, The Astrophysical Journal, 150, 571

Grevesse, N., & Sauval, A. 1998, Space Science Reviews, 85, 161

Han, Z. 1998, Monthly Notices of the Royal Astronomical Society, 296, 1019

Han, Z., Eggleton, P. P., Podsiadlowski, P., & Tout, C. A. 1995, Monthly Notices of the Royal Astronomical Society, 277, 1443

Heger, A., Woosley, S. E., & Waters, R. 2000, in The First Stars, ed. A. Weiss, T. G. Abel, & V. Hill, 121

Hensler, G. 2008, in IAU Symposium, Vol. 252, The Art of Modeling Stars in the 21st Century, ed. L. Deng & K. L. Chan, 309–315

Henyey, L., Vardya, M., & Bodenheimer, P. 1965, The Astrophysical Journal, 142, 841

Herwig, F. 2000, Astronomy and Astrophysics, 360, 952

Higgins, E. R., & Vink, J. S. 2019, Astronomy & Astrophysics, 622, A50

Hunter, I., Brott, I., Lennon, D. J., et al. 2008, The Astrophysical Journal Letters, 676, L29

Hurley, J. R., Tout, C. A., & Pols, O. R. 2002, Monthly Notices of the Royal Astronomical Society, 329, 897

Hut, P. 1981, Astronomy & Astrophysics, 99, 126

Iglesias, C. A., & Rogers, F. J. 1996, The Astrophysical Journal, 464, 943

Keszthelyi, Z., Puls, J., & Wade, G. 2017, Astronomy & Astrophysics, 598, A4

Kudritzki, R. P., Pauldrach, A., Puls, J., & Abbott, D. C. 1989, Astronomy & Astrophysics, 219, 205

Lamers, H. J., Snow, T. P., & Lindholm, D. M. 1995, The Astrophysical Journal, 455, 269

Langer, N. 1998, Astronomy & Astrophysics, 329, 551

LeBlanc, F. 2010, An Introduction to Stellar Astrophysics (John Wiley & Sons)

Lebovitz, N. R. 1967, Annual Review of Astronomy and Astrophysics, 5, 465

Lecar, M., Wheeler, J. C., & McKee, C. F. 1976, Astrophysical Journal, 205, 556

Ledoux, P. 1947, The Astrophysical Journal, 105, 305

Lodders, K. 2003, The Astrophysical Journal, 591, 1220

Lucy, L. B., & Solomon, P. M. 1970, The Astrophysical Journal, 159, 879

Maeder, A., & Meynet, G. 2000, Astronomy & Astrophysics, 361, 159

Maeder, A., & Meynet, G. 2012, Reviews of Modern Physics, 84, 25

Maeder, A., & Stahler, S. 2009, Physics Today, 62, 52

Maeder, André & Zahn, J.-P. 1998, Astronomy and Astrophysics, 334, 1000

Markova, N., Puls, J., & Langer, N. 2018, Astronomy & Astrophysics, 613, A12

Meynet, G., & Maeder, A. 1997, Astron. Astrophys, 321, 465

Meynet, G., & Maeder, A. 2000, Astronomy and Astrophysics, 361, 101

—. 2002, Astronomy & Astrophysics, 390, 561

Mihalas, D., & Kunasz, P. B. 1978, The Astrophysical Journal, 219, 635

Milne, E. 1926, Monthly Notices of the Royal Astronomical Society, 86, 459

Mitalas, R., & Sills, K. R. 1992, The Astrophysical Journal, 401, 759

Morel, T., Butler, K., Aerts, C., Neiner, C., & Briquet, M. 2007, Communications in Asteroseismology, 150, 199

Newton, I. 1642-1727, Principia : the mathematical principles of natural philosophy, ed. D. Adee (N. W. Chittenden. New-York : Daniel Adee, 1846.), 581

Nugis, T., & Lamers, H. J. G. L. M. 2000, Astronomy & Astrophysics, 360, 227

Pauldrach, A., & Puls, J. 1990, Astronomy and Astrophysics, 237, 409

Paxton, B., Bildsten, L., Dotter, A., et al. 2010, The Astrophysical Journal Supplement Series, 192, 3

Paxton, B., Cantiello, M., Arras, P., et al. 2013, The Astrophysical Journal Supplement Series, 208, 4

Paxton, B., Marchant, P., Schwab, J., et al. 2015, The Astrophysical Journal Supplement Series, 220, 15

Paxton, B., Schwab, J., Bauer, E. B., et al. 2018, The Astrophysical Journal Supplement Series, 234, 34

Petrovic, J., Langer, N., Yoon, S.-C., & Heger, A. 2005, Astronomy & Astrophysics, 435, 247

Puls, J., Springmann, U., & Lennon, M. 2000, Astronomy and Astrophysics Supplement Series, 141, 23

Puls, J., Vink, J. S., & Najarro, F. 2008, The Astronomy and Astrophysics Review, 16, 209

Rappaport, S., Verbunt, F., & Joss, P. C. 1983, Astrophyiscal Journal, 275, 713

Reimers, D. 1975, Memoires of the Societe Royale des Sciences de Liege, 8, 369

Rogers, FJ & Nayfonov, A. 2002, The Astrophysical Journal, 576, 1064

Saumon, D., Chabrier, G., & Van Horn, H. 1995, The Astrophysical Journal Supplement Series, 99, 713

Schwarzschild, K. 1906, Nachrichten von der Königlichen Gesellschaft der Wissenschaften zu Göttingen. Math.-phys. Klasse, 195, p. 41-53, 195, 41

Soberman, G., Phinney, E., & Van den Heuvel, E. 1997, Astronomy and Astrophysics, 327, 620

Sobolev, V. V. 1960, Moving envelopes of stars

Song, H., Jiangtao Wang, f. S., Ruiyu Zhang, Z. L., Weigue Peng, Q. Z., & Jing, J. 2018, The Astrophysical Journal, 859, 13

Spiegel, E. A., & Zahn, J.-P. 1992, Astronomy & Astrophysics, 265, 106

Spruit, H. 2002, Astronomy & Astrophysics, 381, 923

Spruit, H. C. 1999, Astronomy & Astrophysics, 349, 189

Strickland, D. K., & Stevens, I. R. 1998, Monthly Notices of the Royal Astronomical Society, 297, 747

Taylor, R. J. 1973, Monthly Notices of the Royal Astronomical Society, 161, 365

Timmes, F. X. 1999, The Astrophysical Journal Supplement Series, 124, 241

Timmes, F. X., & Swesty, F. D. 2000, The Astrophysical Journal Supplement Series, 126, 501

Tout, C. A., & Eggleton, P. P. 1988, Monthly Notices of the Royal Astronomical Society, 231, 823

Vink, J. S. 2015, in Very massive stars in the local universe (Springer), 77–111

Vink, J. S., de Koter, A., & Lamers, H. 2001, Astronomy & Astrophysics, 369, 574

Vink, J. S., de Koter, A., & Lamers, H. J. 1999, Astronomy & Astrophysics, 350, 181

Von Zeipel, H. 1924, Monthly Notices of the Royal Astronomical Society, 84, 665

Weaver, R., McCray, R., Castor, J., Shapiro, P., & Moore, R. 1977, Astrophysical Journal, 218, 377

Weaver, T. A., Zimmerman, G. B., & Woosley, S. 1978, The Astrophysical Journal, 225, 1021

Yoon, S.-C., & Langer, N. 2005, Astronomy & Astrophysics, 443, 643

Yoon, S. C., Langer, N., & Norman, C. 2006, Astronomy & Astrophysics, 460, 199

Zahn, J.-P. 1975, Astronomy & Astrophysics, 41, 329

—. 1977, Astronomy & Astrophysics, 57, 383

Zahn, J.-P. 1992, Astronomy and Astrophysics, 265, 115

Appendix A
Inlists provided by Erin Higgins & Dr. Jorick Vink

In the following "true" means the option is turned on therefore "false" is off. If there is an "!" this means the line is commented out and the FORTRAN library is not initialized.

```
&star_job  show_log_description_at_start = .true.
eos_file_prefix = 'mesa'
kappa_file_prefix = 'gs98'
set_initial_age = .true. ! begin without pre-MS
initial_age = 0 ! starting model age in years
create_pre_main_sequence_model = .false. ! begin with a pre-main sequence model
pgstar_flag = .true. ! display on-screen plots
pause_before_terminate = .true. ! allow plots to remain on screen
!————————————ROTATION————————————!
new_rotation_flag = .true.
change_rotation_flag = .true.
change_initial_rotation_flag = .true.
new_surface_rotation_v = 200 ! in km/s
set_surface_rotation_v = .true.
set_initial_surface_rotation_v = .true.
change_v_flag = .true.
change_initial_v_flag = .true.
new_v_flag = .true.
/ ! end of star_job namelist
&controls
!————————————- STOPPING CONDITIONS ————————————————!
! run_star_extras stopping condition for log[N/H]+12 <= [some value]
! currently turned off
xa_central_lower_limit_species(1) = 'h1'
xa_central_lower_limit(1) = 0.01
! max_age = 4.5d6
! star_mass_min_limit = 30
! log_L_upper_limit = 1d99
!————————————-OUTPUT PARAMETERS ————————————————!
do_history_file = .true.
history_interval = 10
star_history_name = 'test/rot/27Mv200.data'
profile_interval = 25
terminal_interval = 5
write_header_frequency = 10
num_trace_history_values = 1
trace_history_value_name(1) = 'log_abs_mdot'
```

trace_history_value_name(2) = 'log[N/H]+12'
!————————BASIC PARAMETERS————————!
initial_mass = 27 ! Mass in Msun units
mesh_delta_coeff = 1.5 ! Larger values increase the max deltas,decreases the no. of grid points
mesh_delta_coeff_for_highT = 2.5 ! ĥor high T
varcontrol_target = 1d-4 ! Target value for relative variation in the structure between models
use_Type2_opacities = .true. ! Default opacities for Massive stars
Zbase = 0.02 ! Base Metallicity: Galacticz=0.014, SMCz=0.004, LMC/Bonn=0.0088
!————————MIXING PARAMETERS————————!
mixing_length_alpha = 1.5 ! Geneva use 1.6 <40 Msol, and 1.0 >40 Msol. Bonn/MESA default use 1.5
MLT_option = 'Henyey' ! Options: Cox, ML1, Ml2, Mihalas, Henyey, none Orginially Henyey
okay_to_reduce_gradT_excess = .false. ! MLT++ on=true/off=false
gradT_excess_lambda1 = -1.0 ! Full MLT++ on
use_Ledoux_criterion = .true. ! Schwarzschild criterion if false
alpha_semiconvection = 1 ! Determines efficiency of semiconvective mixing
!————————OVERSHOOTING PARAMETERS————————!
overshoot_f0_above_nonburn_core = 0.005 ! overshoot distance in the expense of the core: pre-MS
overshoot_f0_above_nonburn_shell = 0.005
overshoot_f0_below_nonburn_shell = 0.005
overshoot_f0_above_burn_h_core = 0.005 ! overshoot distance in the expense of the core: MS
overshoot_f0_above_burn_h_shell = 0.005
overshoot_f0_below_burn_h_shell = 0.005
overshoot_f0_above_burn_he_core = 0.005 ! overshoot distance in the expense of the core: post-MS
overshoot_f0_above_burn_he_shell = 0.005
overshoot_f0_below_burn_he_shell = 0.005
overshoot_f0_above_burn_z_core = 0.005 ! overshoot distance in the expense of the core: post-MS
overshoot_f0_above_burn_z_shell = 0.005
overshoot_f0_below_burn_z_shell = 0.005
step_overshoot_D0_coeff = 1 ! Diffusion coefficient D at point r0
step_overshoot_f_above_burn_h_core = 0.1 ! Step overshooting values:
step_overshoot_f_above_burn_h_shell = 0.1 ! alpha_ov= 0.335 -> Bonn Model
step_overshoot_f_below_burn_h_shell = 0.1 ! alpha_ov= 0.1 -> Geneva Model
step_overshoot_f_above_burn_he_core = 0
step_overshoot_f_above_burn_he_shell = 0

step_overshoot_f_below_burn_he_shell = 0
step_overshoot_f_above_burn_z_core = 0
step_overshoot_f_above_burn_z_shell = 0
step_overshoot_f_below_burn_z_shell = 0
!————————MASS LOSS————————!
hot_wind_scheme = 'Vink' !Vink et al 2001 treatment of mass loss
hot_wind_full_on_T = 1.2d4 !T limits
cool_wind_full_on_T = 1.0d4 !T limits —- hot_wind_full_off_T command doesn't exist
Vink_scaling_factor = 1.0d0 !"Mass-loss predictions for O and B stars as a function of metallicity" mdot_omega_power = 0.0d0
!————————ROTATION————————!
! Chemical Mixing ! 1 -> on, 0 -> off D_DSI_factor = 1 ! dynamical shear instability D_SH_factor = 0 ! Solberg-Hoiland D_SSI_factor = 1 ! secular shear instability D_ES_factor = 1 ! Eddington-Sweet circulation D_GSF_factor = 1 ! Goldreich-Schubert-Fricke D_ST_factor = 0 ! Spruit-Tayler dynamo
! this is for ang.mom. transport
am_nu_DSI_factor = 1
am_nu_SH_factor = 0
am_nu_SSI_factor = 1
am_nu_ES_factor = 1
am_nu_GSF_factor = 1
am_nu_ST_factor = 0
am_gradmu_factor = 0.1d0 ! f_mu from Brott et al
am_nu_factor = 1d0 ! this factor accounts for angular momentum transfer
am_D_mix_factor = 0.0333333333333333d00
/ ! End of controls namelist

Appendix B

Inlists provided by Zsolts Keszthelyi for Brott Model

! inlist to compare rotating MESA models with Bonn group models. Published by Keszthelyi, Puls, Wade (2017) A&A 598 A4. (Figure 3.) ! Note that the comparison holds for rotational velocities up to 300 km/s. Closer to the critical rotation (500 km/s) differences arise when using this simple inlist.

```
& star_job
! display on-screen plots pgstar_flag = .true.
pause_before_terminate = .false.
!========= New METALLICITY ========================!
relax_initial_Z = .true. ! gradually changes abundance from Z = 0.02
new_Z = 0.014d0
relax_initial_Y = .true.
new_Y = 0.2638d0
set_uniform_initial_composition = .true. ! if false the rest are not set.
initial_h1 = 0.7274d0 initial_he4 = 0.2638d0
initial_h2 = 0d0 initial_he3 = 3.27733d-5
initial_zfracs = 5 ! 5 Asplund et al 2005. ! 0 when you define them in controls
!========= surface ROTATION ==================!
new_rotation_flag = .true.
change_rotation_flag = .true.
change_initial_rotation_flag = .true.
new_surface_rotation_v = 315 ! in km/s
set_surface_rotation_v = .true.
set_initial_surface_rotation_v = .true.
/ !end of star_job namelist
&controls
do_history_file = .true.
max_model_number = 150000
history_interval = 30
profile_interval = 50
terminal_interval = 5
write_header_frequency = 10
!========= The OUTPUT ========== - filename -
star_history_name = 'Bonn_rot/M20_v274_Bonn.data'
log_directory = 'LOGS'
photo_directory = 'photos'
! INITIAL specifications
!——— initial MASS———————
initial_mass = 20
!————————————————
! initial mass fraction of elements, only when initial_zfracs = 0
!z_fraction_c = 0.1139
```

```
!z_fraction_n = 0.1070
!z_fraction_o = 0.1198
!z_fraction_f = 0.0639
!z_fraction_ne = 0.1098
!z_fraction_na = 0.0864
!z_fraction_mg = 0.1025
!z_fraction_al = 0.0892
!z_fraction_si = 0.1038
!z_fraction_fe = 0.1037
!———————————————————————
! STOPPING options
! max_age = 3d6
Teff_lower_limit = 13d3
! stop when the center mass fraction of h1 drops below this limit
! xa_central_lower_limit_species(1) = 'h1'
! xa_central_lower_limit(1) = 1d-1
!======= MASS-LOSS RATES ==============================
! enhance mass loss due to rot. see control defaults for Eq.
mdot_omega_power = 0.43
! use_other_wind = .true.
hot_wind_scheme = 'Vink'
Vink_scaling_factor = 1.0d0
cool_wind_RGB_scheme = 'Dutch'
cool_wind_AGB_scheme = 'Dutch' !  wind schemes and naming have been changed in new versions!
Dutch_scaling_factor = 1.0d0
!======== ROTATIONAL INSTABILITIES =========!
skip_rotation_in_convection_zones = .true.
!==================================
am_nu_factor = 1d0 ! this factor accounts for angular momentum transfer
!==================================
am_D_mix_factor = 0.0228d0 ! commenting out sets it to zero
!==================================
! factor for rot.instabilities => D_mix = diffusion coefficient => this is multiplied by f_c
!  D_mix = D_mix_nonrot + am_D_mix_factor * ( D_SI + ...)  this is f_c from Heger et al
! 1 is normal, 0 turns off
! this is for chemical mixing
D_DSI_factor = 1 ! dynamical shear instability
D_SH_factor = 0 ! Solberg-Hoiland
D_SSI_factor = 1 ! secular shear instability
```

```
    D_ES_factor = 1 ! Eddington-Sweet circulation
    D_GSF_factor = 1 ! Goldreich-Schubert-Fricke
    D_ST_factor = 0 ! Spruit-Tayler dynamo
    ! this is for ang.mom. transport
    am_nu_DSI_factor = 1
    am_nu_SH_factor = 0
    am_nu_SSI_factor = 1
    am_nu_ES_factor = 1
    am_nu_GSF_factor = 1
    am_nu_ST_factor = 1
    !------------------------------
    am_gradmu_factor = 0.1d0 ! This is f_mu from Brott et al
    !------------------------------
    ! mix_factor = 0 ! for every single diffusion coeff. including D_conv !
    !============== MIXING LENGTH parameters ================!
    mixing_length_alpha = 1.5d0
    ! allow_semiconvective_mixing = .true. command no longer exists
    use_Ledoux_criterion = .true. ! Need this to have mixing in semiconvection
    alpha_semiconvection = 1d0
    MLT_option = 'ML1' !  Cox, ML1 - Bohm-Vitense, Ml2 - Bohm-Cas, Mihalas,
Henyey, none
    ! ============== OVERSHOOTING ==================== !
    ! This procedure gives back the 0.335 H_P extension used by Brott et al.
    !---- exponential decay ---------- !
    ! overshoot_f_above_burn_h = 0.001d0 command no longer exists
    overshoot_f_above_burn_h_core = 0.001d0
    overshoot_f_above_burn_h_shell = 0.001d0
    overshoot_f0_above_burn_h_shell = 0.001d0
    !------ overshoot distance in the expense of the core ----------!
    ! overshoot_f0_above_burn_h = 0.03d0
    overshoot_f0_above_burn_h_core = 0.03d0
    !------ step function - extension above the core ----------!
    ! step_overshoot_f_above_burn_h = 0.365d0 command no longer exists
    step_overshoot_f_above_burn_h_core = 0.365d0
    step_overshoot_D0_coeff = 1d0
    !-----------------------------------------------
    / ! end of controls namelist
```

Appendix C
Binary Star Inlist

```
&binary_job
    inlist_names(1) = 'inlist1'
    inlist_names(2) = 'inlist2'
    evolve_bot_stars = .true.
    / ! end of binary_job namelist
    &binary_controls
    !———————- INITIAL PARAMETERS ———!
    m1 = 35.0d0 ! Primary mass in Msun
    m2 = 25.0d0 ! Secondary mass in Msun
    initial_period_in_days = 4.0d0
    limit_retention_by_mdot_edd = .false.
    max_tries_to_achieve = 20
    mdot_scheme = "Ritter" ! Options are Ritter, Kolb, roche_lobe, and contact
    !———————- WIND PARAMETERS ————!
    do_enhance_wind_1 = .true. ! tidally enhance the wind mass loss from one or
both components From Tout & Eggleton (1988) do_enhance_wind_2 = .true.
    tout_B_wind_1 = 1d4
    tout_B_wind_2 = 1d4
    do_wind_mass_transfer_1 = .true. ! transfer part of the mass lost due to stellar
winds From Bondi & Hoyle (1944) do_wind_mass_transfer_2 = .true.
    !———————- OUTPUT ——————————!
    history_name = ' ' ! Name of file for binary output
    log_directory = ' ' ! Directory for binary output
    history_interval = 20
    terminal_interval = 5
    write_header_frequency = 10
    !———————- STOPPING CONDITIONS ——————————-!
    ! accretor_overflow_terminate = 1.0d0
    terminate_if_initial_overflow = .true. ! terminate evolution if first model of run
is overflowing
    terminate_if_L2_overflow = .true. ! terminate evolution if there is overflow
through the L2 point
    !———————- MASS TRANSFER EFFICIENCY CONTROLS———!
    ! mass_transfer_alpha = 0.0d0 ! fraction of mass lost from the vicinity of the
donor as fast wind
    ! mass_transfer_beta = 0.0d0 ! fraction of mass lost from the vicinity of the
accretor as fast wind
    ! mass_transfer_delta = 0.0d0 ! fraction of mass lost from circumbinary coplanar
toroid
    ! mass_transfer_gamma = 0.0d0 ! radius of the circumbinary coplanar toroid is
‘gamma**2 * orbital_separation‘
```

```
!————————- ORBITAL ANGULAR MOMENTUM PARAMETERS ——!
do_jdot_ls = .true. ! Angular momentum loss due to mass transfer inefficiency
do_jot_missing_wind = .true. ! Angular momentum loss due to winds (Requires rotation)
do_jdot_ml = .true. ! Angular momentum loss due to mass leaving the system
do_jdot_mb = .false. ! Angular momentum loss due to magnetic breaking (This and Tides can't be both be set to true)
do_jdot_gr = .false. ! Gravitational wave radiation
include_accretor_mb = .false.
keep_mb_on = .false.
! magnetic_braking_gamma = 3.0d0
! jdot_multiplier = 1d0
!————————- ROTATION AND SYNC PARAMETERS ————-!
do_j_accretion = .false.
do_tidal_sync = .true. ! Applies tidal torque to the star
sync_type_1 = "Hut_rad" ! options are Instantaneous, Orb_period, Hut_conv, Hut_rad, and None
sync_type_2 = "Hut_rad"
sync_mode_1 = "Uniform" ! Where angular momentum is deposited for synchronization.
sync_mode_2 = "Uniform"
! Ftid_1 = 1d0 ! Tidal strength factor.
! Ftid_2 = 1d0
! do_initial_orbit_sync_1 = .true. ! Relax rotation of star to orbital period at the beggining of evolution.
! do_initial_orbit_sync_2 = .true.
/ ! end of binary_controls namelist
```

Appendix D
Example Fortran Algorithms Programmed in MESA

D.1 Vink prescription algorithum

This can be found in mesa/star/private/wind.f90. W is the pointer for wind. pow_cr is defined in MESA's crlimb directory. This directory contains the functions such $\tan x$, $\cos x$ and pow(x,n) $= x^n$ example. pow(x,3) $= x^3$ where x can be any function or pointer. This is programmed for more precision by defining $x^3 = x * x * x$ for example. dp is defined as double float precision.

```
subroutine eval_Vink_wind(w)
real(dp), intent(inout) :: w
real(dp) :: alfa, w1, w2, Teff_jump, logMdot, dT, vinf_div_vesc
! alfa = 1 for hot side, = 0 for cool side
if (T1 > 27500d0) then
alfa = 1
else if (T1 < 22500d0) then
alfa = 0
else ! use Vink et al 2001, eqns 14 and 15 to set "jump" temperature
Teff_jump = 1d3*(61.2d0 + 2.59d0*(-13.636d0 + 0.889d0*log10_cr(Z/Zsolar)))
dT = 100d0
if (T1 > Teff_jump + dT) then
alfa = 1
else if (T1 < Teff_jump - dT) then
alfa = 0
else
alfa = (T1 - (Teff_jump - dT)) / (2*dT)
end if
end if
if (alfa > 0) then ! eval hot side wind (eqn 24)
vinf_div_vesc = 2.6d0 ! this is the hot side galactic value
vinf_div_vesc = vinf_div_vesc*pow_cr(Z/Zsolar,0.13d0) ! corrected for Z
logMdot = &
- 6.697d0 &
+ 2.194d0*log10_cr(L1/Lsun/1d5) &
- 1.313d0*log10_cr(M1/Msun/30) &
- 1.226d0*log10_cr(vinf_div_vesc/2d0) & + 0.933d0*log10_cr(T1/4d4) &
- 10.92d0*pow2(log10_cr(T1/4d4)) &
+ 0.85d0*log10_cr(Z/Zsolar)
w1 = exp10_cr(logMdot)
```

```
else
w1 = 0
end if
if (alfa < 1) then ! eval cool side wind (eqn 25)
vinf_div_vesc = 1.3d0 ! this is the cool side galactic value
vinf_div_vesc = vinf_div_vesc*pow_cr(Z/Zsolar,0.13d0) ! corrected for Z
logMdot = &
- 6.688d0 &
+ 2.210d0*log10_cr(L1/Lsun/1d5) &
- 1.339d0*log10_cr(M1/Msun/30) &
- 1.601d0*log10_cr(vinf_div_vesc/2d0) &
+ 1.07d0*log10_cr(T1/2d4) &
+ 0.85d0*log10_cr(Z/Zsolar)
w2 = exp10_cr(logMdot)
else
w2 = 0
end if
w = alfa*w1 + (1 - alfa)*w2
if (dbg) write(*,*) 'vink wind', w
end subroutine eval_Vink_wind
```

D.2 Eggleton & Tout Wind Enhancement Factor

This is found in /mesa/binary/private/wind.f90

```
subroutine Tout_enhance_wind(b, s)
type (binary_info), pointer :: b
type (star_info), pointer :: s
! Tidaly enhance wind mass loss as described by
! Tout & Eggleton 1988,MNRAS,231,823 (eq. 2)
real(dp) :: B_wind ! enhancement parameter, B in eq. 2
integer :: i, s_i
real(dp) :: dm
real(dp), DIMENSION(b % anomaly_steps):: rl_d, r_rl, mdot
if (s% id == b% s1% id) then
if (.not. b% do_enhance_wind_1) return
B_wind = b% tout_B_wind_1
s_i = 1
else
if (.not. b% do_enhance_wind_2) return
B_wind = b% tout_B_wind_2
s_i = 2
```

```
    end if
    ! phase dependent roche lobe radius
    rl_d = (1-b%eccentricity**2) / (1+b%eccentricity*cos(b% theta_co)) * b% rl(s_i)
    do i = 1,b% anomaly_steps !limit radius / roche lobe
    r_rl(i) = min(pow6(b% r(s_i) / rl_d(i)), pow6(0.5d0))
    end do
    ! actual enhancement
    mdot = s% mstar_dot * (1 + B_wind * r_rl)
    dm = 0d0
    do i = 2,b% anomaly_steps ! trapezoidal integration
    dm = dm + 0.5d0 * (mdot(i-1) + mdot(i)) * (b% time_co(i) - b% time_co(i-1))
    end do
    ! remember mass-loss is negative!
    !b% mdot_wind_theta = b% mdot_wind_theta + mdot !  store theta dependance for edot
    s% mstar_dot = dm ! return enhanced wind mass loss
    end subroutine Tout_enhance_wind
```

Appendix E
Variable Symbols and Descriptions

Below is a description for the variables shown in the thesis. The tables do not include every variable mention in the paper. The purpose of the tables were to prevent confusion between variables that had nearly the same symbol e.g., k_r and k_f.

Table of Symbols

Symbol	Description
M	Mass of a star
M_{sys}	Binary system mass
M_1	Primary star mass
M_2	Secondary star mass
L	Luminosity of the star
T	Local temperature
T_{eff}	Surface temperature
T_{Jump}	Bi-stability jump temperature
P	Pressure
G	Gravitational constant
ρ	Density
k_r	Thermal conductivity
ϵ	Nuclear energy generation rate
σ_{ST}	Stefan-Boltzmann constant
ϕ	Equation variable
σ	Equation of state variable
v_{rot}	Surface rotation velocity
v_{init}	Initial rotation velocity
Q	Thermal energy
V	Volume
κ_λ	Opacity for a photon of specific wavelength
l	Mean free path
$\dot{M}_W$	Wind mass loss rate
$\dot{M}_{RLOF}$	Mass transfer due to RLOF
$\dot{M}_\star$	Total mass loss rate from a star
α_{conv}	Convection coefficient
α_{sc}	Semiconvection coefficient
α_{conv}	Step overshoot coefficient

Table of Symbols continued

Symbol	Description
f_{ov}	Exponential overshoot coefficient
∇_{rad}	Radiative gradient
∇_{ad}	Adiabatic gradient
μ	Mean molecular weight
∇_{μ}	Mean molecular weight gradient
H_P	Pressure scale height
H_P	Velocity scale height
f_v	Wind factor for Vink scheme
β	Mass Luminosity Parameter that varies as a function of mass
δt	Time step
k	Specific cell layer within MESA
$\vec{g}_{grav}$	Gravitational acceleration
$\vec{g}_{eff}$	Local gravity
$\vec{g}_{cent}$	Centripetal acceleration
$\vec{g}_{rad}$	Radiative acceleration
V_c	Solid body rotation potential
ϕ	Gravitational potential
Ψ	Sum of rotation and gravitation potentials
$\lvert\vec{\nabla}\Omega\rvert$ or $\frac{d\Omega}{dr}$	Rotational shear
Ω	Rotation rate
$\Omega(k)$	Rotation of cell k
Ω_{crit}	Critical Rotation Rate
$\dot{\Omega}_{k,j}$	Change in rotation rate for either star at cell layer k
v_{crit}	Critical rotation velocity
$\bar{\Omega}$	Average rotation rate over an isobaric surface
$\hat{\Omega}$	Zonal rotation rate over an isobaric surface
ω_{orb}	Orbital rotation rate
t_{dyn}	Dynamical timescale
t_{kh}	Thermal timescale
t_{sys}	System age
L_W	Mechanical Luminosity
$v_2(t)$	Expansion rate of a bubble
L_b	Luminosity of region (b)
T_b	Temperature of region (b)
n_0	ISM atomic density
n_b	Atomic density of region (b)

Table of Symbols continued

Symbol	Description
L_{Edd}	Eddington luminosity
v_{in}	velocity before momentum transfer
v_{out}	velocity after momentum transfer
g_{rad}^{line}	Line radiation acceleration
σ_e	Thomson Cross section for an electron
g_{rad}^{TH}	Thomson accleration
v_s	Sound speed in a gas
f_i	Resonance frequency of a transition
ν_i	Resonance frequency of a line
v_{th}	Thermal velocity
L_ν	Luminosity for photon of a specific frequency
v_∞	Wind velocity out to infinity
$v(r)$	Wind velocity as a function of radius
α_T	Ratio of line acceleration of optically thick lines to the sum of all lines
δ_i	Describes the ionization in the wind
$\alpha^{'}$	Coefficient that is based upon α_T and δ
k_f	Measure of the number of lines stronger than Thomson scattering
$M(t)$	Ratio of the line acceleration to the Thomson acceleration
m	Depends on α_T and δ
v_{esc}	Escape velocity at the surface of the star
B_W	Tidally enhanced wind coefficient
R_L	Rochle lobe radius
α_W	Wind mass transfer parameter
β_W	Wind mass transfer parameter based on spectral type
v_{orb}	Orbital velocity
σ_g	Characteristic growth rate for the SP-dynamo
ω_A	Alfén Frequency
v_A	Alfén velocity
B_A	Magnetic field on the Alvén surface
ρ_W	Wind Density
χ_n	Mass fraction of species n
f_c	Angular momentum diffusion factor
f_ν	Angular momentum transfer factor
f_μ	The ∇_μ factor
Γ_{factor}	Eddington Factor
P_{orb}	Orbital period
J_{orb}	Orbital angular momentum
k_a	Apsidal motion constant
$\dot{J}_{ml}$	Change in orbital angular momentum due to mass loss
$\dot{J}_{ls}$	Change in orbital angular momentum due to spin-orbit coupling
$\dot{J}_{mb}$	Change in orbital angular momentum due to magnetic breaking